Properties Modification of Nanopatterned Surfaces Functionalized with Photo-activated Ligands

Stefan Stoianov

Dissertation submitted to the faculty of the Virginia Polytechnic Institute and State University

In partial fulfillment of the requirements for the degree of

Doctor of Philosophy

in

Physics

Hans Robinson, Chairman

Yong Xu

James R. Heflin

Mark Pitt

December 7th, 2011

Blacksburg, VA 24060

Keywords: ionic self assembled multilayer film, convective self-assembly, surface enhanced Raman spectroscopy, surface functionalization

Properties Modification of Nanopatterened Surfaces Functionalized with Photo-activated Ligands

Stefan Stoianov

Abstract

This dissertation focuses on four research topics: self-assembly of colloidal nanoparticles, surface modifications of the properties of ionically self-assembled multilayer films, surface enhanced Raman spectroscopy of functionalized gold nanoparticles, and two photon uncaging in gel. Those techniques are used for development of novel nanofabrication methods for top-down and bottom-up assembly of nanostructures, by modifying the properties of nanopatterned surfaces with photoactive ligands, and other technologies.

First I describe the development of an improved method for nanosphere lithography, a variation of the convective self-assembly technique. The method exhibited high reproducibility and yielded high quality monolayer crystals by withdrawing a meniscus of liquid polystyrene spheres solution and subsequent evaporation of the solvent. The monolayer crystal was used as an evaporation mask to create surface arrays of gold nanotriangular particles.

Metal nanoparticles, with sharp features or narrow gaps, exhibit strong plasmonic properties. I took advantage of those properties to attempt to create patchy modifications of the surface functionalization of gold nanotriangular particles treated with photosensitive molecules. Two molecules denoted, P3-DTC, and LIP3, were used as functional molecules attached to the gold nanoparticles.

After interaction with 356nm UV light, part of those molecules cleaves off the surface of the nanoparticles rendering the surface modified with a new functional group. The modification takes place only at the plasmonic hot spots of those nanoparticles, resulting in a patchy modification of the properties of the nanoparticles.

I built polymer Ionically Self-assembled Multilayer (ISAM) films using a Layer-by-Layer deposition technique and treated them to alter their surface adhesion properties. Poly (allylamine hydrochloride) (PAH), and poly (styrene sulfonate) (PSS) are a very well-studied system of polyelectrolytes for LbL deposition. ISAM films built from those polyelectrolytes are rich in amine groups to which nanoparticles, cells, tissue cultures, ligands can be made to adhere. In my work I developed a method for selective modification of the surface adhesiveness, by neutralizing the amine groups trough acetylation with acetic anhydride. With resolution from a few microns to a few hundred nanometers, I selectively passivated some areas of the ISAM film while others I left unaltered. I tested the effect of the acetic anhydride passivation by performing Horse Radish Peroxidase (HRP) test which quantifies the amount of free amines on the surface of the film. I also demonstrated the patchy modification of surface adhesiveness by introducing gold nanospheres which attached only to the amine active areas of the modified ISAM film.

Photoactivatable fluorophores, *i.e.* compounds and other entities that may transform into a fluorescent form on absorption of a photon can be employed in multidimetional volume patterning. I studied the photoactivation of aryl azides in gelatin matrix. Specifically, I used Azidocoumarin 151 as a test molecule to undergo two-photon activation, and then measured the resulting photoluminescence. The activation of the Azidocoumarin 151 can be used to create arbitrary 3D patterns of modified functionality inside the gel. The activated molecules can be

used as sites for further modification of the patterning inside the volume of the gel. Possible modifications include attaching biomolecules, nanoparticles, or individual cells.

Acknowledgements

I would like to acknowledge my adviser Hans Robinson for giving me the opportunity to work on several very interesting projects. Dr. Robinson has taught me critical thinking and supported greatly my research in his laboratory. He was always kind and willing to discuss scientific ideas and therefore contributed to my development as a successful graduate student.

I'd like to also thank Dr. Richie Davis and Dr. Webster Santons for the useful discussions about my projects. I had the great pleasure to work closely with several graduate students during my time at Virginia Tech. Kai Chen, helped me get into the field of polymer self-assembled films. I worked closely with Jason Ridley on modifying surface properties of ISAM films. Brandon Thorpe has been a constant supplier of a variety of compounds that I used in my SERS studies. I'd like to thank my fellow graduate students from Dr. Robinson's group, Chih-Yu Jao, Erich See, Kirby Mayers, for being great company and lending help when I need it.

During my stay at Virginia Tech I have met some wonderful faculty and staff at the Department of Physics. They were all very helpful, but I'd like to extend special thanks to Chris Thomas, Dr. Ghiti Khodaparast, Dr. Mark Pitt, Dr. Tetsuro Mizutani, and Randy Heflin.

Finally, I'd like to thank my wife Elitsa for being patient during my time as a graduate student. I'd like to also thank my daughter Eleonora and son Alexander for being the cutest kids in the world and for cheering me up all the time.

TABLE OF CONTENTS

LIST OF FIGURES

CHAPTER 1

CHAPTER 2

CHAPTER 3

CHAPTER 4

CHAPTER 5

CHAPTER 1 Introduction

Fabrication technologies in the field of nanoscience are promising to open new areas of research with many possibilities in applied science. Realization of their full potential will require merging top-down and bottom-up fabrication approaches. For instance, accurate spatial positioning of bottom-up fabricated nanoparticles and nanoassemblies provided by top-down lithographic methods can be applied in all but the simplest devices and systems, such as biosensors or molecule-like nanoparticle assemblies. A similar interest in controlling the positioning of living cells exists for applications such as tissue engineering, biosensors and cellular studies. Both cells and nanostructures are generally quite fragile and typically cannot withstand the processing conditions of most forms of lithography. This limitation can be overcome by patterning the adhesive properties of a substrate, so that adsorption of nano- or bio-structures at desired locations can be the very last step in the fabrication process. Therefore, the overall goal of this dissertation was to develop and apply methods for modifying the properties of nanopatterned surfaces.

This dissertation focuses on the development of both top-down and bottom-up techniques to pattern the surface properties of polymer films and metal nanoparticles. I have developed a method for substrate functionalization using Multilayer (ISAM) films and the modification of their surface adhesion properties. The modifications are made by chemical treatment and can be used for selective surface fixation of nanoparticles and nanostructures, cell cultures and tissue samples. Furthermore, I began development of a top-down method, based on the plasmonic properties of metal nanoparticles and resulting in patchy modification of the surface functionalization of the nanoparticles. The surface modification was achieved by photoactivation

of photosensitive molecules adsorbed on gold nanoparticles. For this purpose, I used triangular nanoparticles which exhibit strong plasmonic properties. The energy of the incident light is focused and enhanced at the sharp corners of the particles, the photosensitive molecules get activated and thus the surface functionalization at the hot spots is altered. The modified areas on the nanoparticle surface can be then used as adhesion sites for ligands, or other nanoparticles.

I developed of a nanosphere lithography method for colloidal crystal growth on a surface. In particular, I applied a modified version of the convective self-assembly method[1], known as restricted meniscus convective self-assembly and a theoretical model to explain the experimental results was developed. In my research I used nanosphere lithography to deposit triangular nanoparticles on a substrate, and used them for applications in Chapter 3 and Chapter 4.

To study the plasmonic properties of gold nanoparticles for patchy modification of their surface properties, I fabricated ordered arrays of triangular gold nanoparticles on an ISAM film coated substrate. As described in Chapter 3, the ISAM film is rich in amines, has strong adhesive properties, and holds the gold nanoparticles in place even under such extreme conditions as sonication and strong solvent exposure. The nanoparticles were functionalized with photoactivatable molecules, which undergo transformation with absorption of one UV or two red photons. Upon photoactivation part of each molecule was cleaved away leaving exposed a suitably selected functional group, thus modifying the surface chemistry of the nanoparticles. Since the process of photoactivation employs the plasmonic properties of the nanoparticles, the photomolecules get activated predominantly at the hot spots, thus creating patchiness of the surface functionalization. To quantify the photactivation process, I measured the surface enhanced Raman spectrum of functionalized gold triangular nanoparticles before and after photoactivation. I was not able to obtain unequivocal result showing that the photomolecules I

used did undergo photactivation. There could be several reasons for that result; the photomolecules did not functionalize the gold triangular nanoparticles, or premature photo activation of the photoactive molecules due to lightning rod effect or chemical catalysis.

ISAM films can be used not only for surface anchoring of metal nanoparticles, but also for adhesion of other entities. I describe a layer-by-layer technique, using PAH and PSS, to deposit an ISAM film on a glass substrate. The ISAM film is rich in amine groups that are positively charged and can be used as anchors for attachment of other molecules or functionalized nanoparticles. The adhesiveness of the ISAM film was patterned by selectively neutralizing amines in some areas of the film while leaving other areas intact. Selective patterning was then demonstrated in two ways, by attaching Au nanospheres to the amine active areas of the film, and by using horse radish peroxidase as an amine detection test.

Finally, I investigated molecular photoactivation in gel. Using a femtosecond laser, molecules in small volume of the gel were activated. This process resulted in optical patterning of the activation sites because the properties of the photoactive molecules were altered after light absorption. The result of the photoactivation was fluorescence patterened in the volume of the gel, and also chemical modification of the photoactive molecules. Such chemical modification can be used to pattern the volume of the gel and then functionalize these sites with small nanoparticles, for example. Specifically, I have studied the two photon fluorescence on azidocoumarin 151 in gelatin gel, illuminated with femtosecond laser light. Two-photon absorption converted the azidocoumarin into a fluorescent dye, which easily bound to the gelatin matrix creating arbitrary three dimensional patterns. This process could be used for 3D patterning of the volume of the gel, and even for further functionalization of the activation sites with other molecules or simple attachment of nanoparticles.

I will now give an outline of each chapter followed by literature review of each topic in my dissertation.

1.1 Thesis Outline

CHAPTER 1. Introduction

Chapter 1 gives an overview of the four research topics in this dissertation: self-assembly of colloidal nanoparticles, surface modifications of the properties of ionically self-assembled multilayer films, surface enhanced Raman spectroscopy of functionalized gold nanoparticles, and two photon uncaging in gel, as well as a literature review on each topic.

CHAPTER 2. Restricted Meniscus Convective Self-Assembly

In this chapter, I present a variation of the convective self-assembly technique, where the meniscus of a polystyrene nanosphere suspension is restricted by a straight edge located approximately 100μm above the substrate adjacent to the drying zone as shown in Fig 1.1. The movement of the top plate leaves a wet thin film behind. Evaporation drives particles from the suspension to the edge of the wet thin film, enabling continuous growth of a thin ordered colloidal crystal. This technique yields high quality crystals of roughly twice the growth rate compared to conventional convective self-assembly. I attribute that to different rates of diffusion of vapor from the drying crystals in each case. I also investigated the growth rate dependence on the relative humidity, and found that the crystal growth rate was strongly dependent on the humidity. A theoretical model explaining well my experimental results is offered.

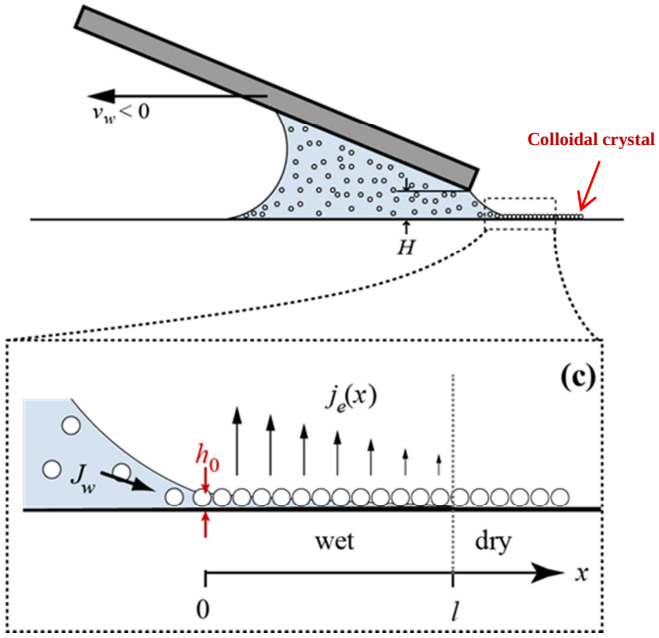

Fig1.1 Schematic of restricted meniscus self-assembly.

CHAPTER 3. Amine-rich polyelectrolyte multilayers for patterned surface fixation of metal nanostructures and proteins

Here, I describe a lithographic method for directly patterning the adhesive properties of an amine-rich layer-by-layer assembled polymer film. The film is useful for surface fixation of metal nanostructures and proteins. The adhesive regions in the film can be patterned with fairly harsh methods, using evaporated aluminum mask to protect selected regions of the substrate, and adhesion passivation on exposed regions with acetic anhydride. When the aluminum is removed with an HCl etch, the protected regions retain their adhesion, while adsorption of both particles and proteins is almost completely eliminated in the passivated areas, making it possible to guide adsorption to the patterned areas. The high degree of adhesion comes about due to uncoordinated amine groups that pervade the full thickness of the film. Cycling the pH through acidic

conditions and back causes the amines to be rearranged, rejuvenating the surface, which is the likely origin of the robustness of the adhesive properties to processing. pH adjustment also causes reversible swelling and deswelling of the film, so that the vertical position and dielectric environment of the nanostructure can be dynamically adjusted.

CHAPTER 4. Surface enhanced Raman spectroscopy

In Chapter 4, I describe a method to selectively modify the surface functionalization on triangular gold nanoparticles using their plasmonic properties. I used several custom made photoactivatable molecules and investigated the process of photoactivation with UV light using surface Raman spectroscopy as a diagnostic tool. I did not obtain clear evidence of photoactivation at the nanoparticle hot spots, due to several possible reasons, which are briefly discussed. I discuss future directions for the realization of the project.

CHAPTER 5. Two-photon activated two-photon fluorescence and binding of azidocoumarin in a gelatin matrix

I have studied the nonlinear optical properties of 7-azido-4-trifluoromethyl-1,2-benzopyrone (azidocomarin 151) contained in a gelatin gel matrix. As ultrafast light pulses are focused into the gel, onset of two-photon fluorescence is observed as two-photon absorption converts the azidocoumarin 151 into a fluorescent dye that binds to the gelatin. In the process of photoactivation discrete sites of modified azidocoumarin 151 molecules are selectively created. The method allows creating of patterned modification of the azidocoumarin 151. The rate of onset scales as the fourth power of the laser intensity, as it results from two two-photon absorption processes. I fit the time dependence of the fluorescence to a model that incorporates

the competition between coumarin photoactivation and photobleaching. From this fit, I estimate an upper bound for the two-photon cross section for photobleaching of the azidocoumarin 151 to be about 0.006×10^{-50} cm^4s at 720 nm.

1.2 Nano sphere lithography

Colloidal particles have been subject to extensive research in the fields of optics,[2, 3] chemistry and material science. Coatings of colloidal particles, consisting of single or multiple layers of densely packed nanoparticles, are of interest for applications such as antireflection coatings[4], photonic crystals[5], optical filters [6, 7], sensors [8, 9], porous membranes [10, 11], surface enhanced Raman spectroscopy (SERS) [12], fabrication of "patchy" nanoparticles [13], and nanosphere lithography.[14] Here I focus on spherical colloidal particles which can easily be assembled into long range periodic two-dimensional and three-dimensional colloidal arrays.[15, 16] 2D hexagonal lattices of colloidal spheres have been employed as ordered arrays of optical microlenses in image processing[17]. They are also used as physical masks for evaporation or reactive ion etching to fabricate regular arrays of micro or nanostructures. Furthermore, 3D opaline lattices of colloidal spheres have been exploited as removable templates to generate highly ordered microporous materials; as diffractive elements to fabricate sensors, filters, switches, and photonic band gap crystals,[18, 19]. A variety of methods have been developed to fabricate 2D or 3D colloidal arrays including sedimentation in a force field,[20] repulsive electrostatic interactions,[21, 22] spin drop casting,[23-26] and attractive capillary forces.[5, 19, 27] In applications where the goal is to produce thin films, containing three layers of colloids or less, and where polycrystalline ordering of the lattice is sufficient, convective assembly, also known as evaporation-induced self-assembly [1, 28-32], is probably the fastest and most convenient technique to implement. The method was first developed by Nagayama *et al.* [29, 32, 33] in which a

liquid suspension of nano or microspheres is spread onto a solid surface. As the liquid from the suspension slowly evaporates, capillary forces slowly drive the spheres to form closely packed 2D or 3D ordered structures. As originally conceived, the deposition method required a slow withdrawal of the substrate from the sphere solution. This deposition resulted in long deposition times, and required large volumes of colloidal suspensions.[29, 32, 33]

Velev *et al.*[1] proposed a faster method of deposition of mono or multi-layer of colloidal spheres, by dragging a meniscus of microliter suspension confined between two planes that move with respect to each other. The rate of withdrawal of the plates must match the rate of ordered crystal formation. The suspension, however, is more concentrated than that used in Nagayama's experiments, and therefore the withdrawal speed can be larger so that crystal deposition is faster. In my dissertation, I present a variation of convective self-assembly method, which is a modification of the method developed by Velev *et al.*[1]I refer to this method as restricted meniscus convective self-assembly. It creates the same quality of the deposited crystal as the conventional self-assembly method, but the speed of crystal deposition is faster.

1.3 Ionically self assembled multilayer films

Ultra-thin organic films are of high interest in areas such as integrated optics, sensors, and friction reducing coatings. [34] A lot of work has been done on surface modification by polymers in an attempt to extend the known versatility of polymer bulk materials to ultra-thin films and coatings. The self-organization of polymers has been exploited for the preparation of well-defined surfaces and interfaces extending the use of the established methods to low molar mass compounds[35-37].

One recent technique for fabricating thin films issurface functionalization techniques is the alternating physisorption of oppositely charged polyelectrolytes. This deposition technique is also known as “layer-by- layer” (LbL) method.

The building of an ISAM film is executed as follows. A negatively charged substrate such as a glass slide is immersed in a solution of a cationic polyelectrolyte. The adsorption is carried out in relatively high concentrations of polyelectrolyte. The adsorbed polymer molecules shield the surface charge of the substrate by forming a layer with reversed charge. After rinsing in pure water, the substrate is immersed in a polyanion solution, a monolayer is adsorbed and the surface again reverses its charge. Alternating immersions in both polyelectrolyte solutions result in building a multilayer assembly of both polymers.

The LbL technique has the advantage that the electrostatic attraction between opposite charges is the driving force for the multilayer build up. [38-40] In contrast to chemisorption techniques [41] that require a reaction yield of 100% in order to maintain constant surface density after each deposition step, no covalent bonds need to be formed. Furthermore, an advantage over the classic Langmuir-Blodgett technique [42] is that the adsorption processes are independent on the substrate size and topology. Because the nature of the film formation is ionic bonding, LbL built films are also referred to as Ionically Self assembled Multilayer (ISAM) films.

Poly (allylamine hydrochloride) (PAH), and poly (styrene sulfonate) (PSS) are two very well studied LbL polyelectrolytes [40]. I successfully deposited ISAM films as thin as 1 bi-layer, by using PAH/PSS as LbL polyelectrolytes. 1 bi-layer is formed by deposition of 1PAH layer and 1 PSS layer. Furthermore, the thickness of the ISAM film is linear with the number of bi-layers and can be controlled by adjusting the ionic strength of the solution from which the

polymers are adsorbed. For PSS, Lvov *et al*.[38] found that varying concentrations of NaCl salt added to the polyelectrolyte solution affects the thickness of each anionic/cationic bi-layer. As shown by Rubner *et al*.[43, 44] PAH/PSS ISAM films can also undergo a discontinuous volume-phase transitions. ISAM films fabricated with both dipping solutions at pH=8-9.5 undergo discontinuous swelling when exposed to low pH solution, and a subsequent shrinking when exposed to a solution of high pH. It was also found that after drying from the swollen state the film retains "memory" of its previous swelling state and returns to this specific level after immersing in DI water. This unique swelling behavior is associated with a pH driven degree of ionization of the weak polyelectrolyte PAH. In this film up to five times more PAH than PSS is used to form a layer in each PAH/PSS bi-layer. The extra PAH leads to excess number of amines present in the ISAM film. Amines are very common functional group used for surface fixation of nanoparticles, nanoassemblies,[45-50] and cellular studies,[51] both because of their positive charge and their ability for chemical coupling. The technique for LbL deposition was developed by Lvov *et al*.[38] He investigated the mechanism of LbL as well as the dependence of the thickness of the polymer layers on the ionic strength of the polyelectrolyte solutions.

In my dissertation, I show that I was able to pattern the surface adhesiveness of (PAH/PSS) ISAM films to selectively create areas with active sdhesiveness and areas with no sdhesiveness. This is done by acetylation with acetic anhydride. The areas of the film which were not treated with acetic anhydride have active amines and thus can be used for fixating molecules and nanoparticles to the film. In contrast the areas that have been treated with acetic anhydride do not have active amines and thus are not adhesive.

1.4 Surface Enhanced Raman Spectroscopy

A few decades ago it was discovered that Raman scattering intensity of pyridine on electrochemically roughened Ag was enhanced by a factor of ($\sim 10^6$).[52, 53] This discovery led to the emergence of Surface-Enhanced Raman Spectroscopy (SERS). SERS has very attractive advantages for the development of selective and sensitive analytical procedures. The technique combines the advantages of positive identification of a molecule in situ, well established instrumentation, and little or no sample preparation with very high levels of sensitivity.

Raman spectroscopy probes the unique vibrational signature of molecules, but it suffers from poor sensitivity due to the inherent weakness of the scattering process. The weakness of the Raman effect makes detecting the signal from a monolayer of adsorbed molecules on a surface difficult. Raman cross-sections are small ($\sim 10^{-29} - 10^{-30}$ cm^2 $molecule^{-1}$) in comparison to typical molecular optical absorption cross-sections ($\sim 10^{-15} - 10^{-16}$ cm^2 $molecule^{-1}$). Therefore for 10^{10} incident photons, only one will be Raman scattered. However, it was observed[52, 53] that there was strong enhancement from pyridine on electrochemically roughened Ag, this was an indication of an extra contribution from a surface effect. In the picture of Raman scattering, the incident EM field induces a dipole moment in the molecule which in turn radiates light at its oscillation frequencies. The induced dipole moment is a product of the molecular polarizability and the applied electric field. It follows that the enhancement of Raman intensity would arise from an increase of one of these factors. The factors affecting the Raman scattering due to their nature are referred to as chemical and electromagnetic.

The electromagnetic mechanism of SERS stems from the ability to excite localized surface plasmon resonances (LSPR) in metal nanostructures. The incident electromagnetic field couples to the collective oscillations of the conduction electrons across the surface of metal

nanoparticles or nanostructures. The resonant excitation results in strong enhancement of absorption and scattering of the electromagnetic field. The spectral positions of LSPR can be tuned by changing the composition, size, and material of the nanoparticles, because these factors affect their absorption and scattering properties.

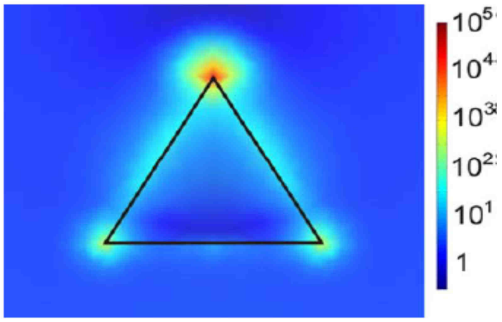

Figure 1.2 Finite element simulation of the enhancement *g* on the top surface of a triangular prism with side length of 200 nm. Light is incident normal to the figure and polarized vertically.

When excited on resonance, the nanoparticles' plasmon modes concentrate the incident light into localized areas on the surface of the particles, known as "hot spots". The hot spots are primarily located around sharp corners or nanoscale gaps between nanoparticles, as shown in Fig.1.2. A near field enhancement factor can be defined as $g = (E_{local}/E_0)^2$, where E_0 is the intensity of the incident light. The g factor can reach values of 10^4-10^7 times.[52, 54, 55] As I mentioned earlier, Raman scattering is a weak effect with low cross section for surface bound molecules. If the molecules are placed in the vicinity of the hot spots of metal nanoparticles or nanorough metal surface, the excited plasmon resonances lead to strong scattering from those molecules.

When a molecule, adsorbed on the surface of a metal nanoparticle, is irradiated with light, an oscillating dipole in the molecule is created which is enhanced by the metal substrate. In addition to enhancement of the incident field, enhancement of the emitted light from the induced

dipole is also possible. To a first order approximation, the overall enhancement factor from both incident and scattered fields can be described as EF= $4|g|^2|g'|^2$, where g' is the enhancement factor at the scattering frequency. For single molecule detection, enhancement of up to 10^{14} has been observed on nanoparticle clusters or fractal structures,[56, 57] making single molecule Raman detection possible. Therefore, in SERS the excitation and scattering wavelength can be in resonance with the LSPRs, thus the enhancement factor due to the plasmon resonance can scale with up to the fourth power of the local electromagnetic fields.

So far I focused on the EM nature of the Raman scattering, as it is the dominant mechanism, but a part of the enhancement is due to what is known as a chemical enhancement. Chemical enhancement arises from direct interaction between the adsorbed molecule and the metal surface, resulting in an increase in the Raman cross-section.[55, 58] Chemisorption, or bond formation between the molecule and the surface, perturbs the electronic structure and therefore the optical properties of the molecule compared to its unbound state. Another way in which the Raman cross-section may be affected by electronic effects is through charge transfer between the adsorbed molecule and the surface.[59-61] If the absorbance maximum of an adsorbed molecule is altered such that it is closer to the laser excitation frequency, the Raman cross-section of the molecule is increased. Thus, the chemical mechanism can be understood as a type of resonant Raman Effect.

1.5 Two photon activation

The term “optical highlighter” describes molecules that are initially non fluorescent, but become fluorescent after photo-activation with light. Molecule photoactivation is used for a relatively new method of imaging referred to as super resolution imaging. Super resolution imaging can obtain signal from spatial distribution of fluorescent molecules on length scales shorter than the classical diffraction limit. In these methods image is constructed from high-accuracy localization of individual fluorescent molecules that are switched on and off using light of different wavelengths. The imaging process consists of imaging cycles during each of which only a fraction of the fluorophores in the field of view are activated such that each of the active fluorophores is optically resolvable from the rest. This allows the position of those fluorophores to be determined with high accuracy. Repeating this process for multiple cycles, each causing different subset of fluorophores to be turned on, allows the position of many fluorophores to be determined and thus an overall image to be reconstructed. In addition to such techniques known as PALM,[62] FPALM,[63] and STORM,[64] two-photon activation offers an alternative to photo bleaching approaches in the study of protein kinetics, gene expression, and cellular dynamics. Photoactivation occurs with absorption of an UV photon, or absorption of two photons, each carrying half the required energy for photoactivation. The two photon photoactivation is a nonlinear process with efficiency scaling with the light intensity. This means that the activation process will be only limited to the volume localized around the light beam. With two photon activation 3D superresolution microscopy can be carried in bulk. The two photon process as it requires low energy wavelengths, is less damaging to tissue samples and allows for deeper imaging.

Other than imaging, two-photon activation can be used for micro-fabrication, which is why it is of interest to my thesis. Two-photon polymerization,[65, 66] for example, is carried in photosensitive gel by focusing and scanning with a laser. The photoactivatable molecules in the path of the beam will transform and crosslink in a 3D pattern inside the gel. Arylazides are an example of a class of photoactivatable compounds. In my dissertation, I study the photoinduced polymerization of Coumarin 151 in gelatin gel. I chose Coumarin 151 because it easily forms bonds with the gelatin gel matrix to create fluorescent pattern, and is less studied than Coumarin 120, but also because the chemical structure redshifts the absorption band facilitating the overlap with the wavelength of our laser.

CHAPTER 2 Restricted Meniscus Convective Self-Assembly

2.1 Introduction

In one standard version of this technique, illustrated in Fig. 2.1(a), a plate is placed at an acute angle immediately above the substrate, and a small volume of nanoparticle suspension is placed in the corner formed by the plate and substrate. The plate is then withdrawn at a velocity v_w, dragging the suspension and a thin wetting film attached to the suspension with it. Evaporation from the film induces a flow J_W of solvent toward its edge. Particles are pulled along with the flow, which drives the growth of a thin colloidal crystal with one or more layers. Uniform films can be deposited on multiple square centimeters in a few minutes with this technique.

In our version of the technique, illustrated in Fig.2.1(b), the meniscus of the solvent is restricted by placing a straight-edge above the substrate just before the drying zone of the film. This can be accomplished simply by running the setup just described in reverse so that the upper contact line of the fluid meniscus from which the film grows is attached along the bottom edge of the angled plate. I will call this growth mode Restricted Meniscus Convective Self-Assembly (RMCSA) to distinguish it from the conventional configuration, where the upper contact line is free to attach anywhere along the flat side of the plate. Since both modes can be accommodated with the same apparatus run in opposite directions, I will use negative withdrawal speeds (v_w) to denote RMCSA and positive for conventional CSA.

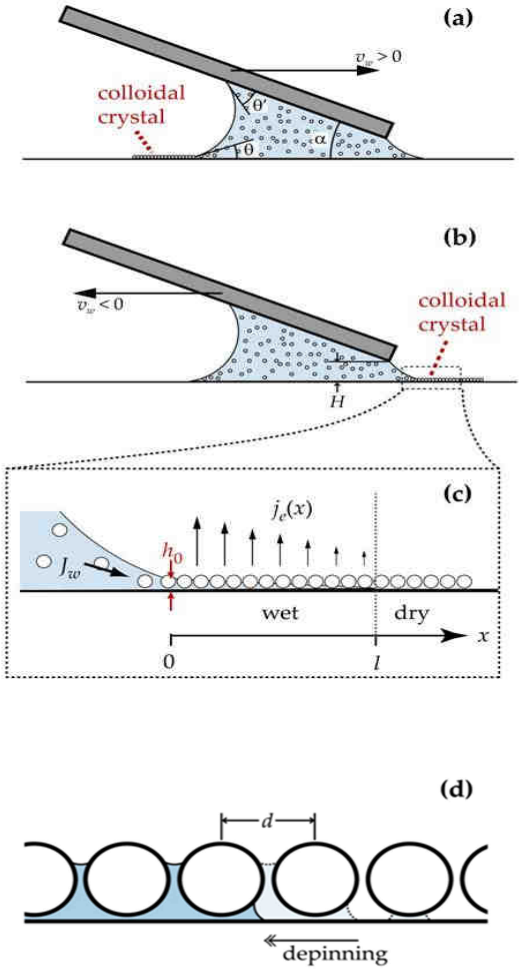

Fig2.1. **Schematic of restricted meniscus convective self assembly**

(a) conventional convective self-assembly. The colloidal crystal forms from a meniscus where the upper contact line is free to move along the flat surface of the angled plate. I denote this with positive withdrawal velocities v_w.

(b) restricted meniscus convective self-assembly. The colloidal crystal grows from a meniscus where the upper contact line is fixed at the lowest corner of the angled plate. I denote this mode with negative withdrawal velocities. This mode grows crystals at roughly twice the rate of the conventional approach.

(c) the drying zone of the colloidal crystal. A wetting film from the suspension extends into the crystal from $x = 0$ to $x = l$. Water evaporates from the film at the rate $j_e(x)$, which in steady state is replaced by a flow J_w from the suspension, pulling nanospheres toward the edge of the crystal, causing it to grow.

(d) The far edge of the wetting film, which marks the boundary between the wet and dry portions of the colloidal crystal, is likely fairly abrupt, as illustrated by the figure. The boundary may move in discrete steps as it gets depinned from the last wet row of nanospheres in a step-wise fashion. Some fluid may be left behind on the nominally dry side of the boundary. If either the conditions required to initiate a depinning event or the amount of fluid left behind after depinning depend on the withdrawal velocity v_w, this could change the scaling of the drying rate from the results expressed by Eqs. 8 and 9.

2.2 Experimental

Au pellets (99.999% pure) and Ni pellets (99.98% pure) were obtained from Kurt J. Lesker (Clairton, PA). Surfactant free white carboxyl polystyrene latex nanosphere suspension (784nm diameter, 4.2 % w/v) was purchased from Invitrogen (Carlsbad, CA). Unless otherwise noted, the nanoparticles were concentrated by centrifugation to 21% w/v prior to use. Plain precleaned glass slides and all chemicals were purchased from Fisher (Pittsburgh, PA).

Following Prevo and Velev [1], the particle suspension was deposited between the substrate and a metal plate mounted at a 22.5° angle above the horizontal. The plate was mounted on a vertical positioning stage (Thorlabs p/n PT1A) so that the spacing between plate and substrate could be controlled with μm precision. To ensure that the bottom edge of the plate was parallel to the substrate, a goniometer stage (Thorlabs p/n GNL18) was also incorporated in the setup so that the horizontal alignment of the plate across the substrate could be adjusted.

The substrates consisted of standard precleaned 1"×3" microscope slide (Fisher Scientific) which were first cleaned by the RCA process [67], *i.e.* immersion in a 1:4:20 solution of NH_4OH : H_2O_2 : H_2O at 80±5 °C for 15 min, followed by a 1:1:5 solution of HCL : H_2O_2 : H_2O at 80±5 °C for an additional 15 min. These mixtures are highly corrosive and the appropriate protective equipment must be worn while handling them. Between and after the immersion steps, the slides were rinsed with copious amounts of DI water and then stored in DI water until used. Two metal contact strips, approximately 2-3 mm wide, were fabricated along both long edges of each substrate. This was done by covering the center of the side with a 20 mm wide strip of aluminum foil, followed by e-beam vacuum deposition of 50 Å Ni and 1000 Å Au. Water contact angle measurements indicated that the evaporation process rendered the surfaces less

hydrophilic than right after RCA cleaning. For this reason, the evaporated samples were briefly ultrasonicated in a 1:1:6 - NH_4OH: H_2O_2: H_2O solution and then in a 1:1:5 - HCl: H_2O_2: H_2O solution, which restored the original hydrophilicity to the surface.

Just prior the use, each substrate was blow dried with dry nitrogen and mounted horizontally on a computer controlled motion stage (Thorlabs p/n Z625B) just below the angled plate. The orientation of the plate was adjusted with the goniometer stage so that lowering the plate to bring it in contact with the substrate would cause the plate to make simultaneous electric contact with the two contact strips on the substrate. The plate was then withdrawn to between 10 μm and 200 μm from the substrate and kept at that distance throughout the deposition.

The entire setup was kept inside an airtight enclosure. Dishes filled with either warm water or $CaSO_4$ desiccant were placed inside the enclosure for whatever time was required to adjust the relative humidity to the desired value. The temperature in the laboratory was maintained at 21±1 °C. A few μl of concentrated nanoparticle suspension was then placed between plate and substrate, at which point the substrate was displaced either in the forward direction (Fig 2.1(a)) for conventional CSA, or the backward direction (Fig 2,1(b)) for RMCSA.

2.3 Theory

As explained by Dimitrov and Nagayama [29], convective self-assembly occurs due to evaporation from a wetting film that extends into the colloidal crystal from the three-phase contact line between the suspension and the film. See Fig. 2.1(c). I denote the total evaporative flow per unit width across the length of the film as J_E. In steady state, the evaporated water is replaced by a flow of water $J_{W0} = J_E$ from the suspension. This flux carries a particle number

flow $J_N \propto J_{W0}$ along with it, which gets deposited at the leading edge of the colloidal crystal. If the withdrawal speed is chosen appropriately, a uniform film with crystalline order is formed. For example, a hexagonal closepacked monolayer forms if $v_w = v_c^{(1)} = \frac{\sqrt{3}}{8}\pi d^2 J_N$, where d is the diameter of the nanoparticles. In general, then, we have that $v_w = \left(\alpha/h_0\right) J_{W0}$, where α is a unitless constant of proportionality that depends on the structure of the colloidal crystal and h_0 is the thickness of the wetting film at the growing edge of the crystal. The flow J_{W0} is driven by the gradient of the pressure $p(x)$ inside the wetting film, which can written as

$$p(x) = \Pi + P_{pc} \tag{1}$$

where Π is the disjoining pressure between the air-liquid and liquid-solid interfaces in the wetting film, and P_{pc} is the capillary pressure due to the menisci formed between the nanoparticles submerged in the film. Both Π and P_{pc} depend on the average local thickness $h(x)$ of the wetting film, where x denotes the distance to the three-phase contact line. At $x = 0$, the pressure must equal the pressure in the nanoparticle suspension

$$p(0) = P_c + P_h \tag{2}$$

where P_c is the capillary pressure due to the meniscus between the angled plate and the substrate, and P_h is the hydrostatic pressure at the level of the substrate.

The lateral fluid flow $J_W(x)$ in the wetting film decreases with increasing$x$, and is related to the local evaporation flux $j_e(x)$ by

$$J_W(x) = \int_x^l j_e\big(h(x)\big)dx' \tag{3}$$

where l is the length of the wetting film in the x-direction. Elaborating on Dimitrov and Nagayama's model, I note that since we are dealing with low Reynolds number flow through a porous medium, Darcy's law is valid, and we can write

$$J_W(x) - h(x)v_w = -h(x)\frac{\kappa}{\mu}\frac{dp}{dx} \tag{4}$$

where κ is the permeability of the colloidal crystal to the wetting film, and μ is the dynamic viscosity of the fluid. The $h(x)v_w$ term accounts for the global motion of the liquid suspension relative to the colloidal crystal.

To proceed, some assumptions about the relationship between the pressure $p(x)$ and the film thickness $h(x)$ need to be made. This is a complex problem beyond the scope of this dissertation, so I restricted myself to examining two limiting cases which I will denote as the *pressure driven* and *pressure independent* limits, respectively.

In the pressure driven limit, h is completely determined by p, and explicit dependencies on other parameters can be neglected, so that $h = h\big(p(x)\big)$. This means that the thinning of the wetting film as I move into the film from the three-phase contact line occurs only in response to the increasingly negative p required to maintain a non-zero liquid flow through the crystal. The length l of the wetting film is then strongly dependent on J_{W0}, and for the static case, where $J_{W0} \equiv 0$, l goes to infinity. In the pressure driven limit, we can rewrite Eq. 4 to obtain:

$$-\frac{\kappa}{2\mu}\frac{dp}{dh}\frac{d}{dx}(h^2) = \int_x^l j_e dx' - \frac{\alpha h}{h_0}\int_0^l j_e dx', \tag{5}$$

subject to the boundary conditions that $h(0) = h_0$ and $h(l) = 0$. Solving this equation yields $h(x)$, which determines all other relevant quantities. As mentioned, doing so explicitly is beyond our current scope, but I can still extract the scaling behavior of the solution by writing Eq. 5 in dimensionless form. To do this, we make the substitutions

$$\begin{aligned} x &= l \cdot s, \\ h(x) &= h_0 \cdot \theta(s), \\ j_e(h) &= j \cdot \zeta(\theta), \\ \left(\kappa\frac{dp}{dh}\right)[h] &= -\mathrm{c} \cdot \gamma(\theta), \end{aligned} \tag{6}$$

where j is the evaporation rate from a free liquid surface and c is chosen so that $\gamma(\theta)$ is dimensionless and approximately $\in [0,1]$. Eq. 5 and its boundary conditions can then be written as

$$\begin{gathered} \left\{\frac{ch_0^2}{jl^2}\right\}\gamma\frac{d}{ds}(\theta^2) = \int_s^1 \zeta ds' - \alpha\theta\int_0^1 \zeta ds'; \\ \theta(0) = 1; \qquad \theta(1) = 0. \end{gathered} \tag{7}$$

The quantity in the curly brackets is fixed by the boundary conditions, and therefore embodies the scaling of the equation. Noting that $J_{W0} \propto jl$ and that $j \propto (1 - RH)$, where RH is the ambient relative humidity, we find that

$$v_c^{(1)} \propto h_0\sqrt{c(1-RH)}. \qquad \text{(pressure driven limit)} \tag{8}$$

In the pressure independent limit, $p(x)$ has negligeable effect on $h(x)$, and the form of $h(x)$ can be found by energy minimization in the static case. The variations in $p(x)$ that are required to sustain a flow through the film is created by small changes in the configuration of the surface of the wetting film that do not appreciably affect $h(x)$. l is now a constant that is independent of J_{W0}, and therefore largely independent of the evaporation rate and the withdrawal velocity. I can therefore write that

$$v_c^{(1)} \propto h_0(1 - RH). \qquad \text{(pressure independent limit)} \qquad (9)$$

So far, I have assumed that the wetting film height h varies only slowly with x. This is probably not true at the far edge of the film (where $h(l) = 0$). More likely, the situation is closer to the sketch in Fig 2.1(d), where the wetting film contact edge is pinned at a specific row of nanoparticles, and h rapidly changes from a finite value to 0. Movement of the contact line to the left is impeded by the energy barrier associated with dewetting the last line of nanospheres and moving the surrounding fluid one particle diameter to the left. This occurs when the thickness of the wetting film reaches a critical value h_{min}. In terms of my model this corresponds to replacing the boundary condition at $x = l$ with $h(l) = h_{min}$. At low withdrawal velocities, I expect h_{min} to be constant and independent of v_w. As a result, the scaling of $v_c^{(1)}$ remains as announced in Eq. 8 and 9, even though I have needed to slightly modify our model.

Another complication would occur if some amount of fluid were left behind on the uncovered spheres during depinning, so that $J_W(l) \neq 0$. If this quantity is constant I have that $J_W(l) \propto v_w$, and Eq. 8 and 9 still express the correct scaling, but if it varies with withdrawal speed, the scaling will be affected.

Before I present the experimental results, I will also note that in addition to parameters such as withdrawal speed, humidity, surface tension, and substrate wettability, I was also able to modify the pressure $p(0)$ in the particle suspension by simply changing the volume V of the suspension placed between the angled plate and the substrate. If we neglect P_h as well as the small effect the restricted meniscus has on V, we get that

$$P_c = \gamma \cdot \sqrt{\frac{w}{2V} g(\alpha, \theta, \theta')} \tag{10}$$

simply by geometrically relating the volume trapped under the plate to the radius of the free meniscus and to the contact angles, and then applying the Young-Laplace equation. Here, w is the width of the substrate, γ is the surface tension, and

$$g(\alpha, \theta, \theta') = \frac{(1 + \cos(\alpha + \theta + \theta'))(\cos\alpha + \cos(\theta - \theta'))}{\sin\alpha} + \alpha + \theta + \theta' + \sin(\alpha + \theta + \theta') - \pi \tag{11}$$

is a geometric factor that depends on the angle α between the angled plate and the substrate, and on the upper (θ') and lower (θ) meniscus contact angles (see Fig. 2.1). For my setup, $g(\alpha, \theta, \theta') = g(22.5°, 11°, 31°) = 5.85$.

2.4 Results and Discussion

The results from a number of RMCSA and conventional CSA experiments all carried out with the same nanoparticles but at varying v_w and relative humidity are shown in Fig. 2.2. For each value of the humidity, there is a critical withdrawal speed $v_c^{(1)}$ above which only submonolayer colloidal films form, but below which the films will consist of one or more

closepacked monolayers. For uniform monolayer films, free of inclusions of thicker or thinner films, v_w must lie within a few % of $v_c^{(1)}$. Similar critical withdrawal speeds exist for two- and three-monolayer films [1], but this region of phase space was not explored in my work. Fig. 2.3 shows micrographs of several films fabricated with v_w values near $v_c^{(1)}$. If v_w is appreciably larger than $v_c^{(1)}$ small submonolayer patches are included in the closepacked monolayer film, but if v_w is too small, bands of bilayer film appear.

From the data in Fig. 2, I made several observations; first, RMCSA is about twice as fast as conventional CSA for fabrication of single monolayer close packed colloidal films. Second, both CSA and RMCSA growth rates depend fairly strongly on ambient humidity, displaying linear scaling in $1 - RH$ consistent with the pressure independent limit. This is at variance with the work by Prevo and Velev [1, 31] who reported only weak dependence of the growth rate on humidity. It is possible that they were working closer to the pressure driven limit, which would lead to a fairly weak dependence of $v_c^{(1)}$ on humidity for RH below 50%.

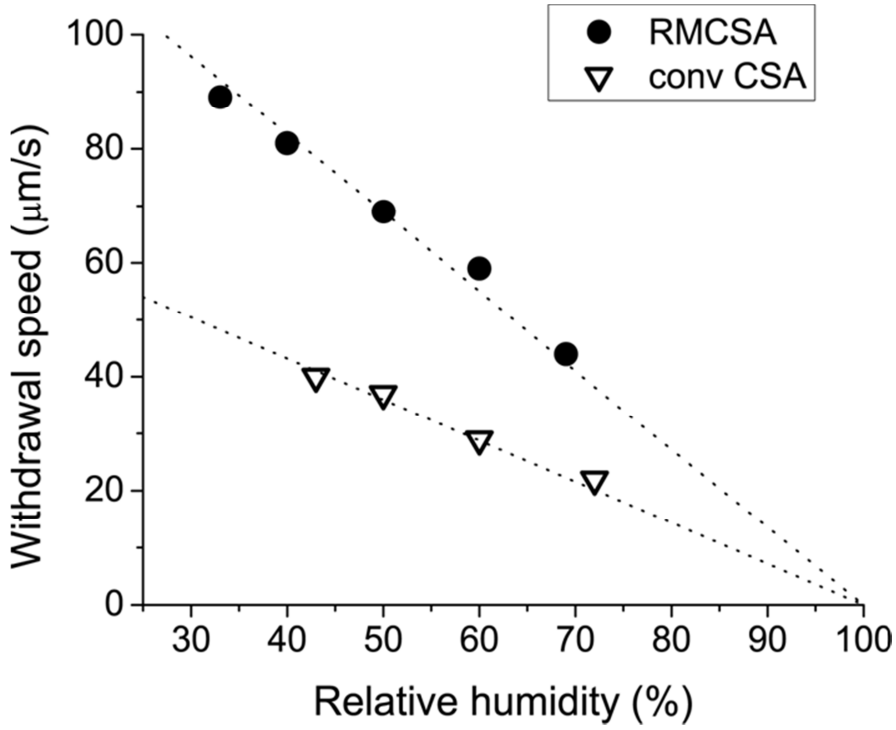

Figure 2.2 Plot of $v_c^{(1)}$, the withdrawal speed for generating uniform closepacked monolayer crystals with CSA as a function of relative humidity for conventional CSA and RMCSA. The dotted lines are approximate fits of the data to Eq. 9.

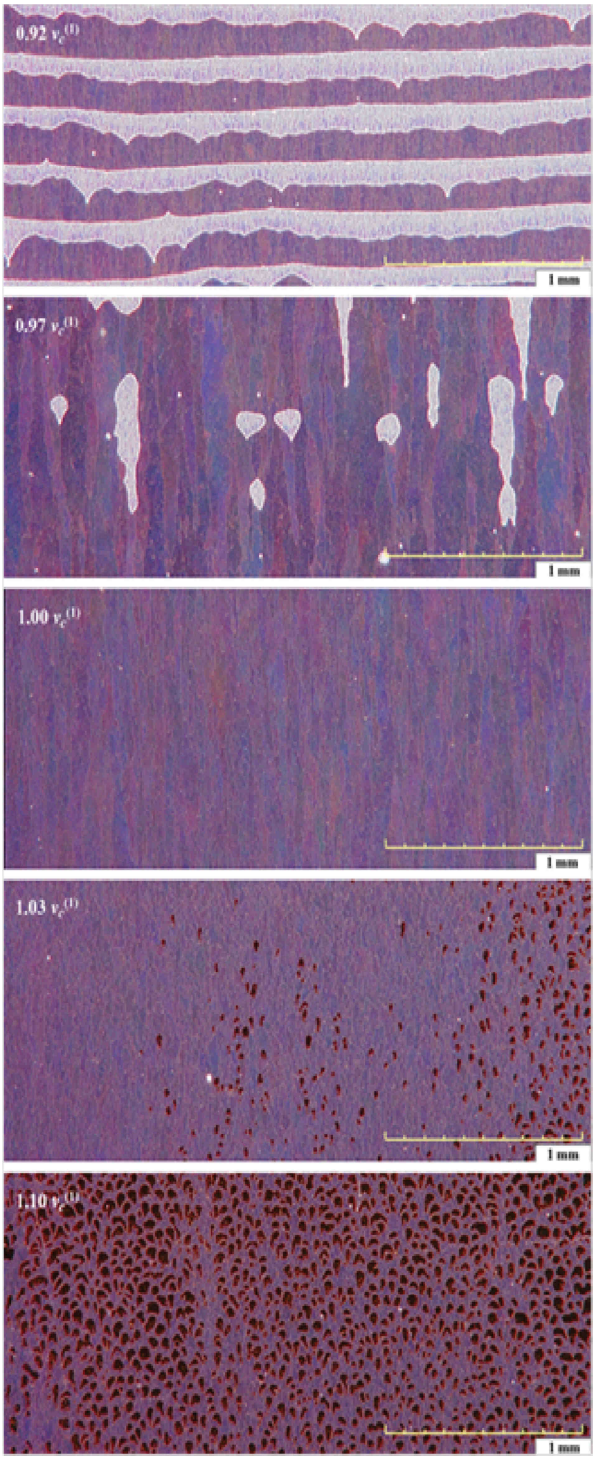

Fig 2.3 Micrographs of colloidal crystal films fabricated with withdrawal speeds near $v_c^{(1)}$ The closepacked monolayer regions appear as iridescent purple, bilayer regions are white, while submonolayer regions are dark. Deviating more than a few percent from the ideal withdrawal speed leads to submonolayer or bilayer inclusions into the crystalline film

The notion that I was operating close to the pressure independent limit is also supported by the data shown in Fig. 2.4(a). Here, $v_c^{(1)}$ was measured as a function of relative humidity for three suspensions with varying amount of the surfactant Triton X-100 added. The surfactant improved the wetting properties of the suspension, making it easier to fabricate uniform colloidal crystals over multiple square centimeters. [29] Without the surfactant, the high surface tension of the wetting film has a tendency to break it up into stripes as the assembly proceeds, as is shown in Fig. 2.5. Adding surfactant also made the substrate cleaning process much less critical for crystal growth. Parenthetically, it is worth mentioning that the Triton-X surfactant slowly softens the polystyrene nanospheres, so a suspension should be used within a few days of the addition of the surfactant, or the spheres may deform into hexagons (Fig 2.4) during the convective self-assembly. The image also illustrates the fact that the capillary forces among the spheres are quite strong during the crystal formation.I measured the surface tension of the suspensions using the pendant drop method, and found 65.2 mN/m, 31.7 mN/m and 31.0 mN/m for the 0 mM, 1 mM and 10 mM Triton X-100 suspensions respectively, which is consistent with values in the literature.[68] Fig. 2.5(a) shows that the addition of the surfactant has only a slight effect on $v_c^{(1)}$, even though it strongly effects the surface tension. This indicates that $h(x)$ and therefore l are largely unaffected by capillary forces.

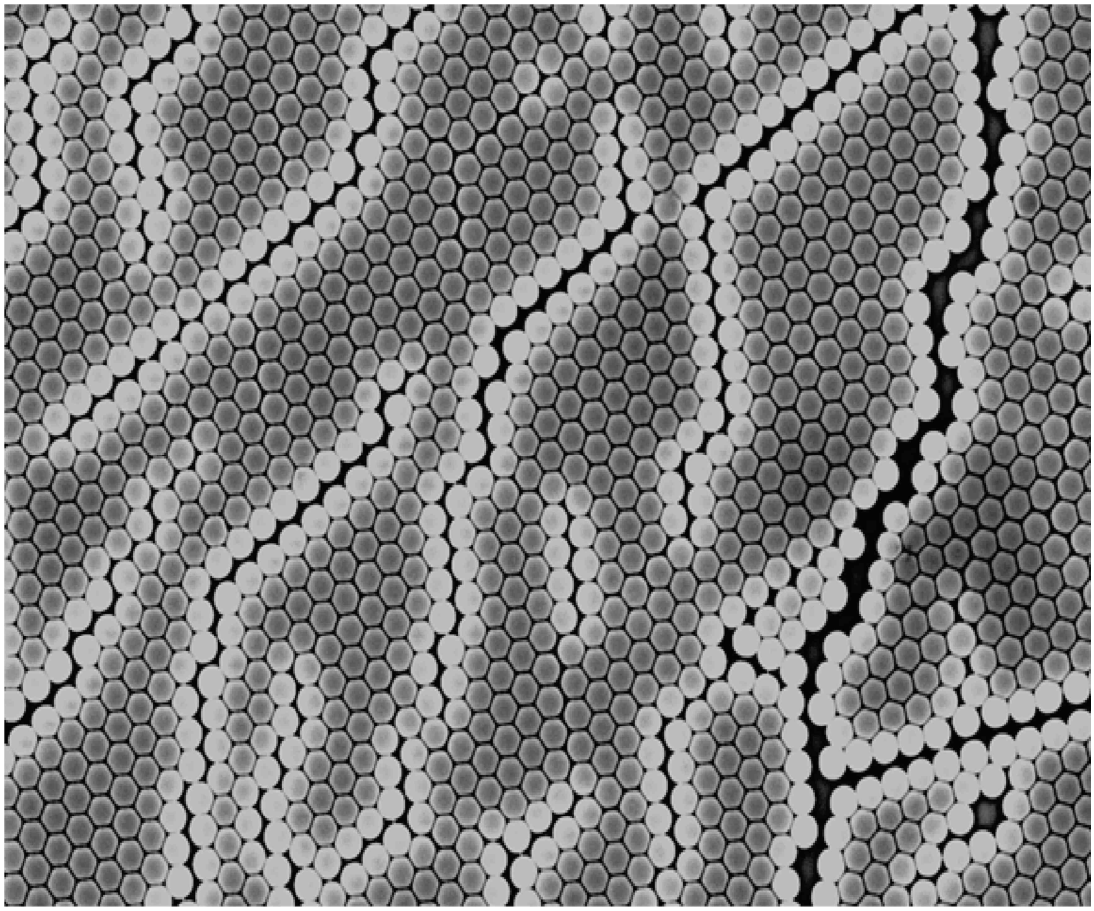

Figure. 2.4 SEM image of polystyrene spheres deformed while assembling in a monolayer crystal after prolonged exposure to Triton X-100

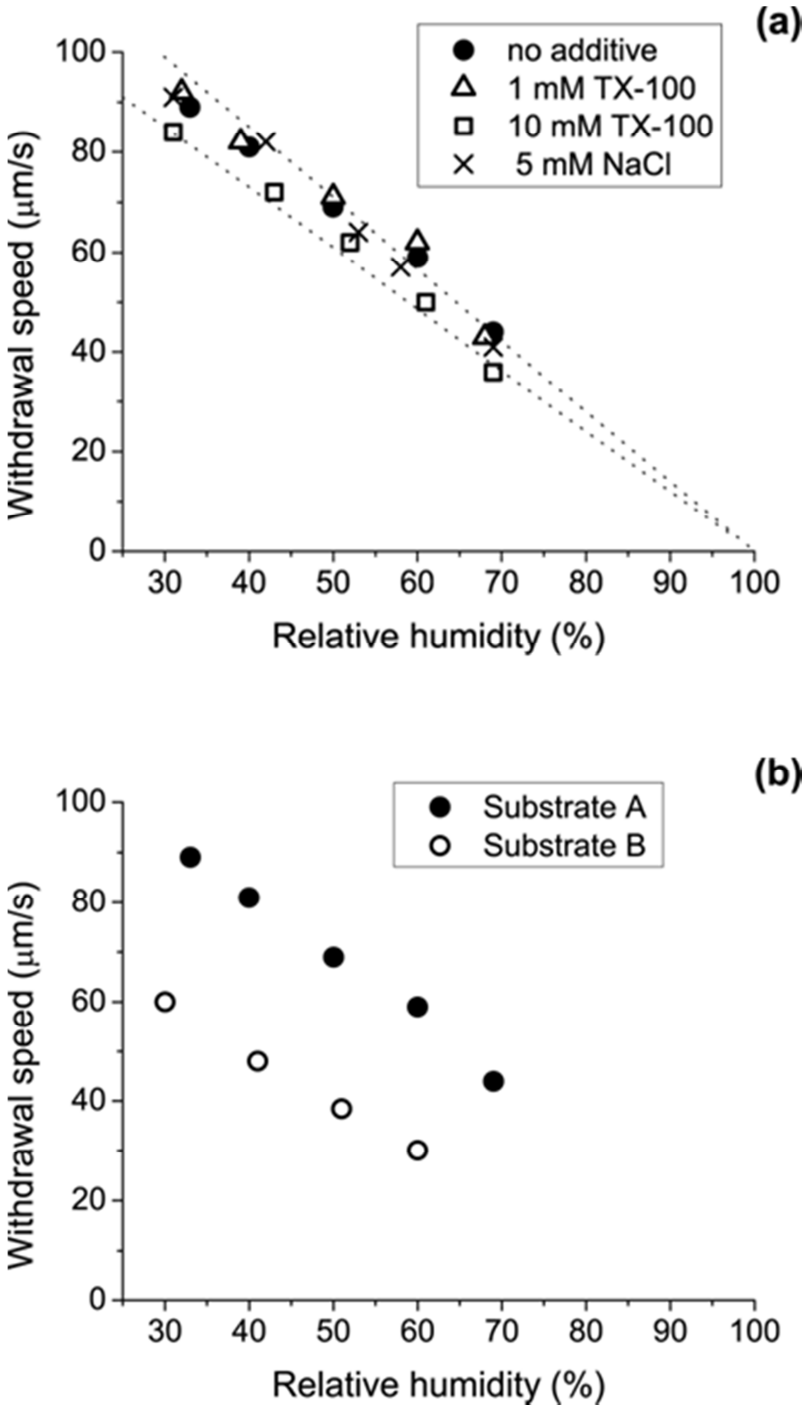

Figure 2.5. Plots of $v_c^{(1)}$ versus relative humidity for RMCSA using (a) nanoparticle suspensions with additives designed to lower capillary pressure (Triton-X 100) and the electrostatic portion of the disjoining pressure (NaCl). (b) substrates with different degrees of wettability. Substrate A has an 11° water contact angle, while substrate B has a 29° water contact angle.

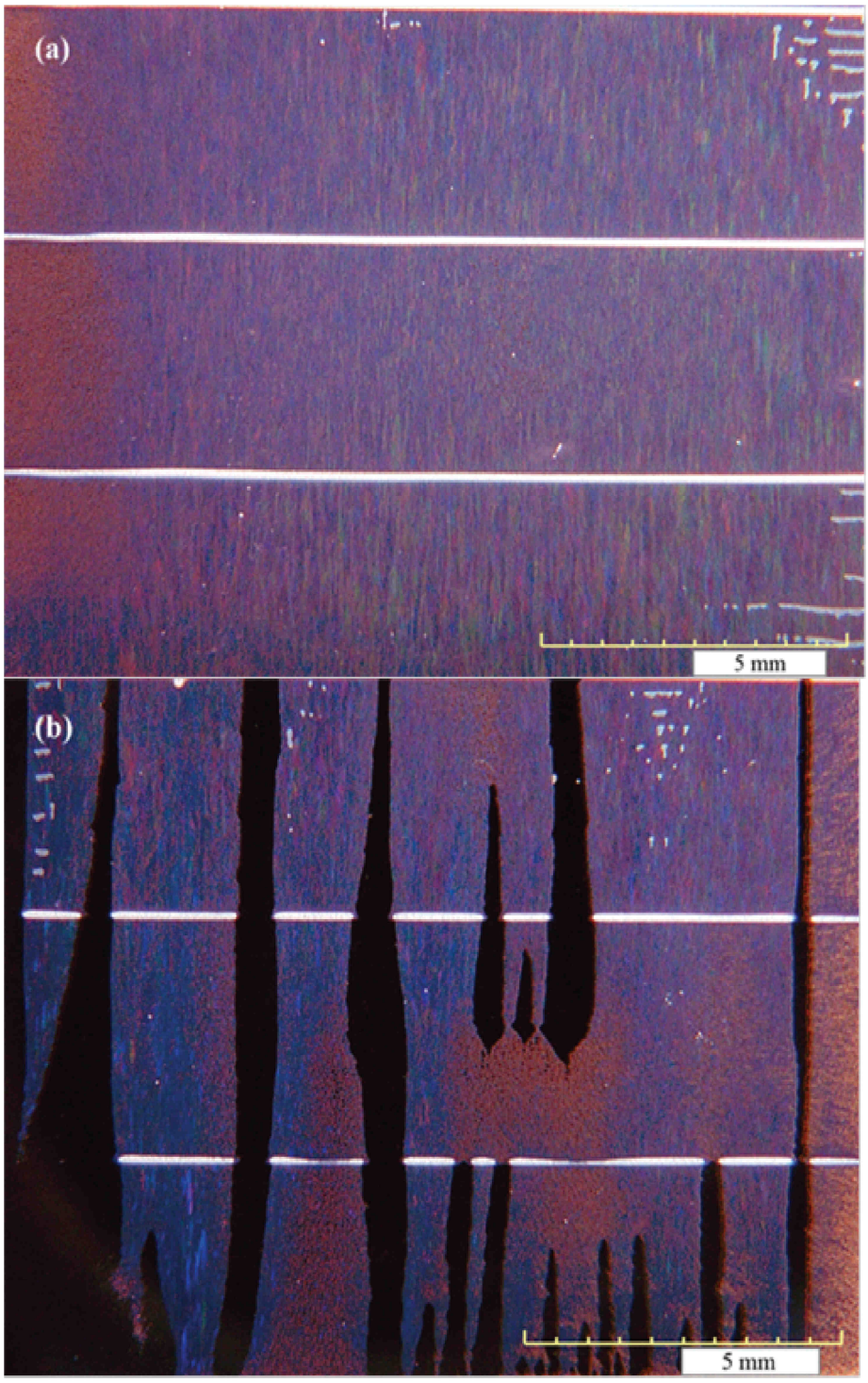

Figure 2.6. Photographs of colloidal crystals (a) of high quality, (b) containing bare stripes. The addition of a surfactant such as Triton-X 100 to the suspension reduces the probability of stripes appearing. The horizontal white stripes are places where the withdrawal was stopped for a few seconds in order to create a recognizable boundary between regions grown with different withdrawal speeds.

Since Triton X-100 is a nonionic surfactant, it is not clear that its presence changes the disjoining pressure Π much. It is also conceivable that the flow through the wetting film is predominantly driven by variations in Π and that P_{pc} plays only a minor role. For this reason, I also measured $v_c^{(1)}$ vs RH for a suspension containing 5 mM of NaCl. The salt strongly reduces the electrostatic component of Π, [69] which is likely to dominate at the length scales that are relevant in the colloidal crystal. The only visible effect of the salt on the crystal formation is to reduce the size of the submonolayer patches when v_w is larger than $v_c^{(1)}$, but as can be seen in Fig 2.5(a), it has no measurable effect on the value of $v_c^{(1)}$ itself.

It is clear that the parameters that determine $p(x)$ have only minor influences on $v_c^{(1)}$, as one would expect if operating in the pressure independent limit. By contrast, changing the wettability of the substrate has a strong impact. Fig. 2.5(b) plots measurements of $v_c^{(1)}$ vs RH on two glass substrates with different surface preparation. Substrate A was subjected to the standard cleaning procedure described above, rendering it quite hydrophilic (11° water contact angle). For substrate B, the cleaning steps after contact evaporation were omitted, which resulted in a less hydrophilic surface (29° water contact angle). This corresponds to a 12% increase in the surface free energy of wetting, much smaller than the change in surface tension due to the addition of surfactant, but nonetheless resulting in a reduction in $v_c^{(1)}$ on the order of 40%.

I will now attempt to explain the difference in self-assembly speed between conventional CSA and RMCSA. I first note that the details of the flow depend only on what happens in the wetting film and its immediate vicinity. I would therefore expect that the dynamics of the film growth is largely independent of the distance H between the angled plate and the substrate. This was indeed observed experimentally, as is shown in Fig. 2.7(a). Similarly, the film pressure $p(x)$

can, as I have already noted, be shifted by changing the volume of the particle suspension placed between the angled plate and the substrate. I varied between 2 ml and 30 ml, which, using Eqs 10 and 11 and 65.2 mN/m, corresponds to values between 0.10 kPa and 0.40 kPa. is negligibly small in this regime. As can be seen in Fig. 2.7(b), this had no impact on

.

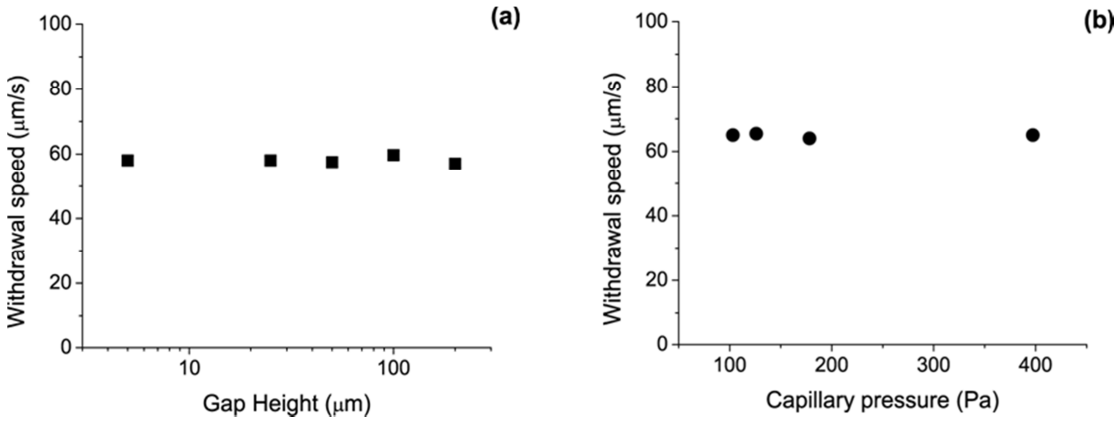

Figure 2.7. Plots of $v_c^{(1)}$ versus (a) the height of the angled plate above the substrate and (b) the capillary pressure in the suspension as controlled by the volume of liquid.

These results show that the difference in growth rates between CSA and RMCSA cannot be due to any difference in between the growth modes (for instance due to different advancing and receding contact angles changing the radius of the unrestricted meniscus). Nor is it likely due to any constriction in the flow inside the suspension caused by the presence of the angled plate. With the factors excluded, the only remaining explanation for my observations is a difference in evaporation rate between the two cases. Even if the relative humidity far from the film is the same in both modes, the shapes of the spaces through which the evaporated water must diffuse after it leaves the wetting film are quite different. Since the RMCSA configuration is more open toward the environment, the humidity at the wetting film surface is likely to be closer to the

humidity far away from the film than in the case of conventional CSA. The evaporation rate j_e is therefore higher for RMCSA, and as I have already established, this means that the colloidal film growth rate also must be higher for RMCSA.

2.5 Practical RMCSA

Producing good results with RMCSA requires following several basic procedures. All substrates that are used for the deposition need to be RCA cleaned. This is very important especially when the substrate is first functionalized, with ISAM film for example. The restricting plane, which defines the upper confinement line for the nanosphere suspension, is a microscope glass slide that has to be cleaned well before every deposition. Thorough rinse with DI water and consequent blow dry are very important for proper deposition, and the glass slide can't have any chips on the edge that will affect the deposition process and lead to lower quality crystal. The distance between the upper restrictive plane and the substrate should be roughly 1.5 times the diameter of the polystyrene spheres used for the deposition. The nanosphere suspension changes its concentration with time due to evaporation, so the life of a freshly made 20% suspension is approximately two weeks.

2.6 Conclusion

I have compared the crystal growth rates of two different forms of convective self-assembly, which differ only in the attachment of the upper contact line of the meniscus from which the crystal is grown. Contrary to expectations, I find that the growth rates of the two modes differ by as much as a factor of two. After excluding other explanations, I attribute this to

different evaporation rates from the wetting films in the two cases, which in turn is due to the difference in shape between the spaces through which vapor must diffuse away from the films.

I have also examined colloidal crystal formation as a function of ambient relative humidity for nanoparticle suspension with different amount of surfactant and salt added. To my knowledge, this is the first time such a study has been undertaken. My results indicate that the profile and length of the wetting film permeating the growing crystal is largely independent of the pressure inside the film and thereby also of parameters such as ambient humidity, surface tension and suspension ionic strength. The size and type of nanoparticles used as well as the wettability of the substrate are however quite important. As a results of this behavior, the growth speed of a closepacked monolayer colloidal crystal scales approximately as $1 - RH$ where RH is the ambient relative humidity.

My result underscores the complexity of the physics of convective self-assembly, and how phenomena on multiple length scale must be considered in order to properly describe it. The simple model I have presented here partially explains the humidity dependence of the growth rates, but more detailed studies, both experimental and theoretical, are needed if a more complete understanding is to emerge.

CHAPTER 3 Amine-rich polyelectrolyte multilayers for patterned surface fixation of metal nanostructures and proteins

3.1 Introduction

Full realization of all the promises of nanotechnology will require merging top-down and bottom-up fabrication technologies. For instance, accurate spatial positioning of bottom-up fabricated nanoparticles and nanoassemblies provided by top-down lithographic methods will become necessary in all but the simplest devices and systems. A similar interest in controlling the positioning of living cells exists for applications such as tissue engineering, biosensors and cellular studies. Both cells and nanostructures are generally quite fragile and typically cannot withstand the processing conditions of most forms of lithography. This limitation can be overcome by instead patterning the adhesive properties of a substrate, so that adsorption of nano- or bio-structures at desired locations can be the very last step in the fabrication process.

As the adhesive properties of a surface are themselves quite sensitive, creating patterns of adhesion is a non-trivial task. One method to accomplish this is to use standard lithographic processing to prepattern the surface with materials such as gold that can be thoroughly cleaned and functionalized orthogonally from a glass or silicon substrate to selectively bind desired structures. Lift-off of layer-by-layer (LbL)[70] or spun-on[71] films are other ways to achieve the same goal. Soft lithography techniques such as microcontact printing,[72, 73] dip-pen nanolithography,[74] or microfluidic patterning[75] are quite popular. Other techniques to create

surface patterns of particles or cells include electrostatic patterning,[76] dielectrophoresis,[77, 78] and even patterning with magnetic fields.[79]

In this chapter, I show that the adhesive properties of ionic self-assembled multilayer (ISAM) films that are rich in amine groups are sufficiently robust that they can be patterned by a much harsher technique; by using an evaporated metal mask to protect the surface from chemical passivation with acetic anhydride, followed by removal of the mask by wet-etching. To my knowledge, this is the first time adhesion patterning has been demonstrated with this approach. The robustness stems from the fact that most of the amine groups in the film are coiled up into hydrophobic regions, buried in the bulk of the film, or both. As described below, the amines can be rearranged by modulating the film pH, which makes it possible to at least partially rejuvenate the film, removing damage and fouling in a way that is not available, for example, in a silane monolayer.

The lithographic process is illustrated in Fig. 3.1. First, an amine-rich ISAM film is deposited on the charged substrate (Fig. 3.1(a)). An aluminum mask is patterned on the film (Fig. 3.1(b)). Here, I use an array of nanostructures fabricated with nanosphere lithography,[14] one of the easiest ways to create nanoscale patterning on a surface. The nanospheres that served as an evaporation mask for the metal deposition are then lifted off with adhesive tape, and the adhesive properties of the exposed film are passivated by immersing the substrate in acetic anhydride, which acetylates the free amine groups in the film, lowers the surface energy and reduces the number of sites available for hydrogen bonding, thereby reducing surface adhesion in those areas not covered by metal (Fig. 3.1(c)). Finally, the metal mask is etched away, and other structures, proteins or compounds can be adsorbed onto the substrate. (Fig.3.1(d)). A very high contrast is

seen between unmodified areas (where particles adhere strongly) and passivated areas (where virtually no particle adhesion is observed).

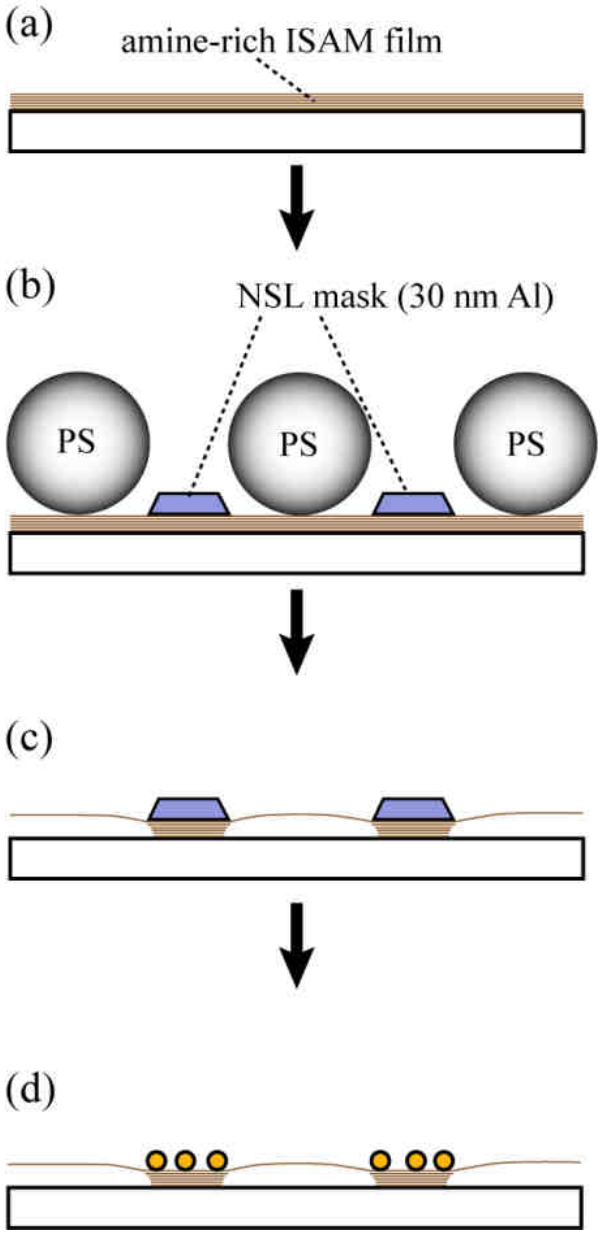

Figure 3.1 (Al) mask is deposited on the ISAM film with nanosphere lithography. (c) The adhesion to the surface is passivated with acetic anhydride. The mask remains securely attached. (d) The mask is removed with wet-etching, and nanostructures can be preferentially adhered to the exposed areas.

This type of adhesion layer is particularly useful in plasmonic applications as it does not degrade the plasmonic properties of surface-bound metal structures. An example of such applications includes colloidal gold plasmonic sensors,[80-83] which can be used to detect the presence of an analyte that shifts the plasmon resonance of the particles when it binds to them. Another example is surface enhanced Raman spectroscopy (SERS),[84-87] which makes it possible to measure the Raman spectrum of minute quantities of a molecule, even as small as a single molecule.[86, 87] Both these techniques rely on strong plasmon resonances, which means that conventional gold and silver on adhesion layers, made from metals such as Cr, Ni or Ti are not useful, as they tend to strongly degrade the plasmon resonances.[88, 89] As ISAM films are entirely dielectric, they do not share this disadvantage.

Another advantage of my approach is that it makes self-aligning adhesion lithography possible. Specifically, one can adsorb one type of nanoparticle on the surface and then passivate the adhesion to the film, taking the process through the stage shown in Fig. 3.1(c). The particles will remain securely attached, since the film below them is masked from the passivation. However, particles and compounds introduced later will not bind to the passivated areas of the surface, which makes it possible to modify and add to the bound nanostructures[90] without having to take additional precautions to avoid non-specific binding elsewhere on the surface.

ISAM films are a form of LbL films made by alternately applying positively and negatively charged polyelectrolytes to a surface. The particular type of ISAM film of interest to me has a large surplus of amine groups, the availability of which on the surface can be controlled by pH. These films were pioneered by Rubner *et al.*,[43, 44, 91] and can be made from a variety of polymers; I use the polycation poly(allylamine hydrochloride) (PAH) and the polyanion poly(styrene sulfonate) (PSS). An ISAM film can be made from these polymers by immersing a

negatively charged substrate in a solution of PAH, which assembles into a thin layer on the surface while reversing the surface charge. After rinsing to remove excess polymer, the substrate is immersed in a solution of PSS, which assembles onto the PAH, restoring the negative surface charge. This process can be repeated as many times as needed, building up films of arbitrary thickness on the surface. If the assembly is performed at pH values above 8, the amine groups in the PAH will only be partially protonated, increasing the amount of PAH adsorbed on the substrate in each step. This results in a film with a large excess of amines, where most amine groups are free rather than coordinated with sulfonate groups, as is the case for films assembled at neutral pH. The uncoordinated amines make the film strongly adhesive to a wide variety of materials and molecules, including gold nanoparticles and small proteins, which I have used here to evaluate the adhesive properties of the film. It is also easy to couple a variety of organic molecules and peptides to the amines,[75] so the surface properties of the film are easily modified.

Amine-rich ISAM films have the remarkable property that they can undergo dramatic reversible swelling and deswelling as a function of pH.[43, 44] Lowering ambient pH to ~ 3 causes the film to swell, gaining up to several hundred percent in thickness. The film can be returned to its original thickness, if the pH is raised as high as 10. This hysteresis is due to coiling of amine groups into tightly packed hydrophobic domains at high pH. The pK_a of the amines in this state is quite low (~4),[44] so that strongly acidic conditions are required to protonate the amines. In the resulting swelled film, the pK_a of the amines is close to its value in solution (~ 8.8), so deprotonation requires the pH to be raised above this value. The hysteresis makes it possible to regulate the quantity of amines available at the surface near neutral pH, and should therefore make it possible to adjust the degree of adhesion to the film. However, I find that adhesion is quite strong even when adsorbing onto a deswelled film, thus this possibility is not investigated

further here. Perhaps more interestingly, the ability to adjust film thickness means I can adjust the effective index of refraction seen by the particles as well as the separation between the nanostructure and the substrate, which provides a way to tune plasmon resonances after surface fixation.

3.2 Materials and Methods

Pre-cleaned glass slides, acetic anhydride, sodium hydroxide, and hydrochloric acid were purchased from Fisher Scientific. Poly (allylamine hydrochloride) (PAH) M_W = 15,000, and Poly (sodium 4-styrene-sulfonate) (PSS) M_W = 1,000,000, sodium citrate, gold (III) chloride trihydrate, and other chemicals were obtained from Sigma Aldrich. EZ-Link NHS-$(PEG)_4$-biotin, high sensitivity NeutrAvidin-HRP, 1-Step Slow TMB (a solution of 3,3',5,5'-tetramethylbenzidine with H_2O_2), Blocker BSA in PBS(10X), and StartingBlock (PBS) Blocking Buffer were obtained from Thermo Scientific. GoldSeal UltraStick APTES terminated slides were purchased from Electron Microscopy Sciences. 99.999% gold and 99.99% Aluminum for evaporation were purchased from International Advanced Materials and Kurt J. Lesker, respectively. The ISAM films were deposited on standard pre-cleaned 1"x 3" microscope slides, which were first cleaned by the RCA process,[67] *i.e.* immersion in a 1:4:20 solution of NH_4OH:H_2O_2:H_2O at 80±5 °C for 15 min, followed by a 1:1:5 solution of HCl:H_2O_2:H_2O at 80 ± 5 °C for an additional 15 min. Between and after the immersion steps, the slides were rinsed with copious amounts of DI water and then stored in DI water until used.

3.2.1 ISAM deposition and passivation

ISAM films were deposited on the RCA cleaned slides. The deposition was done by consecutively dipping each slide in aqueous solutions of PAH (adjusted with NaOH to pH 9.45)

and PSS (pH 9.45) for 45s. The concentration of the polyelectrolyte solutions were 10 mM on a monomer basis. The slides were rinsed in DI water (pH 9.45) between insertion in each polyelectrolyte solution. The pH of the solutions and rinse water were adjusted and monitored to not deviate within more than ±0.02 pH units during the deposition process. Between 1 and 10 bilayers of PAH/PSS were deposited and capped with a final layer of PAH. Such a film containing *n* bilayers plus a PAH layer will be denoted $(PSS/PAH)_n/PAH$. The glass slides coated with ISAM films were then soaked for 10 min in DI water adjusted with HCl to pH 3.25 followed immediately by a 20 min soak in DI water adjusted with NaOH to pH 10.25. Finally, the substrates were rinsed with DI water (pH ~5.5) and used immediately.Surface amines were passivated by acetylation with acetic anhydride. The substrates were first dried in a convection oven at 115 °C, and then immersed in neat acetic anhydride (97%+, Acros Organic) for 20 minutes, and finally rinsed thoroughly with DI water.

3.2.2 Nanosphere lithography

A close-packed monolayer of polystyrene nanospheres was formed on the substrates from their suspension using convective self-assembly. The details of my method have been described elsewhere,[92] and largely follow the processes of Dimitrov and Nagayama[29] and Prevo and Velev.[1] Briefly, it involves placing a suspension of nanospheres at the inside corner of the space formed by the substrate surface and an angled plate suspended just above it. As the substrate is withdrawn from below the plate at the correct speed, a monolayer colloidal crystal of close-packed polystyrene spheres forms at the receding contact line between the suspension droplet and the substrate. In most cases, I used positively charged amidine functionalized spheres, as the substrate surfaces were positively charged, and the technique requires that substrate and spheres have the same charge so that premature binding to the surface does not occur. 40 nm of gold or

30 nm of aluminum was then deposited onto the slides using electron beam evaporation. Most of the metal is blocked by the spheres, reaching the surface only through the triangular-shaped gaps between the spheres, after which the spheres were removed with adhesive tape, leaving behind an array of triangular particles.

3.2.3 Gold nanosphere synthesis and adsorption

Negatively charged, citrate-terminated gold nanoparticles were synthesized with the Turkevitch method.[93] This is the oldest and simplest method for making gold nanoparticles, and yields spheroidal particles with a fairly uniform size distribution. Briefly, 15 mg of $HAuCl_4 \cdot 3H_2O$ was dissolved in 150 ml of DI water and brought to a vigorous boil. 2.25 ml of a 10 mg/ml aqueous solution of sodium tricitrate was then added as quickly as possible. The reaction was allowed to proceed for at least 5 minutes, and the resulting nanoparticle suspension was removed from the heat. After synthesis, the particles were cleaned three times with centrifugation and resuspension in DI water, which resulted in a ς-potential of approximately -40 mV at a pH of about 5. The average diameter is largely determined by the ratio of citrate to gold salt. In my case, the average nanoparticle diameter is approximated 25 nm.

The negative charge of the gold nanospheres should cause them to adhere strongly to the positively-charged ISAM surfaces, so surface absorption of these particles was used as a simple test of the adhesive properties of the ISAM films and other substrates. This was done by simply immersing substrates in the nanosphere suspension for 3 hours, after which the substrate was thoroughly rinsed with water and dried before imaging with scanning electron microscopy.

3.2.4 Surface biotinylation and protein adsorption assay

In addition to adhesion of gold nanoparticles, I also carried out preliminary tests of the ISAM films' functionalization and protein binding characteristics. Those assays are described schematically in Fig 3.2. Biotinylation was first carried out by coupling the crosslinker NHS-$(PEG)_4$-biotin to the surface, which only works in locations where free amines are available, *i.e.* not in passivated areas of the film (Fig. 3.2(b)). A conjugate of the proteins NeutrAvidin (NA) and horseradish peroxidase (HRP) was then introduced. The NA binds with great specificity to the biotin linkers (Fig 3.2(c)), and may also bind nonspecifically to the film in the absence of any biotin. The amount of HRP on the film was quantified by allowing it to interact with tetramethylbenzidine (TMB) in the presence of hydrogen peroxide (purchased as a premixed "Slow-TMB" solution), which causes the TMB to be catalytically converted to a colored form (cTMB) which stays in solution and can be detected with absorption spectroscopy.

In detail, the procedure was performed as follows: The substrate, a microscope slide coated with the film under test, was inserted into a demountable multiwell microarray from ArrayIt Corporation. Two mg of NHS-$(PEG)_4$-biotin was dissolved in 1.7 mL of dry DMF and added to the appropriate wells of the microarray. The reaction was allowed to proceed for 1 hour, and the substrate was then removed from the microarray cassette and freely rinsed with DMF. The substrate was placed in a beaker filled with DMF and stirred for 15 minutes, after which the DMF was replaced and stirred for an additional 15 minutes. Finally, the substrate was rinsed with ethanol followed by deionized water.

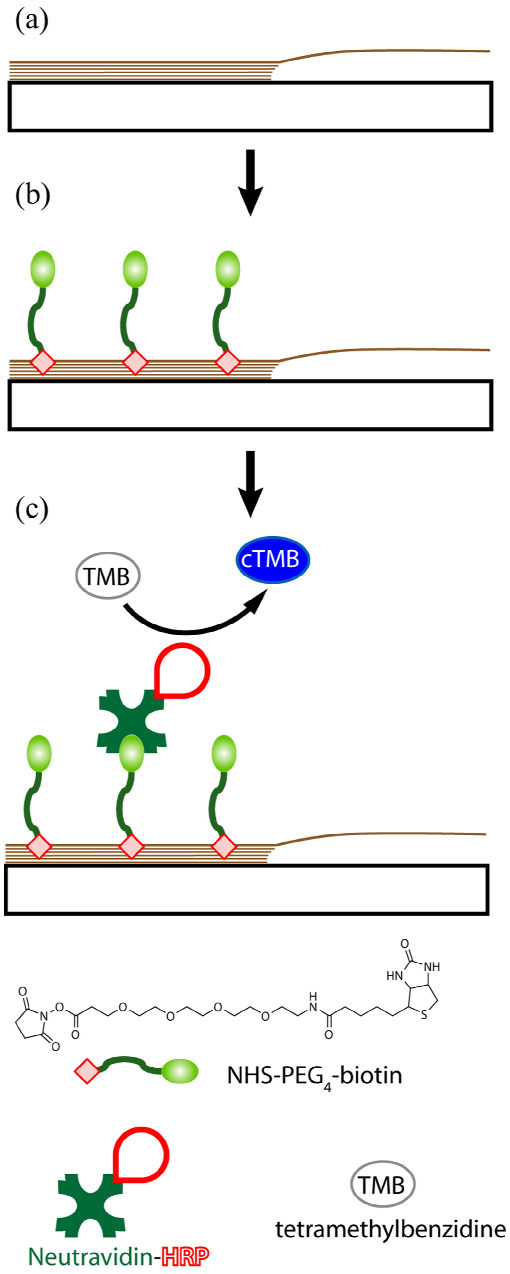

Figure 3.2 Schematic of the protein adsorption assay. (a) An amine rich ISAM film (which may or may not be patterned) or other substrate with exposed amine groups is first fabricated. (b) The cross-linker NHS-PEG_4-biotin is exposed to the surface, binding to the available amine groups. (c) The surface is exposed to the neutravidin-HRP protein conjugate. The quantity of protein bound to the surface can be determined by monitoring the transformation of colorless TMB into a colored version (cTMB) by enzymatic action by the HRP in the presence of H_2O_2. Protein adsorbed directly on the film will give a similar signal, so the amount of non-specific binding can also be estimated with this assay.

The substrate was coated with StartingBlock, a proprietary protein solution intended to suppress non-specific protein binding, and allowed to dry in ambient conditions for 30 minutes. Next, the

substrate was inserted into the Array-It cassette, where additional StartingBlock was added and removed from the microwells two times. A protein mixture containing 13.6 μg NA-HRP, 150 μL 10% BSA in PBS, and 1.35 mL PBS was prepared, and 150 μl was added to each well and allowed to interact for 1 hour. To completely remove excess NeutrAvidin, the substrate was removed from the cassette and rinsed with PBS. This was followed by a second PBS rinse (containing 0.05% Tween-20) that was carried out in an identical manner as the DMF rinse described above. As a final step to minimize non-specific binding of protein, the substrate was left in a 1 M NaCl solution overnight at 4 °C. The substrate was then thoroughly rinsed with PBS and dried with dry N_2 gas. Next, 100 μL of Slow-TMB substrate was added to each microwell, and allowed to interact. The ensuing HRP-TMB reaction was quenched by adding 100 μL of 1 M sulfuric acid (H_2SO_4) to each well after 10 minutes had passed. 175 μL of this solution was then mixed with the same quantity of DI water. The optical absorbance at 452 nm was measured and used as an indication of the amount of HRP present in each well.

3.3 Results and Discussion

3.3.1 Nanosphere lithography on ISAM and APTES substrates

Nanosphere lithography (NSL)[14] is one of the simplest ways to fabricate nanostructures on a surface. It results in arrays of triangular nanoparticles over large areas, as much as several cm^2. The particles have very sharp corners, which makes them particularly suitable for plasmonic applications such as surface enhanced Raman spectroscopy.[84] The quality of the NSL is highly dependent on surface properties, and can in fact only be performed if there is no significant adhesion between the surface and the polystyrene nanospheres as they assemble into a

colloidal crystal. To minimize the surface adhesion, I use positively charged amidine-terminated nanospheres, and ensure that the ISAM film is in its deswelled state.

Fig. 3.3(a-d) show optical micrographs of polystyrene colloidal crystals assembled with convective self-assembly on amine-rich ISAM films of varying thickness. Each white disk corresponds to a nanosphere, and defects appear as dark spots and lines. For comparison purposes, I also deposited colloidal crystals on an APTES substrate (Fig 3.3(e)) and directly on glass (Fig 3.3(f)). Since glass is negatively charged in neutral aqueous solutions, negatively charged carboxyl-terminated nanospheres were used in that case. All crystals were fabricated on the same day, and at the same ambient temperature and humidity. The crystal defect density can therefore serve as a rough indicator of the propensity of the surface to bind the polystyrene nanoparticles during the deposition process.

The colloidal crystal quality is unquestionably the highest on the glass substrate. Only a few vacancies are seen and the vast majority of defects are line defects that occur due to imperfections in the sphere packing. On the amine terminated surfaces there are numerous vacancies, indicating a much greater propensity for the particles to stick to the surface. In spite of this, the quality of the crystal is sufficient for my purposes, as metal deposition onto the crystals will result in a majority of triangular particles in all cases. In the ISAM films, the defect density increases with increasing film thickness, likely due to greater roughness in the thicker films. The defect density seen in the 2-bilayer sample is roughly equivalent to what is seen in the APTES sample. However, the APTES sample suffers from a lack of uniformity, which means that a

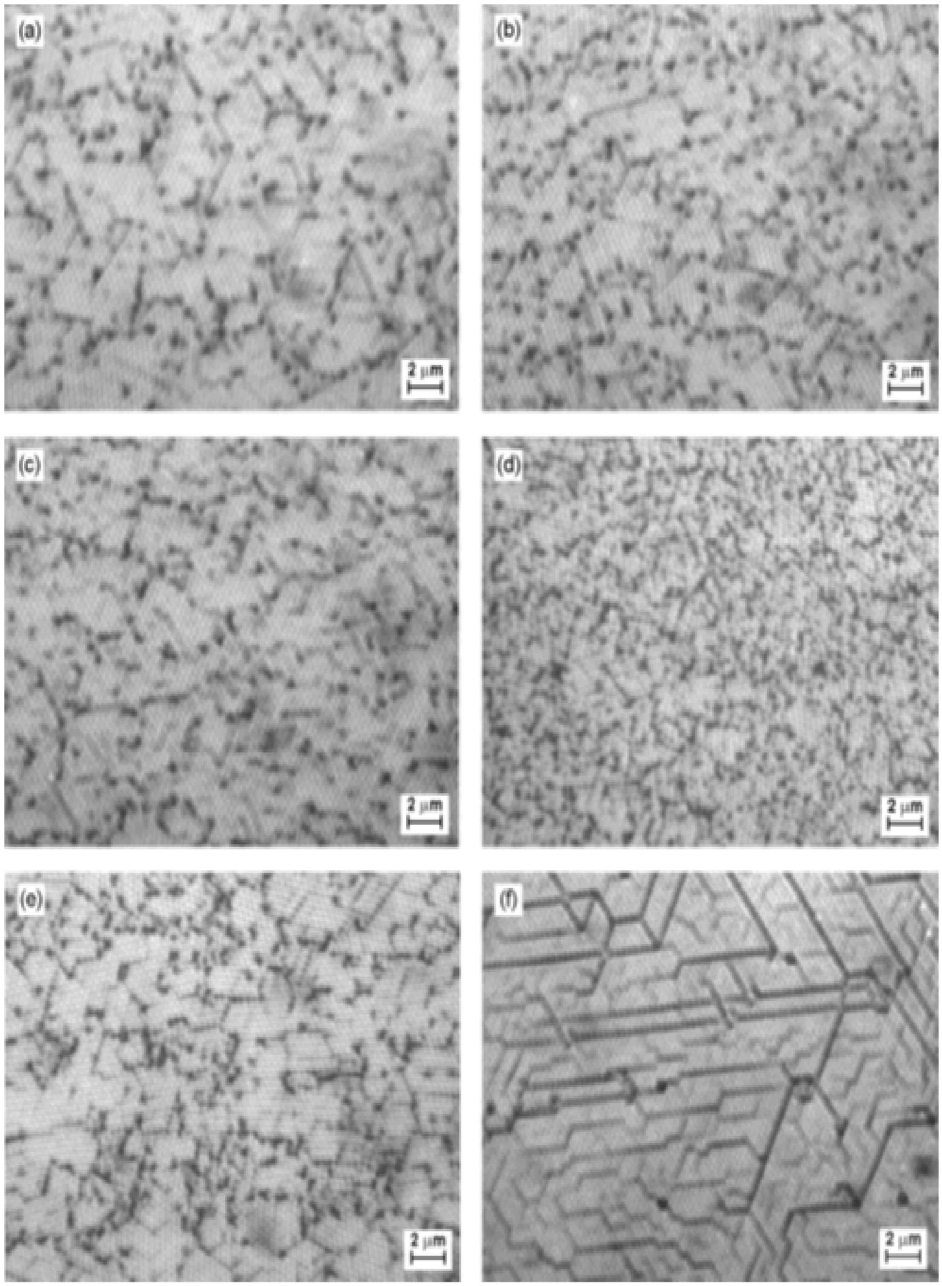

Figure 3.3 Micrographs of colloidal crystals of polystyrene nanospheres deposited with nanosphere lithography, illustrating the dependence of colloidal crystal domain size on the substrate. The spheres are visible as small white disks arranged in a hexagonal close-packed pattern. Defects and missing spheres in the colloidal crystal show up as dark lines and spots. (a) PAH/PSS/PAH film deposited at pH 9.5. (b) $(PAH/PSS)_2$/PAH film. (c) $(PAH/PSS)_5$/PAH film. (d) $(PAH/PSS)_{10}$/PAH film. (e) APTES-terminated substrate. (f) Unadorned glass. Positively charged amidine-terminated spheres were used in samples (a-e), and negatively charged carboxyl- terminated spheres were used in sample (f). Both types of particles were 450 nm in diameter.

monolayer colloidal crystal only forms over some fraction of the surface, while it is straightforward to deposit such a layer over the entire ISAM film substrate.

3.3.2 Adhesion patterning with a metallic mask

When gold nanotriangles are deposited directly on glass with NSL, the adhesion is insufficient to keep them in place even when exposed to a fairly mild disturbance. For instance, adsorbing a monolayer of dodecanethiol onto the particles will lift them off the surface, as is seen in Fig. 3.4(a). If the substrate is coated with an amine-rich ISAM film before the NSL, the particles are fixed in place, and will not lift off after thiol treatment or brief ultrasonication. At this point, the surface between the nanoparticles remains highly adhesive, and readily adsorbs gold nanospheres, as is shown in Fig. 3.4(b). However, the adsorption of gold spheres can be prevented by first passivating the surface with acetic anhydride. The areas of the film already covered by triangular particles is not affected by this, so the triangular particles remain strongly attached to the film, even though the acetic anhydride has almost completely suppressed adsorption of gold nanospheres onto the areas between the particles, as can be seen in Fig 3.4(c). Uncoordinated amine groups extend throughout the full thickness of the ISAM films, and they are rearranged in each swell/deswell cycle, producing a new surface configuration each time.[44] This lends a great deal of robustness to the adhesive properties of the films, which are left unchanged even by significant processing. As a result, it is possible to pattern the surface adhesion with relatively simple means. I first deposited triangular aluminum nanoparticles on an amine-rich ISAM film using nanosphere lithography. The surface was then passivated with acetic anhydride, and rinsed thoroughly. The aluminum was etched away by immersing the substrate in a 1 mM (pH 3.0), 45 °C solution of HCl for 45 min, and then exposing it to pH 10.25

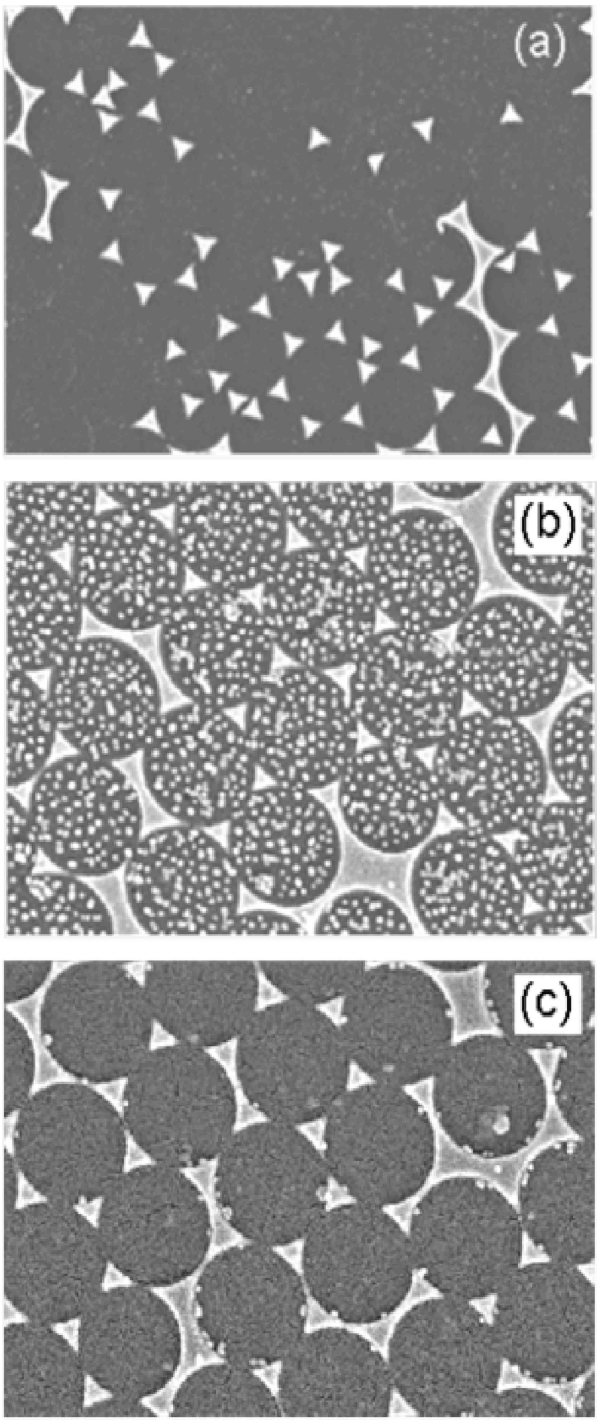

Figure 3.4 SEM micrographs of gold nanotriangles deposited with nanosphere lithography on different substrates; (a) directly on glass, showing poor adhesion after deposition of dodecanethiol; (b) on an amine-rich PSS/PAH film, with gold nanospheres adsorbed in a second step; and (c) on an ISAM film which was then treated with acetic anhydride and onto which gold nanospheres were then adsorbed.

for 20 minutes. Combined with the etch step, this takes the film through a swell/deswell cycle, rejuvenating the surface. The substrate was then immersed in a suspension of gold nanospheres for 3 hours. Figs.3.5 (a-c) show electronic micrographs of gold nanospheres adsorbed on substrates at different pH. While all three substrates readily adsorb the nanoparticles on the amine active areas of the surface, it is easy to observe that the density of the nanospehre coverage varies with pH of the ISAM film. For the pH=7.5 ISAM film substrate, patches of no coverage within the amine rich area were observed. The pH= 8.5 ISAM film follows similar trend, only the uncovered areas within the amine rich regions were smaller and less pronounced. Finally the pH= 9.5 ISAM film substrate shows very uniform nanosphere coverage. The amount of uncoordinated amines in the ISAM film at lower pH values (7.5, 8.5) is less than that in pH=9.5 ISAM film. This leads to inhomogeneous distribution of those amines trough out the film, and therefore nonuniform coverage of the surface with nanospheres. This result is a manifestation of the fact that the amines in the ISAM film reshuffle during swell and deswell cycles to expose fresh amines on the surface of the film. ISAM film deposited at pH lower than 9 does not have enough amines to provide uniform surface density after each swell/deswell cycle.

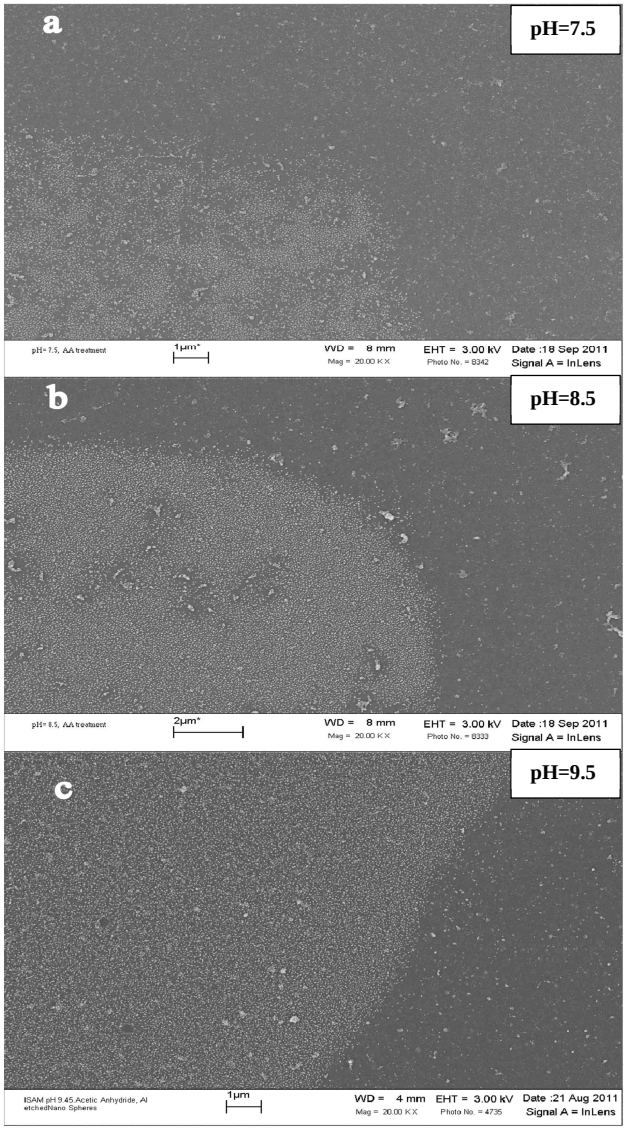

Figure 3.5 SEM micrographs of gold nanosheres adsorbed on ISAM film deposited at different pH conditions. a) Gold nanospheres adsorbed on a substrate coated with pH=7.5 ISAM film b) gold nanospheres adsorbed on a substrate coated with pH=8.5 ISAM film c) gold nanospheres adsorbed on a substrate coated with pH=9.5 ISAM film.

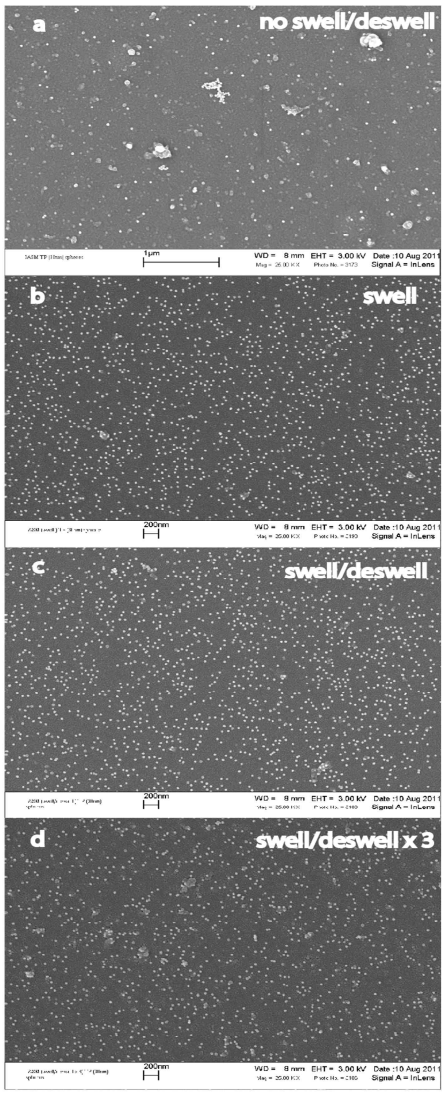

Figure 3.6 SEM images of PAH/PSS ISAM film under various pH conditions. a) no pH change. b) The film was swelled at pH=3.5. c) The film was swelled/deswelled at pH=3.5/10.25. d) The film was subjected to a swell/deswell cycle three times.

Fig 3.6 (a-d) demonstrates the effect of amine rejuvenation on the surface of the ISAM film with cycling of the pH conditions. The ISAM film was made from 10 bilayers of PAH/PSS, which rendered the surface charge negative. Initially the substrate was not subjected to any change of pH (Fig 3.6 (a)), but it was soaked in gold nanaosphere suspension. The nanospheres

have the same charge as the surface of the film and as a result few spheres attach to it due to nonspecific binding. The second substrate (Fig 3.6 (b)) was swelled at pH=3.5 and then soaked in the Au nanosphere suspension. As a result of the amine protonation there were available amines for the nanospheres to attach as seen on the image. The third substrate was swelled and then deswelled , before being soaked in Au nanosphere suspention. As a result the surface of the film is covered with nanospheres. Finally the last substrate was swelled and deswelled 3 times before being soaked in Au nanosphere solution. All three substrates that underwent any change of pH conditions adsorbed the gold nanospheres, but the substrate that was not subjected to pH change. This result clearly indicates the rejuvenation of amines in the ISAM film upon pH cycling.

Furthermore, this patterning technique can be used to modify the surface stickiness on a much smaller scale. I deposited triangular aluminum nanoparticles on an amine-rich ISAM film using nanosphere lithography. Then following the sample preparation procedure described above, I adsorbed gold nanospheres on the patterned surface.

Electron micrographs of the substrate before and after this treatment are shown in Fig. 3.6, where nanospheres adsorb densely on the surface (Fig 3.6(b)) that was protected by the triangular particles, with very little adsorption onto areas that have seen direct exposure to acetic anhydride. The spatial resolution of this process is demonstrably better than 200 nm.

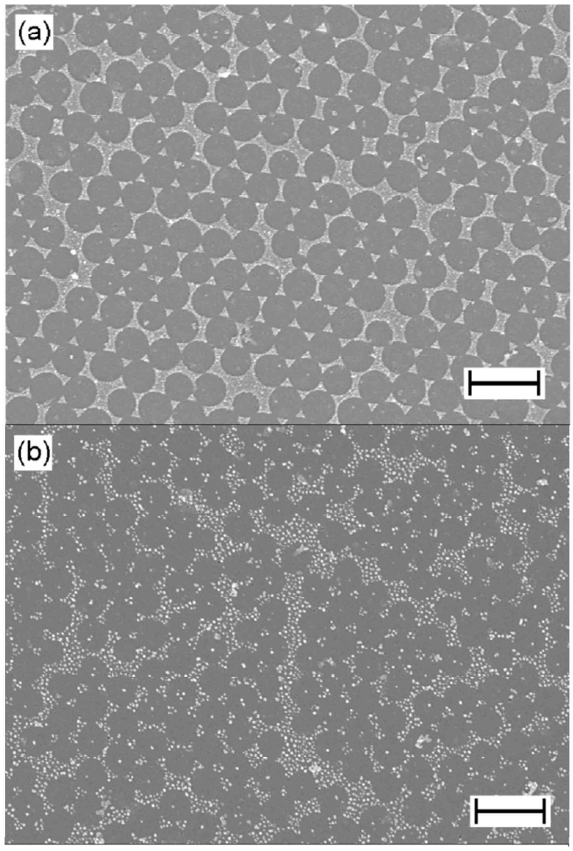

Figure 3.7 (a) Micrograph of an ISAM film with Al nanoparticles applied using nanosphere lithography. (b) The same film after passivation with acetic anhydride, wet etch removal of Al particles and adsorption of gold nanoparticles. The scale bar is 1 µm.

The process just described allows patterning the adhesiveness of the surface into arbitrary or arranged patterns, after which particles, proteins or small molecules are adsorbed onto the surface as desired. Since this is the last step, no constraints are placed on the adsorbate other than the ability to bind to the surface of the film, and particles and molecules that are incompatible with the lithographic process can thus be deposited in a simple manner.

3.3.3 Protein binding and functionalization – comparison between ISAM and APTES substrates

The binding of proteins and small molecules to the surface is of critical interest in nanoassembly. Avidin and its isoforms streptavidin and neutravidin are of particular interest since their highly specific affinity for biotin makes them well suited for the role of linkers in nanoassembly. Protein adhesion is also a key issue in many life science fields, creating additional impetus to study this issue. Here, I present the results of adsorbing a conjugate of neutravidin (NA) and horseradish peroxidase (HRP) onto unpatterned amine-rich ISAM films. It is known that enzymes often retain much of their activity even when embedded within an ISAM film,[94, 95] so the detected HRP activity is likely a good indicator of the amount of protein adsorbed onto the film. Moreover, the isoelectric point of NA is 6.3, while more than 70% of the HRP in my protein conjugate is isoenzyme C, with pI = 8.8. This means that NA has a net negative charge in the pH 7.4 PBS buffer where the adsorption was performed, while most of the HRP has a net positive charge. It is therefore likely that the NA end of the NA-HRP adsorbs preferentially onto the positively charged film, leaving the HRP oriented for maximum activity. In addition, I tested the ability to effectively biotinylate the films by exposing them to a NHS-PEG_4-biotin crosslinker prior to introduction of the NA-HRP conjugate. The NHS group will bind to free amines in the film and the resulting biotinylation should significantly enhance binding of NA-HRP. Fig. 3.7(a) plots the measured HRP activity in ISAM films where the surface was passivated in different ways, including by exposure to acetic anhydride. After passivation, the films were biotinylated as described in the previous section, and then exposed to NA-HRP. The height of each bar in the figure corresponds to the measured HRP activity in the sample, and in my

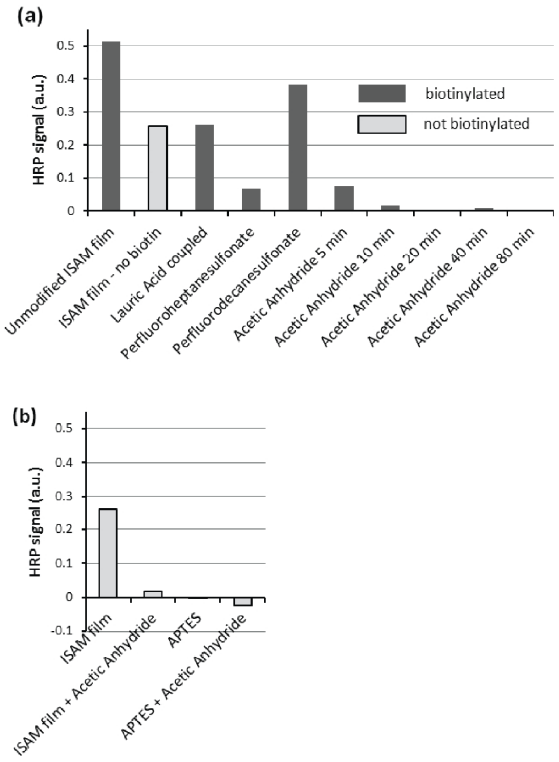

Figure 3.8 Peroxidase activity from NeutrAvidin-HRP conjugate as measured with reaction with TMB. (a) RP signal from films that have been adhesion-passivated in various ways. The dark bars indicate films that were exposed to a biotin-containing crosslinker prior to the protein conjugate. (b) HRP signal from ISAM coated and APTES terminated substrates where NeutrAvidin-HRP was absorbed without any prior biotinylation, with and without passivation with acetic anhydride.

process, this signal is proportional to HRP concentration at least up to values of about 0.3, after which saturation begins to set in. The leftmost two bars in Fig. 3.8(a) are control measurements and correspond to unpassivated ISAM films, with and without biotinylation. A significant HRP signal is present even without biotinylation, indicating that there is significant non-specific binding of the protein to the film. However, exposure to the biotin crosslinker at least doubles the HRP signal, demonstrating that the ISAM film can be successfully biotinylated.

I attempted to suppress the binding in several ways. Lauric acid was coupled to the film with 1-Ethyl-3-(3-dimethylaminopropyl)carbodiimide (EDC), creating covalent bonds between the acid and free amine groups in the film. The film was exposed to two different perfluorinated surfactants, which are standard anti-adhesion agents.[96] These methods did suppress binding to some degree, but satisfactory results were only obtained by treating the film with neat acetic anhydride for at least 20 minutes. The very small signal after this treatment indicates successful suppression of NHS coupling to amine groups in the film, as well as suppression of non-specific binding of both the protein and the crosslinker molecule.

A standard way to immobilize metal nanostructures is to adsorb them onto a monolayer of thiol- or amine-terminated silanes such as aminopropyltriethoxysilane (APTES)[81] or mercaptopropyltrimethoxysilane (MPTMS)[97, 98] that is applied to a glass or silicon substrate. APTES functionalized surfaces are also used heavily in many life science applications, and it is therefore of interest to compare the adhesion properties of the amine-rich ISAM films to substrates functionalized with APTES. Fig. 3.9 compares adsorption of gold nanospheres on a 10-bilayer ISAM film with an APTES substrate. As expected, the particles adsorb readily on both substrates (Fig 3.9(a,c)). When the surfaces are passivated with acetic anhydride, this

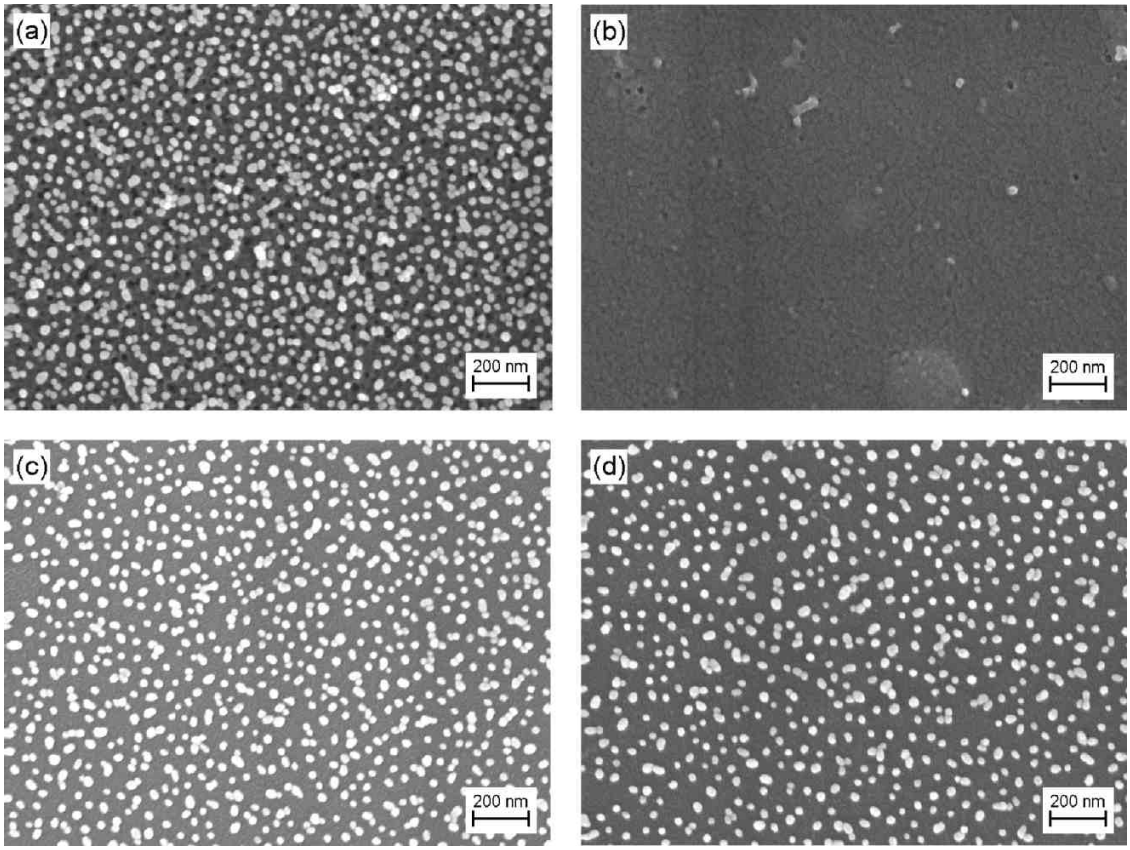

Figure 3.9 SEM micrographs of citrate terminated gold nanospheres adsorbed onto various substrates. (a) Untreated amine-rich PSS/PAH ISAM films (10 bilayers). (b) Acetic anhydride passivated ISAM film. (c) Untreated APTES-terminated substrate. (d) Acetic anhydride treated APTES substrate.

suppresses particle adsorption completely only in the ISAM film (Fig. 3.9(b)), while on the APTES substrate passivation is successful in some areas but ineffective in others. No ultrasonication was performed before any of the images in Fig. 3.9 were taken, but brief (~ 30 s) sonication had no discernible effect on the quantity of gold particles present on the film. Fig. 3.8(b) compares the non-specific binding of NA-HRP in ISAM films to that in APTES substrates. Only the untreated ISAM film shows any significant non-specific protein binding in my assay, while HRP activity in the acetic anhydride treated ISAM film and in the APTES film, whether treated with anhydride or not, are all very small, deviating from zero by less than the

experimental uncertainty. The negative value in the right-most bar reflects drift in the spectrometer during the measurement.

3.3.4 Effects of pH

The dynamic nature of the conformation of the ISAM films, crucial to the adhesion patterning described in this dissertation, is illustrated by the quartz crystal microbalance (QCM) measurements shown in Fig 3.10. The QCM is capable of measuring changes in areal mass density of a film with precision in the ng/cm^2 range. In each of the studies cases, the pH was allowed to equilibrate at a starting pH of 3.25. The pH was then changed to 7.0, 10.25, 7.0, and finally back to 3.25. This cycles the film through its full swell/deswell cycle. Figs. 3.10(a) and 3.10(b) both plot the results from as-prepared amine-rich (PAH/PSS)$_{10}$/PAH films, with the distinction that in Fig. 3.10(a), the films were exposed to DI water where the pH had been adjusted by minimal addition of HCl or NaOH, whereas in Fig 3.10(b), the films were exposed to buffered solutions (standard 10 mM solutions of citrate buffer, phosphate buffered saline, and carbonate buffer for pH 3.25, 7.0 and 10.25 respectively). In both cases, the expected swelling (deswelling) is observed at low (high) pH as a change in the areal density of the film. The expected hysteresis is observed at pH 7, but the hysteresis is smaller if the film is exposed to buffers rather than pH adjusted DI water. This suggests that the degree of swelling in the film and thereby the degree of amine protonation and adhesiveness can be tuned continuously by both the pH history and the ionic strength of the solution in which it is immersed.

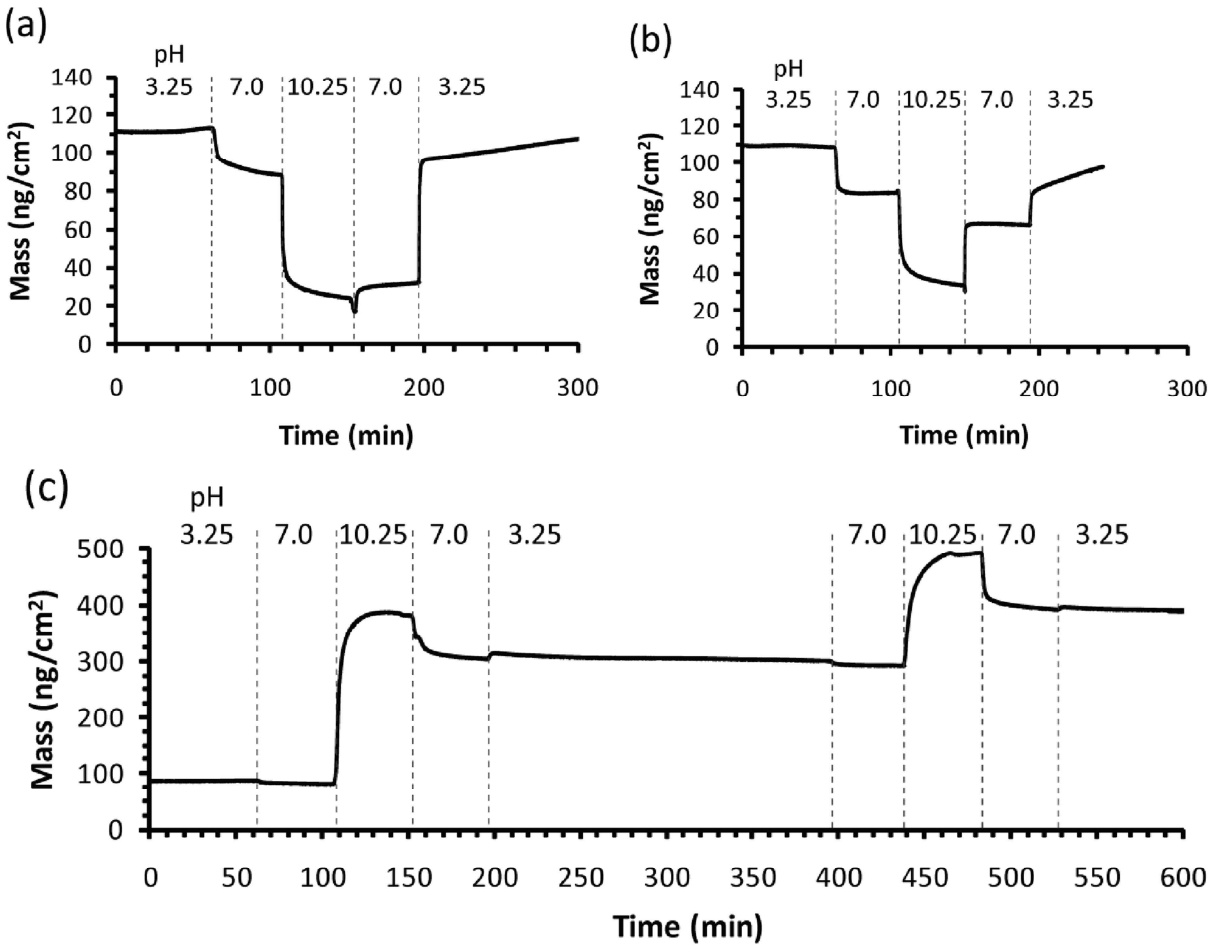

Figure 3.10 Areal mass density changes in 10-bilayer PSS/PAH films assembled at pH 9.45 as a function pH as measured by quartz crystal microbalance. (a) Unmodified ISAM film, minimal ionic strength in the immersions. (b) Unmodified ISAM film, 10 mM buffer solutions. (c) Acetic anhydride passivated ISAM film, high ionic strength (10 mM buffers). The unmodified film shows the expected hysteresis versus pH, while the passivated film displays irreversible swelling at high pH values.

The effect of the same sequence of pH values on an acetic anhydride treated ISAM film is plotted in Fig. 3.10(c). In this case, low pH values do not affect the film appreciably, but exposure to high pH causes the film to swell. A likely explanation for this is that only a small number of unreacted amines remain in the film, and when a large fraction of these are deprotonated, much of the electrostatic attraction that holds the film together is removed,

allowing water to infiltrate it. Some of this water remains in the film when the pH is returned to neutral or lower pH, so the swelling is partially irreversible.

3.4 Conclusion

I have shown that amine-rich PSS/PAH ISAM films are an excellent choice for surface adhesion of metal nanostructures and at least some proteins. These films are at least as good as the more commonly used APTES terminated surface, displaying higher surface uniformity and, in at least some cases, better adhesion. Fabrication of the films is straightforward, and does not involve any toxic chemicals, and a film with highly uniform properties is obtained without extreme efforts.

Nanosphere lithography, relying on convective self-assembly of polystyrene nanospheres to form a template for metal evaporation, can readily be performed on the ISAM films. This results in a large number of triangular nanoparticles, even if the colloidal crystal template has a significantly higher defect density compared to what is seen in convective self-assembly on plain glass.

The surface adhesion can be passivated with acetic anhydride without affecting the binding of structures already bound to the surface. This is particularly useful since it may allow nanoassembly to be performed on a surface without encountering unwanted non-specific surface binding. Arbitrary pattern of adhesiveness can be readily fabricated by taking advantage of this property, protecting areas where adhesiveness is to be retained with an evaporated aluminum mask that is removable with chemical wet etching

This can be used to direct assembly of nanostructures to particular areas, which is of great importance when bottom-up fabricated nanostructures are to be integrated into larger devices or

systems. On the life science side, similar requirements arise in areas such as tissue engineering, and the fact that no post-processing is required after the adhesion step is particularly useful when working with living cells or other structures that cannot withstand the processing conditions of standard lithography.

I hypothesize that the ability to pattern the adhesiveness of these films with a rather harsh lithographic process arises from the dynamical nature of their conformation. The adhesion comes from uncoordinated amine groups which exist at all levels or the film, and which mostly are protected in coiled-up hydrophobic domains. Cycling the pH reorganizes the film, exposing virgin amine groups on the surface and removing damage caused by the metal evaporation and subsequent etch.

.

CHAPTER 4 Surface enhanced Raman spectroscopy for patchy modification of the surface functionalization of metal nanoparticles

4.1 Introduction

The success of nanoscience and technology lays in successfully combining top-down and bottom-up nanofabrication techniques. Lithography methods combined with nanoparticle fabrication and manipulation to build nanoscale complex structures will make it possible to take full advantage of the optical, mechanical, and chemical properties of the nanoparticles. For example bioconjugate techniques realized through the use of photosensitive bifunctional crosslinkers, and selective two photon functionalization can be used to manufacture nanoparticle molecules.[99, 100] Zhang et al.,[101] showed in a computer simulation that nanoparticles with patterened discrete interaction sites, can form nanoparticle assemblies. Janus particles[102] are example of nanoparticle assembly by patchy surface modification.

This chapter discusses the creation of a class of patchy nanoparticles where the surface is patterned with discrete interaction sites that that can attract complimentary sites on other particles. The discrete interaction is achieved by functionalization with photo-sensitive biofunctional crosslinker molecules, and their site specific modification by optical means. On one end the crosslinker molecule has a binding group, which easily attaches to the nanoparticle surface. On the other end, the crosslinker has a pthotocleavable capping group, which after photoactivation leaves the molecule, thus exposing a bonding group available to couple with the

appropriate chemistry. I chose to work with amine groups as functional groups to bind nanoparticles to, because they can anchor metal nanoparticles, and are easy to further modify.

Our approach for patchy photoactivation is based on the plasmonic properties of metal nanoparticles. The plasmonic properties of metal nanoparticles were discussed in detail in Chapter 1. In short incident light of resonant wavelength will excite plasmon resonances in metal nanoparticles. The incident light is concentrated into nanometer size regions of very high light intensity known as "hot spots" located on sharp corners or narrow gaps on the nanoparticle. The enhancement factor is ~10^{4-7}, which allows to detect signal from molecules adsorbed on the surface of the nanoparticles.

Direct manipulation of objects on the size scale of nanoparticles in suspension is quite difficult because they are prone to aggregation during manipulation, and are difficult to purify without large loss of particles. On the other hand, surface fixated nanoparticles can't aggregate and can be cleaned effectively by simple rinsing. Therefore, my efforts were focused on patchy modification of surface fixated gold nanoparticles, and in particular triangular nanoparticles. The geometry of the nanoparticles is a result of the fabrication method. I used nanosphere lithography, because it yields large arrays of particles, with low polydispersity, for which the plasmons can be tuned to most wavelengths in the visible and near IR ranges by changing the size of the triangular nanoparticles. Additionally, that geometry is known to exhibit large plasmonic enhancement factors[103].

In my work, I used several different molecules to functionalize the gold nanotrangular particles. Gold has strong affinity to thiols, therefore the molecules I chose to use for the functionalization have thiol groups on one end. Benzyl mercaptan (Fig 4.1 (a)) was used as a test

molecule to ensure that the triangular nanoparticles were constructed with the size and thickness necessary to achieve plasmonic resonance close to the wavelength of the laser used for exciting the surface plasmons. 4-fluorobezodithoic acid (4-FBTA) (Fig 4.1 (b)) was used to as a test

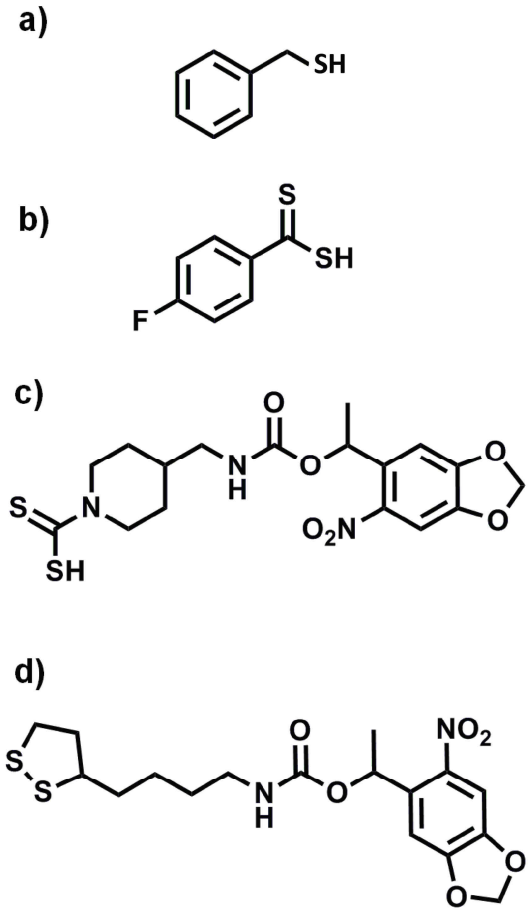

Figure 4.1 Schematic of molecules used to functionalize gold nanoparticlces a)Benzyl mercaptan, b) 4-FBTA, c) P3- DTC, d) LIP3

molecule to ascertain the ability of the anchoring dithiol group to adsorb and adhere strongly on the gold surface. For the photoactivation process, I used two different kinds of photoactivatable molecules Fig 4.1(c,d), namely 4-((((1-(6-nitrobenzo[d][1,3]dioxol-5-yl)ethoxy)carbonyl)amino)methyl)piperidine-1-carbodithioic acid (P3-DTC), and 1-(6-

nitrobenzo[d][1,3]dioxol-5-yl)ethyl (4-(1,2-dithiolan-3-yl)butyl)carbamate (LIP3). Each P3-DTC molecule has dithiocarbamate (DTC) group that bonds to gold. This is the strongest bond available for our purposes because the nitrogen atom in the six-membered ring exchanges an electron with a gold atom from the surface. The drawback of using P3-DTC is that it oxidizes and degrades rather quickly to become unusable within about 4 hours after synthesis. LIP3 has a disulfide group that when in contact with gold breaks down to two thiols that bond to the gold, this is a strong bond but not as strong as DTC bond. The weakest bond is the single thiol bond, which is a feature of Benzyl mercatan. The disulfide group of LIP3 is much more stable than DTC, and is less prone to oxidation; LIP3 is stable for months because of the properties of its anchor group. Both LIP3 and P3-DTC have the same photocleavable group.

4.2 Materials and Methods

Pre-cleaned glass slides were purchased from Fisher Scientific. Poly (allylamine hydrochloride) (PAH) M_W = 15,000, and Poly (sodium 4-styrene-sulfonate) (PSS) M_W = 1,000,000, and other chemicals were obtained from Sigma Aldrich. 99.999% gold for evaporation was purchased from International Advanced Materials. The ISAM films were deposited on standard pre-cleaned 1"x 3" microscope slides, which were first cleaned by the RCA process,[67] *i.e.* by immersion in a 1:4:20 solution of NH_4OH:H_2O_2:H_2O at 80±5 °C for 15 min, followed by a 1:1:5 solution of HCl:H_2O_2:H_2O at 80 ± 5 °C for an additional 15 min. Between and after the immersion steps, the slides were rinsed with copious amounts of DI water and then stored in DI water until used. Nanospehere lithography was performed with amidine functionalized, polystyrene spheres 480nm in diameter purchased from Invitrogen. Photoactive molecules were synthesized by Brandon Thorpe from Webster Santos's group from the

Chemistry department at Virginia Tech. Precursors for the syntheses were obtained from Sigma Aldritch, and Fischer Scientific. Surface enhanced Raman spectroscopy was carried out with WITEC Alpha-500 raman spectrometer.

4.2.1 ISAM deposition

1 bi-layer of PAH/PSS ISAM films with a top layer of PAH was deposited on the RCA cleaned slides, following the procedure described in Chapter3

4.2.2 Nanosphere lithography

A close-packed monolayer of polystyrene nanospheres was formed, on an ISAM film coated substrate, following the procedure described in Chapter 2. I used positively charged amidine functionalized spheres, as the substrate surfaces were positively charged, and the technique requires that substrate and spheres have the same charge so that premature binding to the surface does not occur. 55 nm of gold was then deposited onto the slides using electron beam evaporation. Most of the metal is blocked, reaching the surface only through the triangular-shaped gaps between the spheres, after which the spheres were removed with adhesive tape leaving behind an array of triangular particles.

The lithographic process is illustrated in Fig.4.2. First, an amine-rich ISAM film is deposited on the charged substrate. Because nanosphere lithography[14] is one of the easiest ways to create nanoscale patterning on a surface, I used amidine functionalized polystyrene spheres to deposit a monocrystal on the film. The nanospheres served as an evaporation mask for metal deposition, and are subsequently lifted off with adhesive tape.

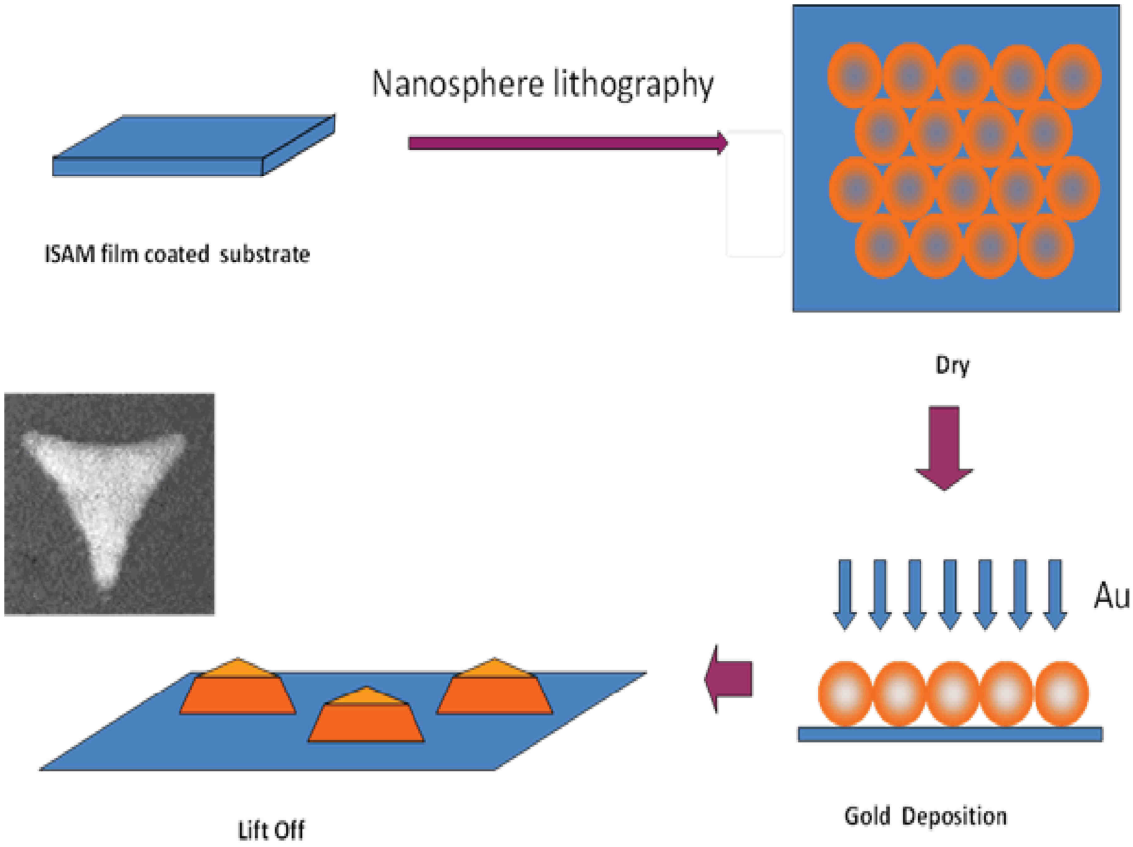

Figure 4. 2. Schematic of a sample preparation process. ISAM film is deposited on a glass substrate. Nanosphere lithography followed by gold evaporation and lift off of the polysterene nanospheres leads to deposition of ordered gold nanotriangular structures on the substrate surface.

Fig. 4.3 shows an array of gold nanotriangular particles deposited on the ISAM film coated substrate surface after the nanosphere evaporation mask was lifted off. The triangular particles are formed by evaporated metal that is deposited on the substrate surface through the open areas between the closely packed nanospheres. It is important that the gold nanotriangular particles are strongly adhered to the substrate surface, because when they are exposed to different solutions containing solvents they can easily come off the substrate if not firmly attached to it. The ISAM film used for substrate coating is rich in amine groups which provide numerous adhesion sites for the gold as described in Chapter 3.

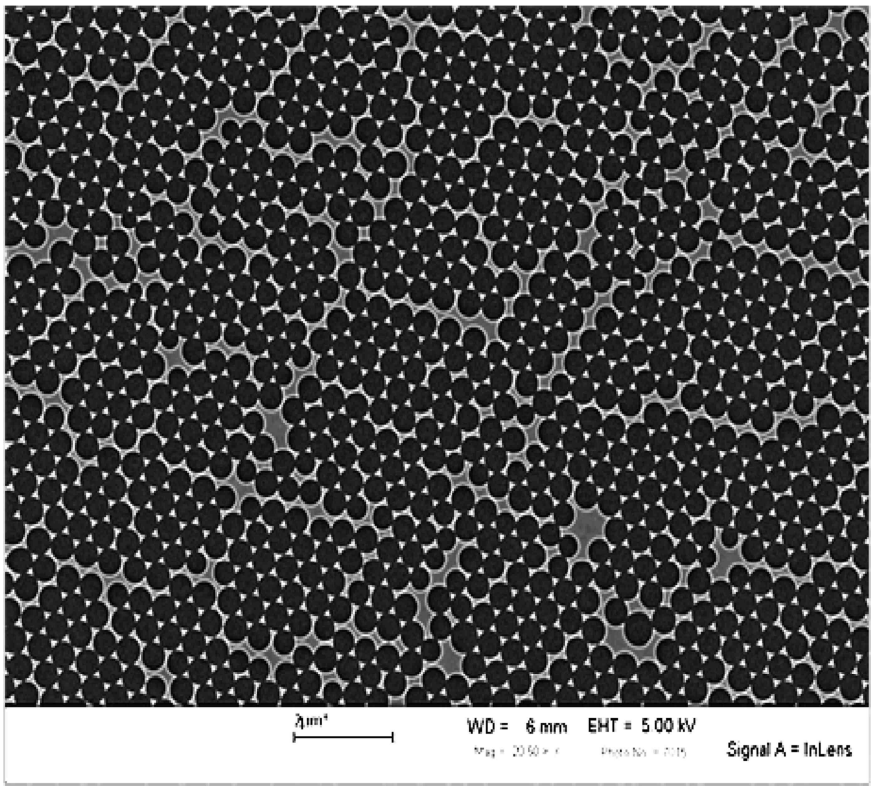

Figure 4. 3. SEM image of Au nanotriangular particles deposited trough a monocrystal microsphere mask by metal evaporation.

4.3 Results and discussion

Due to their small size and composition, the triangular nanoparticles experience surface plasmon resonances when illuminated with light with wavelength that is close to their SPR. The Raman spectrometer at my disposal uses a monochromatic laser with a wavelength of 785nm, therefore my gold triangular nanoparticles were made to have plasmonic resonance close to that

wavelength. The absorption wavelength of gold triangular nanoparticles depends both on the thickness and the size of the particles. I chose to use 480nm diameter nanospheres for evaporation mask, because it allowed me achieve the correct resonance without using too much gold. Fig. 4.4 shows the absorption spectrum of 55nm gold triangular nanoparticles with absorption maximum at 770 nm.

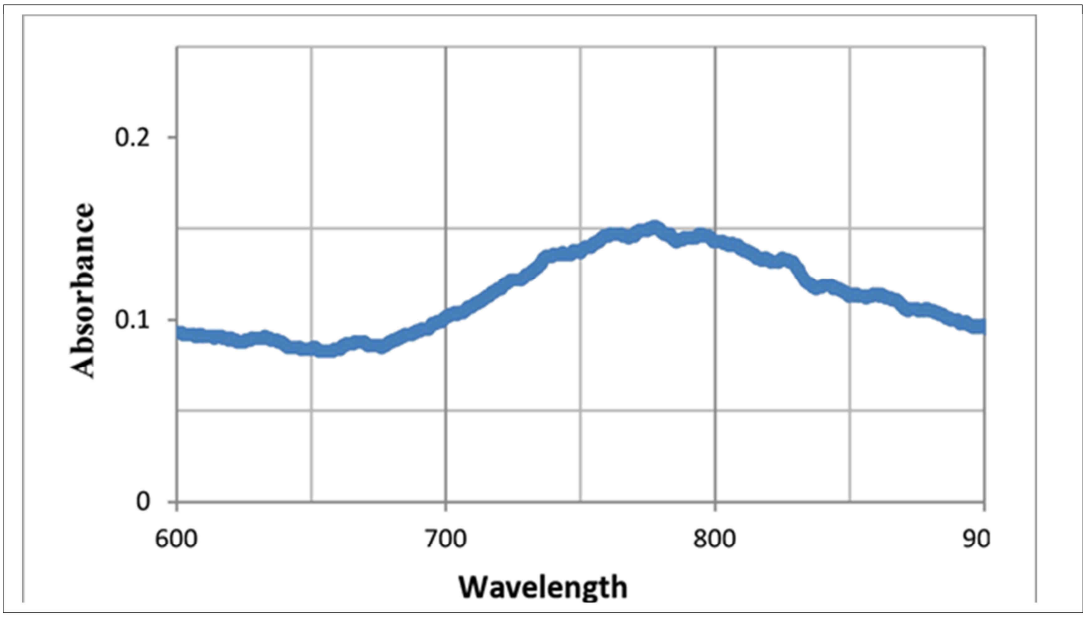

Figure 4.4 Absorbance of 55nm thick gold nanotriangular particles.

The substrates with nanotriangular particles were immersed in 2mM solutions of Benzyl Mercaptan, 4- FBTA, P3-DTC and LIP3, (Fig 4.1(a-d)). Those molecules have affinity to attach to gold, because they contain one or two thiols, and after a 24 hour soak and subsequent rinse, the triangular nanoparticles on the substrate surface are fully functionalized. Benzyl mercaptan and 4-FBTA are used as test molecules to first show that the fabricated arrays of gold triangular nanoparticles are indeed suitable for SERS applications. Those molecules cover the entire surface of the triangular nanoparticles but only the ones that are close to the hot spots of the nanopartielces will contribute to the SERS spectrum. The functionalized samples were illuminated with 785 nm laser and SERS spectrum was taken. Figs. 4.5 (a, b) and 4.6 show

surface enhanced Raman signal of benzyl mercaptan and 4-FBTA functionalized gold triangular nanoparticles. The spectra in Fig 4.5 a) and Fig 4.6 indicate very pronounced Raman peaks that are identified with the aromatic ring in the benzyl mercaptan, and the aromatic ring and the fluorine in the 4-FBTA. Fig 4.5 b) shows for comparison FTIR spectrum of benzyl mercaptan(obtained from Sigma- Aldrich), one can see that some of the peaks, especially around 1000 wavenumbers are at similar positions in each spectrum. The strength of the signal suggests that the size of the triangular nanoparticles was well chosen to produce LSPRs with wavelength close to the wavelength of the laser. The data also shows that the test molecules cover the triangular nanoparticles well, and that the coverage around the hot spots is dense enough to produce strong Raman signal. 4-FBTA was specifically designed with anchoring dithiol group so that it would mimic the anchoring group of P3 DTC compound that I used as one of the photoactivatable molecules.

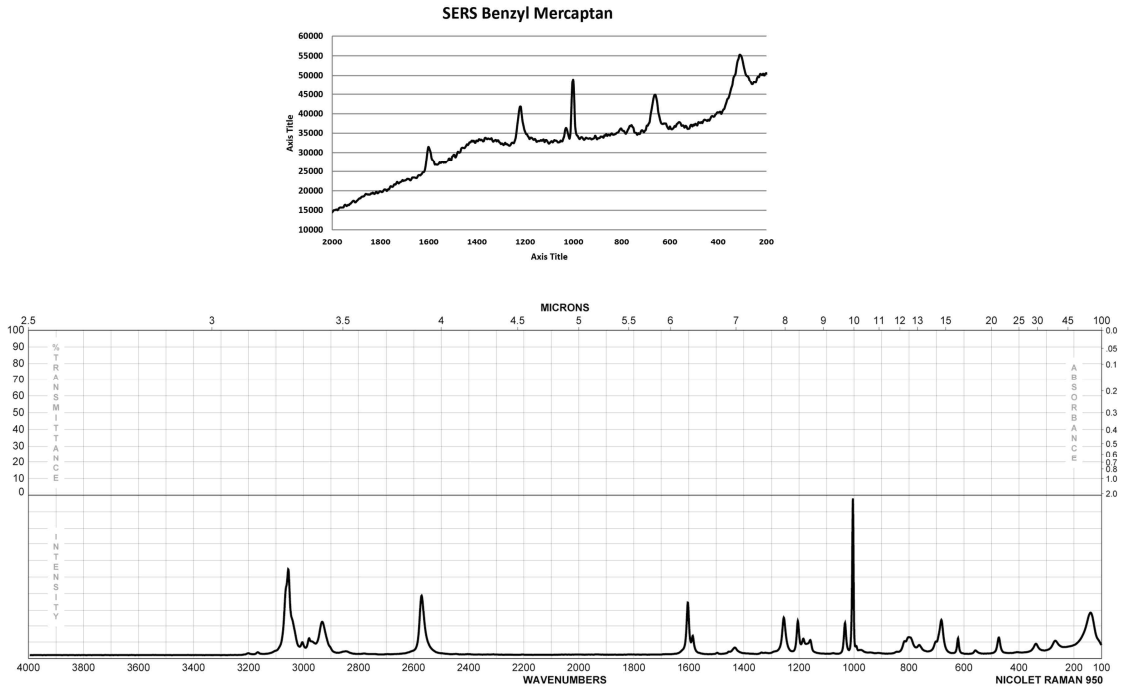

Figure 4.5 (a)SERS of 2mM benzyl mercaptan adsorbed on 55 nm gold nanotriangular particles. (b) FTIR spectrum of Benzyl mercaptan,

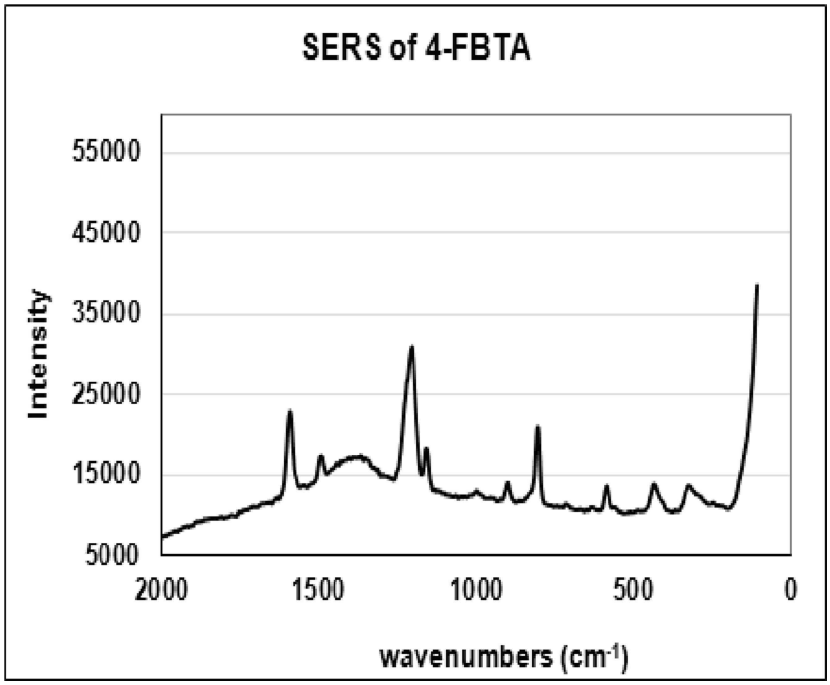

Figure 4.6 SERS of 2mM 4-FBTA adsorbed on 55 nm gold nanotriangular particles.

To characterize the photocleavage efficiency of P3-DTC, I performed a surface photoactivation study on a gold substrate. The photocleavage of P3-DTC with respect to 365nm UV light was closely monitored by reflectance FTIR spectroscopy. This method is used to determine the UV dose needed to complete the photoactivation of P3 DTC on a gold surface. Schematic of the photactivation mechanism is shown in Fig4.7 (a). P3 DTC has two important parts, an anchor group connected to an six-membered ring an N-H group, and a photocelavable cap. A single UV photon or two red photons with enough energy will break the bond between the photocleavable leaving group and the rest of the molecule. IR spectra of P3- DTC as a function of UV exposure with doses from 0 J/cm^2 to 2.3 J/cm^2 are shown in Fig.4.8. As a result of the UV irradiation, a peak emerges at 1050 cm^{-1}, and is associated with a C-N stretch as shown on Fig. 4.7 b). This

vibrational mode indicates that primary amines are being created after photocleavage. Similarly, the extinction of peaks, such as the ones located at 1480 and 1530 cm^{-1}, can aptly represent the photocleavage of P3- DTC. If I plot the area of the absorption peak(s) as a function of the UV dose, I can determine the quantity of light needed to cover the gold surface with primary amine groups. The presented data illuminate the fact that photocleavage of P3-DTC can be done with relatively small dose. The dose is expected to be less for P3-DTC molecules anchored to the gold nanotriangles due to surface plasmon enhancement at the hotspots.

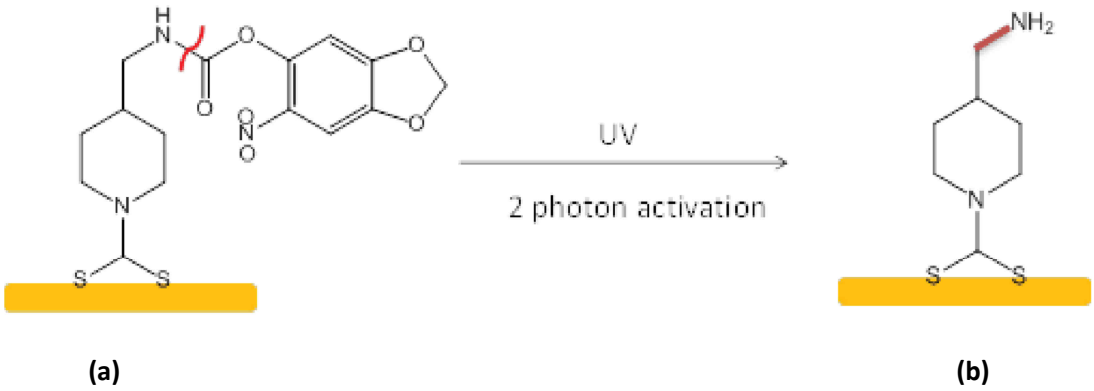

Figure 4.7 Schematic of (a) the mechanism of photoactivation of P3-DTC. (b) C-N stretch of photoactivated P3-DTC molecule adsorbed on gold surface after photoactivation with UV light.

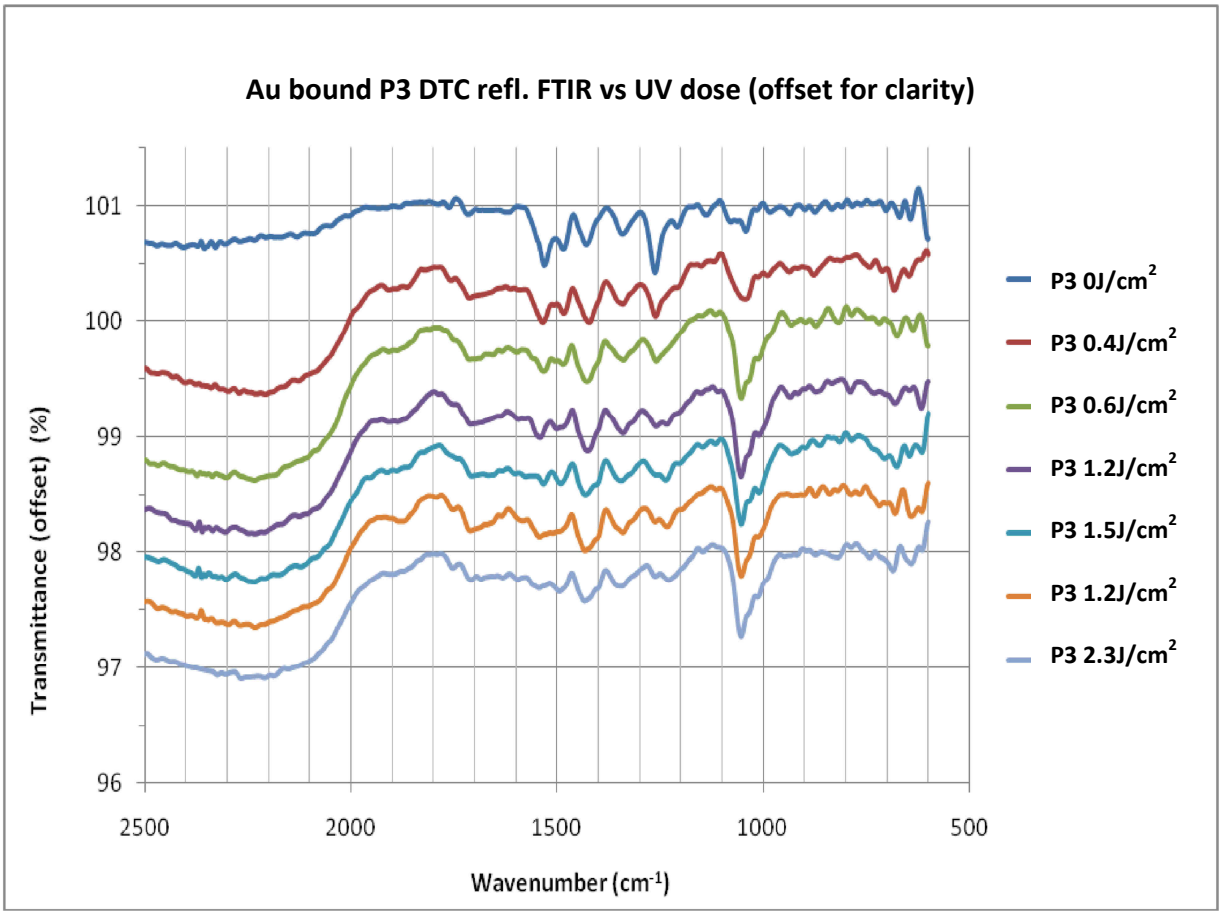

Figure 4.8 Reflectance FTIR spectra of P3 DTC bound to a gold surface as a function of UV exposure at 365 nm. Some peaks (at 1260 cm^{-1}, 1480 cm^{-1} and 1520 cm^{-1}) fade with UV exposure, while one peak (at 1050 cm^{-1}) strengthens considerably. The 1050 cm^{-1} peak is associated with a C-N stretch, and its strengthening with UV exposure signifies cleavage of P3 to reveal a primary amine.

From the data of the surface study of P3-DTC, one can determine the dose needed for full photo activation of all P3-DTC molecules on the gold surface. The result is shown in Fig 4.9, where the sample was irradiated with UV light for various periods of time and FTIR spectrum was taken. From the photoactivation curve, was determined that the dose for full activation of P3-DTC is ~1.5 J/cm^2.

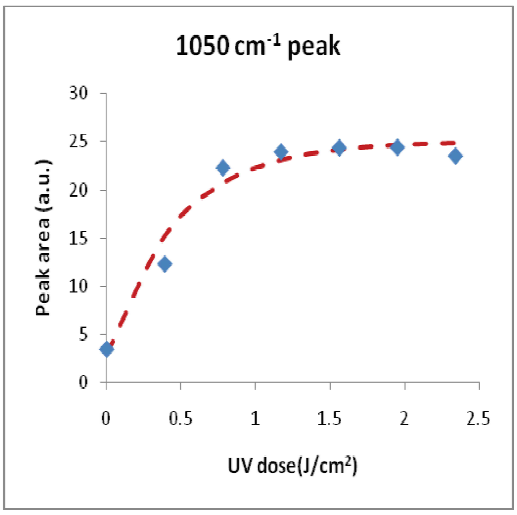

Figure 4. 9 FTIR measurement of activation dose of PD DTC on gold surface. The dose for full photocleavage of P3-DTC is ~1.5J/cm^2, at 365nm UV light.

Fig 4.10 shows the surface enhanced Raman spectrum of 55 nm thick gold nanotriangles functionalized with P3-DTC photoactivatable molecule. Before photoactivation of the molecule, the SERS spectrum should have peaks present, while after photoactivation there will be no peaks in the spectrum, because the part of the molecule left on the surface is too short to register a Raman signal. Fig 4.11 presents SERS spectra of P3-DTC illuminated with various doses of UV, the spectra do not show any peak evolution. The fact that peaks are not evolving in the spectrum, leads to a few possible scenarios of why the molecule does not show any SERS signal.

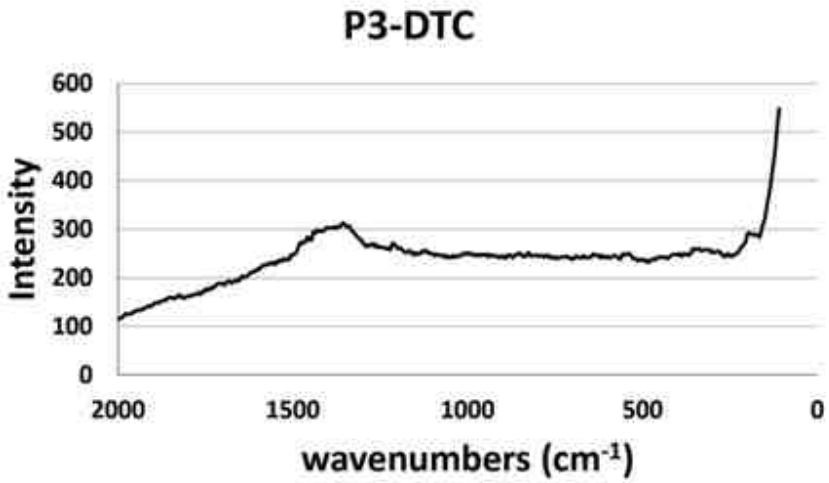

Figure 4.10 SERS of 2mM P3- DTC adsorbed on 55 nm gold triangular nanoparticles.

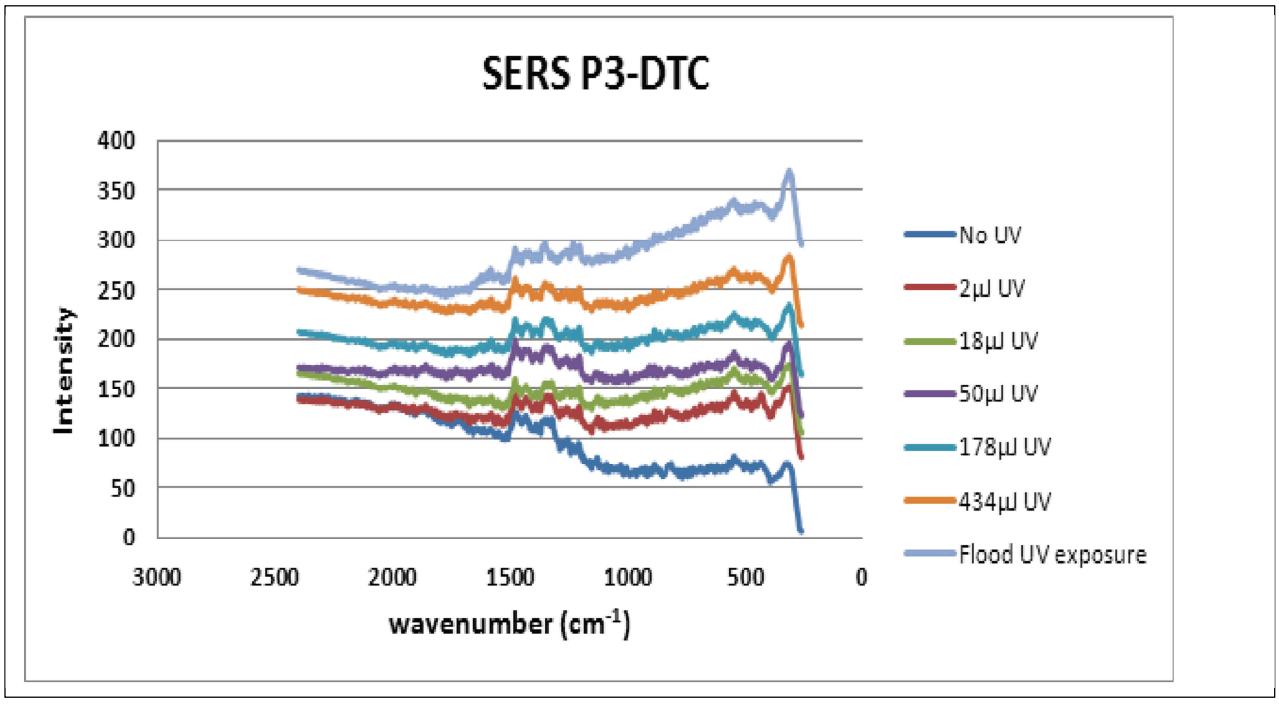

Figure 4.11 SERS of P3-DTC photoactivation with UV dose. Dose is increased and raman spectrum is taken, no change in the signal is observed at any UV exposure dose

My first hypothesis why I could not see any peaks in the P3-DTC Raman signal was that the anchoring group is not efficient enough to allow stable adsorption of P3-DTC on or close to the hot spots without any migration on the surface of the nanoparticles. To test the anchoring mechanism, I used a modified version of the molecule that we denote LIP3 (Fig. 4.4 d)). It differs from P3-DTC in the anchoring group, where instead of DTC the molecule ends with a disulfide group. The disulfide transforms into dithiol when the molecule is in close proximity to gold, which provides good adhesion to gold although the bond is weaker than DTC bond. Unlike DTC, however, LIP3 is less prone to oxidation and hydrolysis.

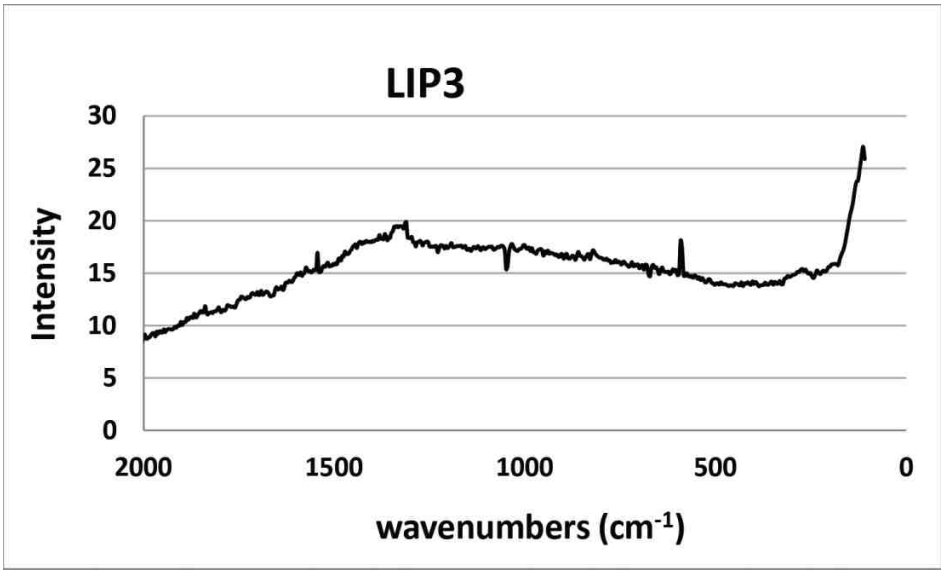

Figure 4.12 SERS spectrum of 2mM LIP3 adsorbed on gold nanotriangles.

Fig. 4.12 shows no significant peaks that can be identified with the molecule at the hot spots of the nanotriangles. In this case again there are a few possibilities for that result, not enough molecules close to the hot spots, premature photoactivation due to lightning rod effect or high curvature catalysis. I will explain those effects in more detail later in the chapter. Given the result, FTIR and XPS spectrum of the LIP3 photoactivation on plain gold surface as a function of

time were taken by Dr. John Morris from Chemistry Department at Virginia Tech. The goal of the measurements was to determine if there is photoactivation of LIP3 on the surface. Also, if there was photoactivation, what was the chemical composition of the surface before and after activation. Fig 4.13 shows the photoactivation process by plotting the change of absorbance with UV dose, which is an indicator of the photo activation. When LIP3 is not photoactivated on the gold surface, the absorbance spectrum contains several peaks, which can be identified from the literature[104]. With increasing the UV dose more and more photocleavable parts of LIP3 will be removed from the surface, which corresponds to decrease of absorbance. Fig 4.13 also displays a differential spectrum, which shows the time evolution of the photoactivation, the increase of the peak size indicates the number of leaving groups diffusing away from the surface. The peak assignment of the differential spectrum is as follows: peak 1 is characteristic for carbonyl, peak 2 is characteristic of methylenedioxy groups, peak 3 is characteristic of nitro goups, peak 4 is characteristic of benzene, and peaks 5 are characteristic of esters. To confirm that indeed the photoactive part of LIP 3 is removed from the surface of the substrate, XPS measurements were performed parallel to the FTIR measurements.

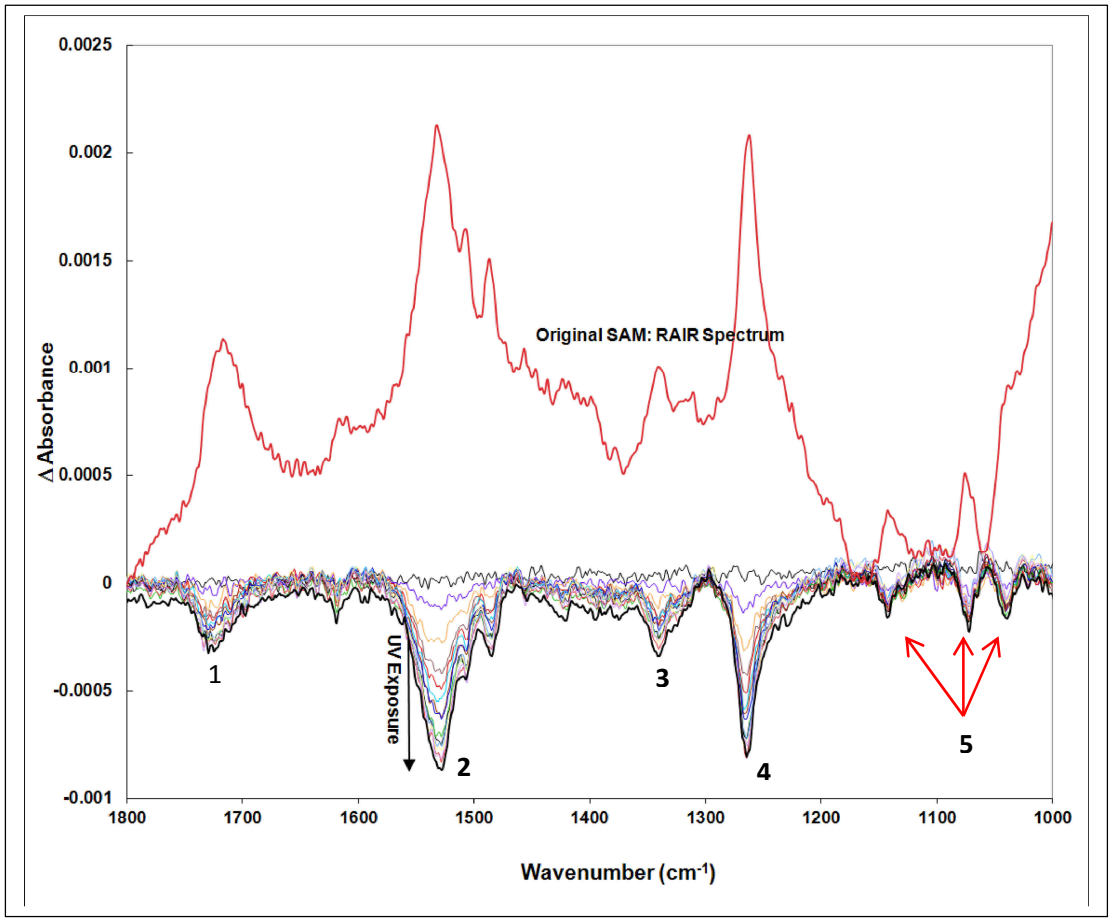

Figure 4.13 FTIR absorbance spectrum of the evolution of photoactivation of LIP3 on plain gold. The absorbance spectra show negative increase of the peaks which corresponds to molecules being separated from the surface.

The results presented in Fig. 4.14(a-d) show that after photoactivation there is a change of the chemical composition on the surface of the sample. Fig, 4.14 (a) shows that the sulfur content does not change which is consistent with the thiols in the molecule anchoring group being bonded to the gold, and not affected by the light exposure. Fig 4.14 (b) shows approximately 50% decrease of carbon content on the sample surface, which is consistent with the photoactive part of the molecule being cleft off from the surface after UV exposure. Fig 4.14 (c) shows no significant change of the nitrogen content on the sample surface, while fig 4.14 (d) shows decrease in the amount of oxygen present on the surface. This is consistent with part of the oxygen leaving the surface along with the rest of the photocleved part of LIP3.

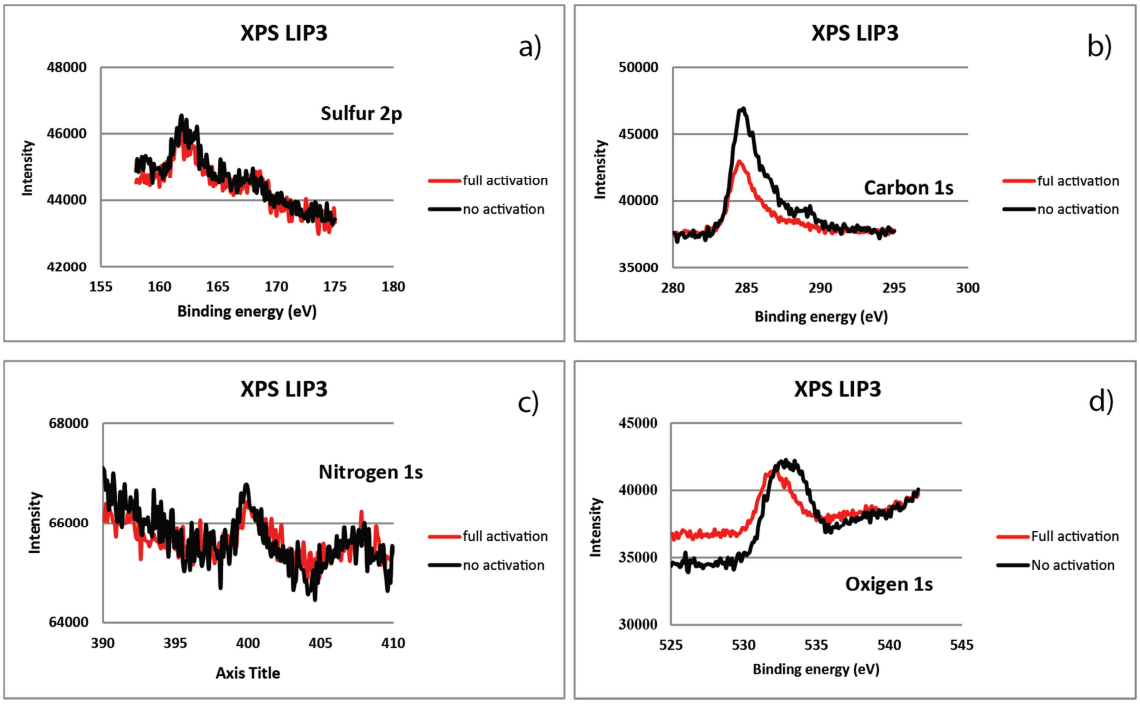

Figure 4.14 XPS spectra of plain gold surface functionalized with LIP3 before and after UV photactivation. a) Sulfur 2p present in the anchoring group of LIP3, b) carbon 1s present in the photocleavable group as well as the rest of LIP3, c) nitrogen 1s present in the amine group left after photoactivation d) oxygen 1s present in the photocleavable group as well as surface oxygen contamination.

The amount of change of oxygen content is not consistent with only departure by photocleaving. Gold surfaces are at least partially oxidized, so even when LIP3 is fully photoactivated, there will be excess oxygen on the substrate surface, which is reflected in the small change of oxygen content before and after activation.

The results from FTIR and XPS measurements indicate several possibilities for the behavior of LIP3 when adsorbed on the gold nanoparticles. First, it is possible that the molecule is too bulky due to the photoactive component and does not cover the hot spot densely enough to observe a meaningful Raman spectrum. Another possibility is that the molecule is prematurely

photoactivated. There are at least a few mechanisms for premature photoactivation; photoactivation due to lightining rod effect, or chemical catalysis.

Apart from plasmon enhancement, the Raman effect can manifest itself through the so called “lightning rod effect”[105]. This enhancement mechanism, which is not related to excitation of surface resonances, occurs when the molecule is adsorbed near high curvature edges of surface irregularities. The polarization of the metal in an external electric field produces a strong local field in the vicinity of such edges which in turn appears as an enhanced Raman scattering by the molecule experiencing this field. The lightning rod effect is manifested in enhancing very weak intensity light incident on the triangular nanoparticles. The enhancement is strong enough to cause photocleavage of the photoactive part of the molecule, even with the precautions we already take to keep the sample in dark or only exposed to long wavelength light.

The second mechanism could be chemical catalysis, which is expressed in interaction of the electron bands of the nanoparticle with the ligand molecule resulting in cleavage of the molecule[106]. Nano-particles of gold lose their metallic nature as their size decreases, the transition occurring at a size dependent on the chemical environment but, corresponding to a hemispherical cluster. The special electronic configuration of very small nanoparticles results from the fact that their physical dimensions are smaller than the characteristic dimension of the electron wave function of the bulk material. This means that it is possible that electrons from the atoms of those particles interact with the functionalizing molecule and cause chemical reaction resulting in cleavage of the photo active cap.

4.4 Conclusion

In this study I used arrays of gold triangular nanoparticles produced with nanosphere lithography method for surface enhanced Raman spectroscopy. The goal of the study was to create patchy modification of the nanoparticle surface by functionalizing the surface with photoactive molecules and using the plasmonic properties of the particles for photo activation at the hot spots thus grating patchy functionalization. I was not able to clearly show true patchy modification of the nanoparticle surface. We have identified several possible reasons for this, which include unstable anchoring at the hot spots of the triangular nanoparticles, bulkiness of the molecule preventing dense population at the hot spot thus rendering weak Raman response, premature photoactivation from lightning rod effect, or chemical catalysis due to the high surface curvature at the hot spots of the triangular nanoparticles.

Future work aimed to resolve this problem will use a specially designed test molecule which will easily show if there is premature photoactivation. Such a molecule, based on LIP3 where adamantine has been added is shown in Fig 4.15.

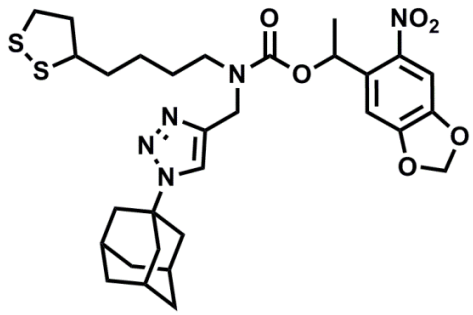

Figure 4.15 Adamantane modified LIP3 molecule to be used for diagnostic of premature photactivation at the hot spots of gold nanotriangular particles

Adamantane has strong double peak near 800 cm^{-1} in its Raman spectrum, so presence or absence in SERS will show if there is photoactivation as well as if the molecule is anchored on the hot spot with good coverage.

Chemical catalysis due to high curvature can be avoided by using other types of nanoparticles such as nanorods. Lightning rod effect can be avoided by developing a stricter procedure for sample handling to eliminate unnecessary ambient light exposure.

CHAPTER 5 Two-photon activated two-photon fluorescence and binding of azidocoumarin 151 in a gelatin matrix

5.1 Introduction

Photoactivatable fluorophores, *i.e.* compounds and other entities that may transform into a fluorescent form on absorption of a photon, have gained in interest in the last few years due to their use in optical superresolution microscopies such as PALM, FPALM and STORM. Photoactivation usually occurs on absorption of one UV photon, but if the light intensity is high enough, it can also be triggered by simultaneous absorption of two photons each carrying half the energy required to excite the molecule. This is a nonlinear process where the efficiency scales with light intensity, which means that it can be limited almost completely to the volume immediately surrounding the focus of a converging light beam. properties of a number of different photoactivatable fluorescent compounds have been investigated.

In this dissertation, I apply the same technique to create arbitrary patterns of fluorescence in a gelatin gel where azidocoumarin 151 has been incorporated. Photoactivation causes the dye to bind to the protein matrix while simultaneously becoming fluorescent, creating a static patternof fluorescence. Most of the other reaction products are rapidly removed from the illuminated spot by diffusion, and therefore play no further role in the experiment. Visualization of the fluorescence is also accomplished through two-photon absorption, which makes it possible to carry out both photoactivation and fluorescence monitoring locally at any point in the gel. It is then possible to immediately visualize the written pattern, without waiting for a development step. I note that coumarins can be used as photo initiators of polymerization[107-110], so this approach may also be of direct interest to the field of two-photon fabrication.

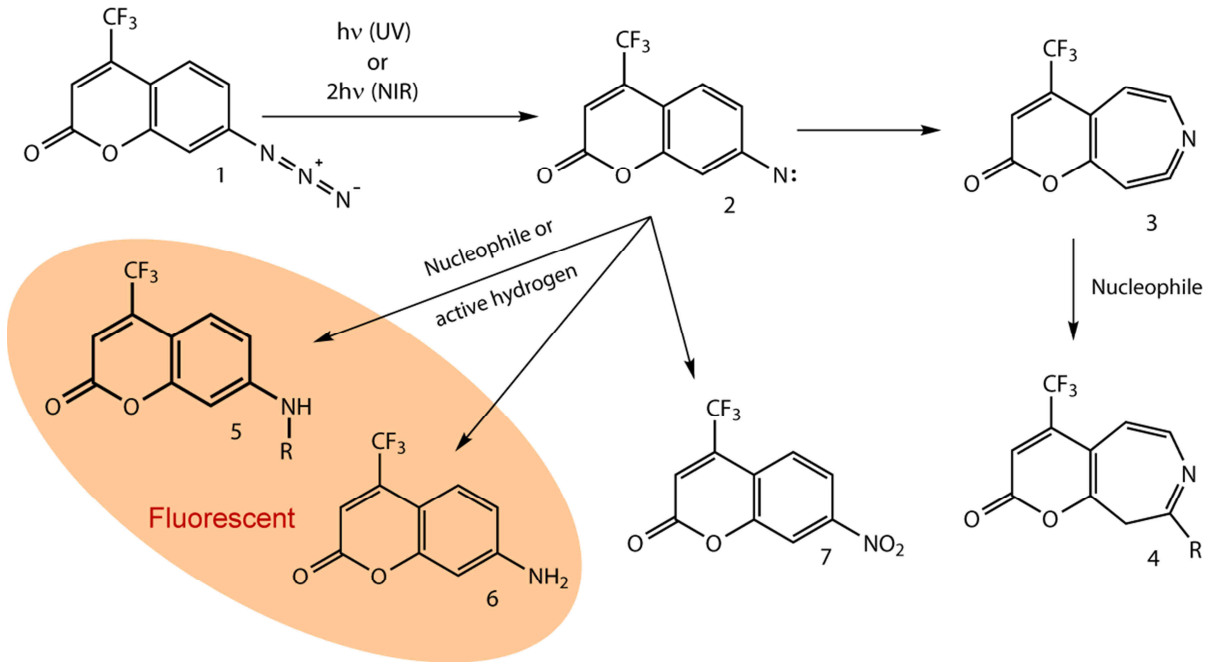

Figure 5. 1 Some possible reaction pathways for photoactivation of azidocoumarin 151 1. The fluorescent product 5 is crosslinked with the gelatin matrix and is responsible for the fluorescent signal we observe.

Figure 5.1 outlines the reaction paths for **1** (Azidocoumarin 151, AzC151). Upon absorption of a UV photon, **1** may expel a nitrogen molecule, forming a highly reactive nitrene **2**. The nitrene can then undergo ring expansion, incorporating the nitrogen atom into a dehydroazepine **3**, which then can react with nucleophiles to form the crosslinked product **4**. The nitrene can also react directly with a number of different groups and form crosslinked products like **5**. The nitrene may also directly abstract hydrogen or oxygen from the environment, reverting back to the original coumarin dye **6** or its nitrosubitituted version **7** [111]. The path to **3** and **4** normally dominates, but it can be suppressed if electron withdrawing moieties are attached to the aryl group [112], stabilizing the intermediate nitrene, so that products **5** and **6** also likely form in significant quantities [113]. This is fortunate for my purposes, as these compounds are strongly

fluorescent, while **3**, **4** and **7** are not. Therefore, virtually all the fluorescence observed by us likely originates from **5**, since the other molecules either are at best weakly fluorescent and/or do not bind to the gelatin.

I have chosen to work with 7-azido-4-trifluoromethyl-1,2-benzopyrone (azidocoumarin 151, AzC151) rather than the better studied AzC120 moiety. This is because the additional fluorine atoms in azidocoumarin 151 redshifts the absorption band, improving the overlap with the wavelength range of our laser. Additionally, as fluorine is an electron withdrawing group, AzC151 theoretically should produce less of **3**, and therefore yield a more fluorescent product.

5.2 Experimental

In the basic experiment showcased in this dissertation, I incorporate AzC151 into a gel made from water, methanol and gelatin, and monitor its behavior as it is activated by a beam of focused light from a femtosecond light source. Fig. 5.2 schematically shows the optical setup. Pulses from a Chameleon Ultra II ultrafast Ti:Sapph laser are focused in an inverted Zeiss LSM 510 confocal microscope into the sample gel. The gel is contained in an airtight container to prevent evaporation of the solvent, and optical access is provided through a thin glass window at the bottom of the container. Any resulting fluorescence is collected by the microscope objective, and separated from the laser light with a beam splitter and an optical long pass filter, before being detected by a photomultiplier tube. The laser outputs 150 fs long pulses at 80 MHz and can be tuned to any wavelength between 690 nm and 1080 nm. The power of the laser was measured before entering the microscope and at the backplane of the microscope objective. These numbers, along the transmittance of the objective provided by the manufacturer, were used to calculate the total optical power delivered to the gel.

The AzC 151 was synthesized from its corresponding coumarin fluorescent dye by following the method of Barral *et al.* [114] Briefly, 100 mg of 7-amino-4-trifluoromethyl-1,2-benzopyrone (coumarin 151, C151) was dissolved in 10 ml of acetonitrile in a round bottom flask. The solution was cooled to 0°C and 110 µl *t*-butyl nitrite followed by 95 µl azidotrimethoxysilane were added dropwise. The reaction was allowed to proceed for two hours in the dark after which it was dried, resulting in approximately 80 mg of a pinkish powder that was used without further purification. All chemicals were obtained from Sigma-Aldrich.

Gelatin gels are normally made from aqueous solutions, but since AzC 151 is poorly soluble in water a 70:30 v/v mixture of water and methanol was used instead. It is known that a gelatin sol/gel system that contains alcohol exhibits phase separation by spinodal decomposition, but by using a sufficiently high fractions of gelatin and water in the gel, this is suppressed as the critical decomposition temperature is pushed below the gel point [115]. In my case, I dissolved 13 mg of AzC 151 in 45 ml of the solvent mixture, and added 7 g of type B gelatin (Sigma-Aldrich). The mixture was heated to about 45 °C and stirred for 20 minutes, and was then allowed to set. The gel was then reheated and sealed inside the airtight container before measurements were performed. If this container is kept in the dark, the optical properties of the gel remain stable for several weeks.

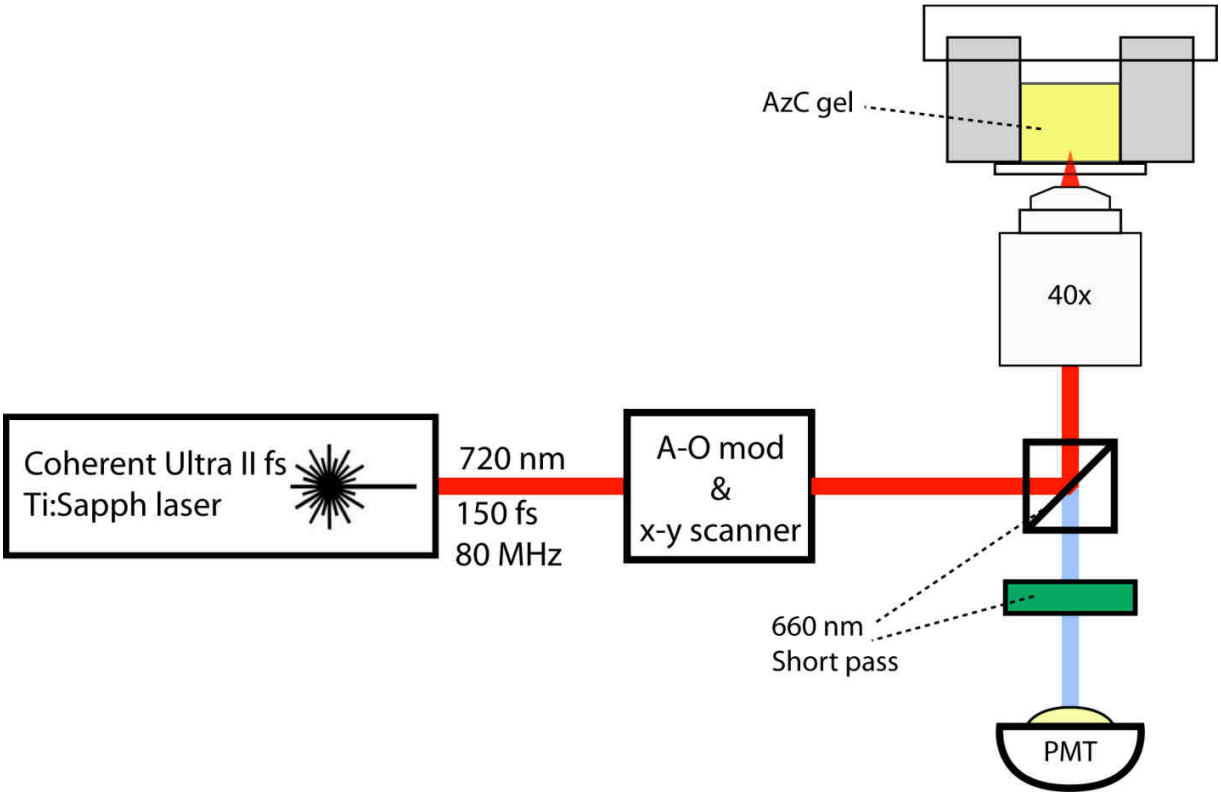

Figure 5.2 Schematic of the experimental setup. 150 fs wide pulses from a Chameleon Ultra II Ti:Sapph ultrafast laser go through an acousto-optical modulator and an x-y scanner (which permits fast scanning of the beam inside the sample), and are focused inside an azidocoumarin-laced gelatin gel contained in an airtight capsule using a Zeiss LSM 510 confocal microscope. Two-photon fluorescence is collected in reflection mode and filtered out from the laser light with a beamsplitter and shortpass optical filter before being detected by a photo multiplier tube.

5.3 Results and Discussion

Fig. 5.3 shows the optical absorptivity spectra of azidocoumarin 151 as it is activated by UV light at 365 nm. (solid lines). The normalized fluorescence spectrum of the fully activated azidodoumarin is also shown (dotted line) along with the absorptivity and fluorescence spectra of coumarin 151 (solid and dashed grey lines). The absorptivity measurements were performed on a 70:30 water:methanol solution containing 50 μM AzC 151 or C151. 20 g/l of Gelatin B was also added to the AzC solution to provide a binding substrate for the activated dye. To avoid phase separation in the gelatin, the measurements were carried out at a temperature of about 35°C. The AzC fluorescence spectrum was collected from the same 1mM AzC gelatin gel as was used in the patterning experiments described below. The C151 fluorescence spectrum was obtained from a 70:30 water:methanol solution containing 1mM of the dye.

The UV light causes the peak at 330 nm in Fig. 5.3 to disappear while a peak at 370 nm emerges. This peak shows good overlap with the absorption peak of C151 in a similar environment. The overlap is not perfect, nor is the absorptivity as high, which is expected given that the AzC converts into multiple products on exposure to light. The fluorescence spectrum from activated AzC is on the other hand almost identical to the C151 fluorescence spectrum, consistent with Fig. 5.1.

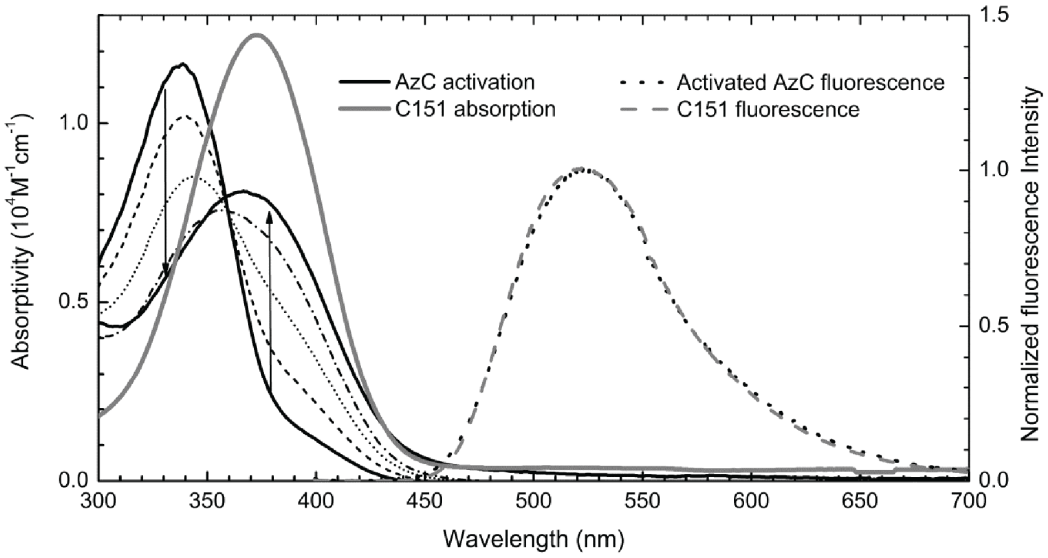

Figure 5.3. Absorptivity spectra of AzC 151 in an methanolic solution and in the presence of gelatin (black lines) as they evolve under UV irradiation. The solid lines represent the initial (0 mJ/cm^2 UV dose) and final (5000 mJ/cm^2 UV dose) spectra. Further UV exposure does not change the spectrum appreciably. The intermediate does are 200 mJ/cm^2, 400 mJ/cm^2 and 800 mJ/cm^2. The absorptivity spectrum of coumarin 151 is also shown (solid grey line). The nearly identical normalized fluorescence spectra of activated AzC151 and C151 are indicated by the dotted black and dashed grey lines, respectively.

When the ultrafast laser is focused at a point in the gel, Azc 151 in the focal spot is photoactivated. Since I am using light with a wavelength of 720 nm, this occurs exclusively through two-photon absorption. The gelatin provides numerous binding sites for the activated coumarin, which with high probability binds to the gel close to the location where it was activated. Because inactivated Azc 151 continually diffuses into the focal spot, there is a buildup of activated coumarin bound to the gel in the spot. From Fig. 5.3 it is clear that the absorption bands of the Azc 151 and its corresponding coumarin dye overlap, so the bound coumarin gives rise to two-photon fluorescence from the same excitation that activated the azide, and the buildup

of bound dye manifests as an onset of fluorescence, as is shown in Fig. 5.4. The fluorescence initially increases linearly with time, but eventually saturates at a constant level as a steady state is achieved where the rates of binding and photobleaching of the coumarin derivatives come into balance.

Since the cross section for two-photon activation of AzC 151 is much smaller than for two-photon fluorescence from the resulting dye, it is possible to image the written fluorescence pattern with the same technique as was used to write it, only using a lower laser power and/or faster scanning. In this mode of operation, the light is sufficient to produce detectable two-photon fluorescence, but not intense enough to cause significant photoactivation of the AzC 151. This is illustrated in Fig. 5.5, where the “VT” logo was written by with a laser power of 32 mW and a pixel dwell time of 250 μs, but the imaging was done with a laser power of 13 mW and a 13 μs pixel dwell time.

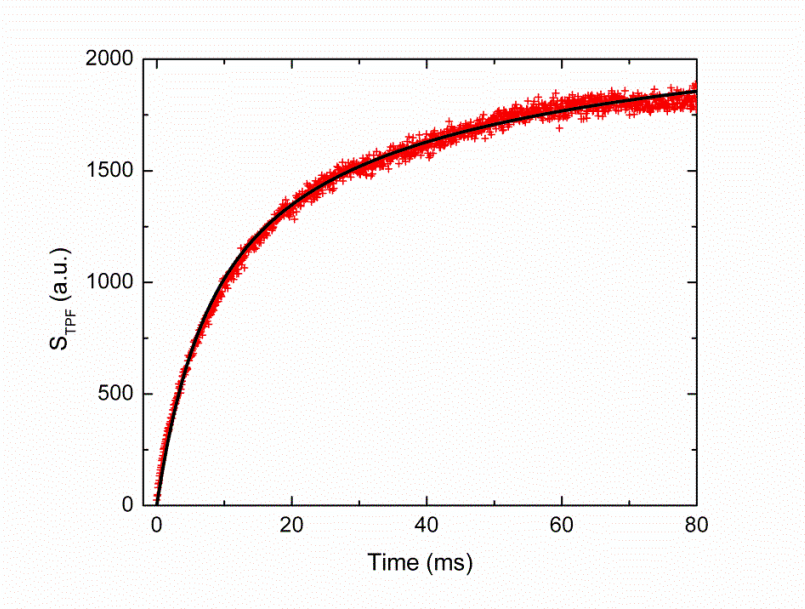

Figure 5.4 Onset of two-photon fluorescence as 720 nm pulsed laser light is focused into the gel, fit to the model described in the text.

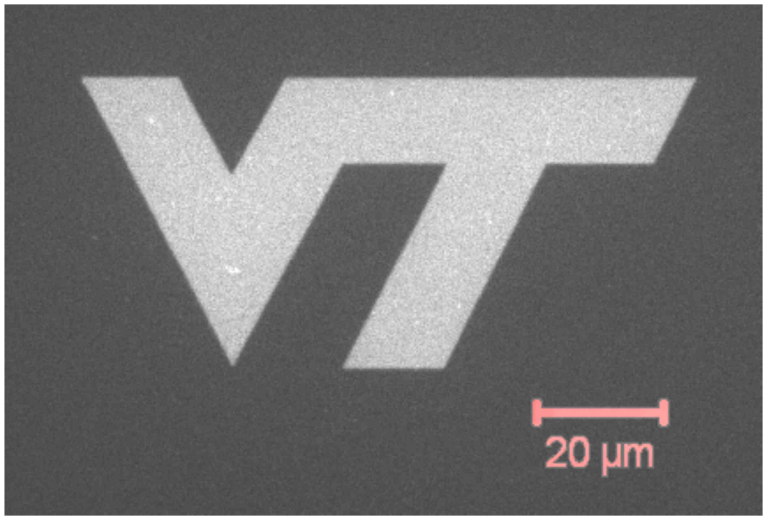

Figure 5.5 Micro-patterned fluorescence created by slow scanning of the target area at high optical power, followed by readout by rapid scanning at a lower power. The latter illumination does not appreciably activate the AzC 151, so pattern creation and visualization can be obtained with the same laser wavelength.

The fluorescence onset in Fig. 5.4 results from the interplay of several effects: Photoactivation of azidocoumarin; diffusion of the photoactivated product through the gel; its binding to the gelatin matrix, resulting in a fluorescent dye; photobleaching of that dye; and diffusion of azidocoumarin from outside the beam to replace the photo converted azide. Since the intensity of the beam is not uniform, the photoactivation takes place at different rates at different points in the beam, and for the same reason, the contribution of each point to the signal is also different.

The full treatment of this problem is beyond the scope of this thesis, but we can make a few simplifying assumptions that will render the problem manageable. First, the diffusion time t_D across the width of the beam is quite short compared to the timescale of photoactivation and bleaching, at least for low laser powers. We can estimate it by $t_d \sim \frac{2W_0^2}{D}$, where $2W_0$ is the beam width, and D is the diffusion constant. The beam width is on the order of 0.5 μm, and the diffusion constant is not likely to be much smaller than 10^{-6} cm^2/s for small molecule diffusion in the gel [116]. t_D is therefore no larger than about a millisecond. Given that the fluorescence onset occurs on timescale from tens of millisecond to several seconds, we can treat the diffusion as instantaneous compared to the timescales of photoactivation and bleaching. The most important consequence of this is that we can treat the background concentration of unreacted azidocoumarin c as essentially constant and equal to its background value throughout the laser beam spot, as photoactivated AzC is rapidly replaced during the illumination.

Moreover, the high reactivity of the photoactivated coumarin combined with the high density of binding sites provided by the gel means that we can ignore any diffusion after photoactivation, and assume that the photoactivation and binding occur at the same locations.

The rate of accumulation of fluorescent dye bound to the gel is therefore proportional to the square of the laser intensity, and the same holds true for the rate of two-photon induced photobleaching. Under those assumptions, the concentration c_f of fluorescent coumarin dye in the gel is given by

$$\frac{dc_f}{dt} = \left(\phi\beta_a c - \beta_b c_f\right) g I_\omega^2\,(\boldsymbol{r}) \qquad (1)$$

where c is the background concentration of unreacted AzC 151, β_a and β_b are the two-photon cross sections for photoactivation and photobleaching, ϕ is the fraction of activated dye that ends up binding to the gel, and $I_\omega(\boldsymbol{r}) = \langle I_\omega(\boldsymbol{r})\rangle$ is the average light intensity distribution inside the focal spot in units of photons×cm^{-2}×s^{-1}. $g = \langle I_\omega^2\rangle/\langle I_\omega\rangle^2$, or the ratio of the time-average of the square of the light intensity to the average light intensity squared. Two-photon processes scale with the former quantity, while the latter is easy to measure directly, so it is convenient to include this scale factor in the calculations. For the typical fs Ti:sapph laser, g is about 10^5. In my case, a sech^2 pulse shape with 150 fs FWHM and a repetition rate of 80 MHz gives g close to 5×10^4.

If the intensity of the light is low enough, diffusion will be efficient enough that we can assume that c is essentially constant throughout the beamspot. In that case, the two-photon fluorescence intensity (S_{TPF}) takes the form

$$S_{TPF} = K\beta_f \int I_\omega^2(\boldsymbol{r}) c_f d\boldsymbol{r} = K\beta_f c\phi g \frac{\beta_a}{\beta_b}\int I_\omega^2(\boldsymbol{r})[1-\exp(-\beta_b g I_\omega^2(\boldsymbol{r})t)]d\boldsymbol{r} \qquad (1)$$

where β_f is the cross section for two-photon fluorescence and the constant K accounts for the detection efficiency of the system. Let us approximate the point spread function of the optical system with an ideal Gaussian beam:

$$I_\omega(\boldsymbol{r}) = \frac{2P}{\pi h\nu W^2(z)} \exp\left(-\frac{2(x^2+y^2)}{W^2(z)}\right) \ , \ \ W^2(z) = W_0^2\left(1+\left(\frac{z}{z_0}\right)\right) \tag{2}$$

where P is the total power of the beam, and the beam waist radius W_0 is related to the depth of focus $2z_0$ and the wavelength in the gel λ by

$$2z_0 = \frac{2\pi W_0^2}{\lambda} \tag{3}$$

This is a reasonable approximation near the center of the beam spot, which is the area that dominates the two-photon fluorescence signal. This is particularly true since we are operating with the confocal aperture wide open, so that the relevant aperture in the system is the back aperture of the microscope objective, which is more than twice the beam diameter.

Physically, Eq. (1) describes an exponential approach to saturation of two-photon fluorescence due to competition between fluorescence activation and bleaching. The rate of this process is proportional to $I_\omega^2(\boldsymbol{r})$, and as a result, the saturation occurs first at the center of the beam, where the intensity is at its maximum. Locations further out see a lower light intensity, and will therefore reach saturation at a later time. The net result of this is that the width of the fluorescent spot made by focusing the pulsed laser into the gel increases over time.

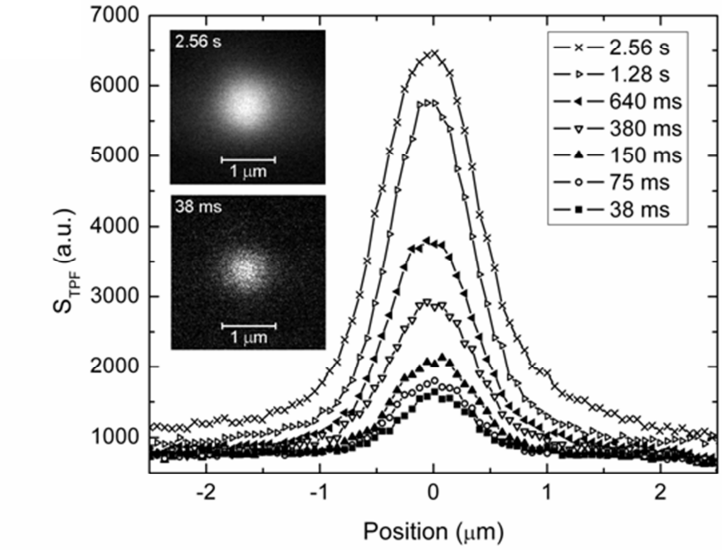

Figure 5.6 Profiles of two-photon fluorescence spots that result from focusing the laser into the gel for varying amounts of time. Because fluorescence saturation occurs first at the center of the beam spot, the width of the spot increases with increasing exposure to the laser light.

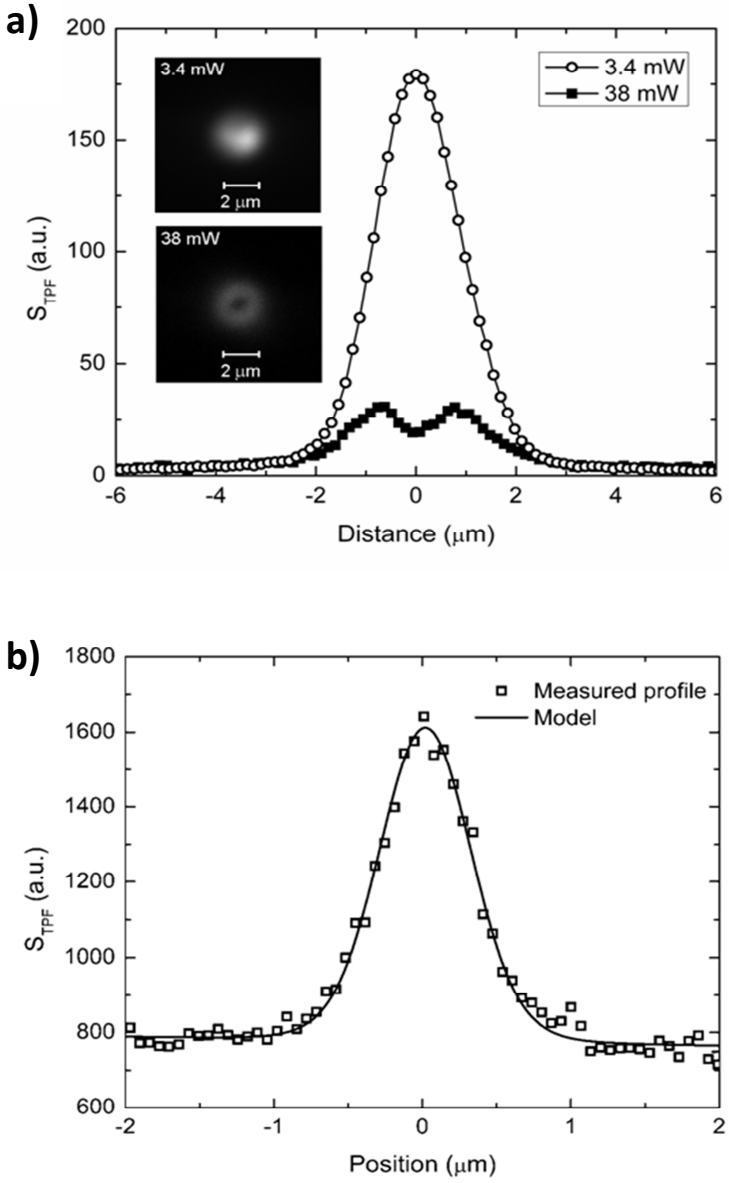

Figure 5.7 (a) Two-photon fluorescence profiles resulting from illuminating the gel at low power for a long time (3.4 mW, 164 s) and at high power for a shorter time (38 mW, 1.27 s). Both illuminations should result in the same amount of Azc 151 activation, but the much less fluorescence is seen in the high power case due to damage inflicted on the gel (b) Two-photon fluorescence profile obtained at low power and short illumination time in order to minimize saturation. The solid line is a fit to the autocorrelation function of a Gaussian beam profile, yielding a beam radius of 0.56 μm.

This can be seen in the data plotted in Fig.5.6, which was obtained by illuminating a single location in the gel for a set amount of time, and then scanning across the x-y plane while

measuring the two-photon fluorescence. The resulting profile is therefore $c_f * I_\omega^2$, or the convolution of the concentration of fluorescent dye bound to the gel with the square of the point spread function. In Fig. 5.6, the gel was illuminated with a 40x oil immersion objective at an optical power of 13 mW. As the illumination time is increased, the effective width of the fluorescent spot is gradually increasing, with a marked saturation of the fluorescence intensity seen, particularly at the center of the spot.

Taking$I_\omega(\boldsymbol{r})$ to be Gaussian, Eq. (1) cannot be solved explicitly, but I can write it as a power series:

$$S_{TPF} = K\phi c \frac{\beta_a}{\beta_b} \frac{gP^2}{(h\nu)^2\lambda} \sum_{n=1}^{\infty} \frac{(-1)^{n+1}}{(n+1)\pi^{2n-1}} \frac{(4n-1)!!}{n!(2n)!} \left(\frac{gP^2\beta_b}{(\nu h)^2 W_0^4} t\right)^n \ . \tag{4}$$

The integral takes on a simpler form at short and long times. At short times, photobleaching is not a factor, and the fluorescence increases linearly in time, and Eq. (1) can be approximated as

$$S_{TPF}^0 \approx K' g^2 \lambda \beta_f \beta_a t \int I_\omega^4(\boldsymbol{r}) d\boldsymbol{r} = \frac{3K' g^2 \beta_f \beta_a}{4\pi (h\nu W_0)^4} P^4 t \ . \tag{5}$$

At long times, the fluorescence saturates, tending to a constant value

$$S_{TPF}^\infty = K' g \lambda \beta_f \beta_a t \int I_\omega^2(\boldsymbol{r}) d\boldsymbol{r} = K' g \beta_f \frac{\beta_a}{\beta_b} \frac{\pi}{(h\nu)^2} P^2 \tag{6}$$

In other words, the initial slope of the activation curve will be proportional to P^4, while the fluorescence signal at saturation is proportional to P^2. The onset of fluorescence is due to a combination of two two-photon processes, activation and fluorescence, which explains the P^4 scaling of the initial slope. Saturation of the fluorescence is reached at a value that depends on the ratio of the activation and photobleaching cross sections, and since both of those processes

have the same P^2 dependence on optical power, the quantity of optically active fluorophores at saturation is independent of optical power, at least at first approximation. For that reason, S_{TPF}^{∞} is governed only by a two-photon fluorescence process, and should scale as P^2.

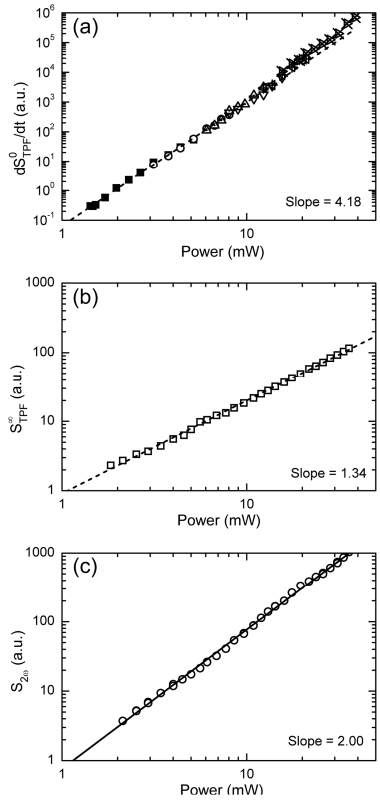

Figure 5.8 (a) Log plot of the initial slope of the two-photon fluorescence onset as a function of incident optical power. The exponent is approximately four because the onset results from the combination of two-photon activation and two-photon fluorescence, each of which contributes a factor of P^2 to the power dependence. The different marker styles correspond to different settings for the detector gain and integration time. (b) Log plot of the steady state two-photon fluorescence signal at long times vs. incident optical power. (c) Log plot of the two-photon fluorescence signal from a previously photoactivated volume of the gel. In contrast to plots (a) and (b), the beam is scanned rapidly to negate the effect of photobleaching.

As can be seen in Fig. 5.8(a), the initial slope of the observed two-photon fluorescence obeys these scaling laws quite well, with an exponent of 4.18. The deviation from the exact value of 4 can be attributed to the nonlinearity of my optical power meter and the difficulty of accurately

measuring the initial slope of a curve over six orders of magnitude of dynamic range. As for S_{TPF}^{∞}, it does obey a power law but the observed exponent (Fig. 5.8(b)) is only 1.34, well below the predicted value of 2.

To help determine the source of this deviation from the model, we optically activated AzC in a volume of the gel, creating a concentration c_f^0 of fluorescent dye within the volume. Two-photon fluorescence ($S_{2\omega}$) was then measured by rapidly scanning through this region while varying the laser power. Neither photoactivation nor photobleaching affect $S_{2\omega}$, which is given by

$$S_{2\omega} = \frac{K\phi c_f^0}{\lambda} g\beta_f \frac{\pi}{(h\nu)^2} P^2 \tag{7}$$

As shown in Fig. 5.8(c), the P^2 scaling is actually observed in this case, which means that the observed fluorescence is indeed due to two-photon fluorescence, and the deviation from Eq. (7) is due to some other factor.

Clearly, some process other than two-photon photobleaching is at work suppressing the fluorescence from the activated azidocoumarin, at least at longer time scales. This can also be seen from the fluorescence spot scans shown in Fig. 5.7(a). Here, the gel was illuminated at 3.4 mW for 164 s, and 38 mW for 1.27 s. $t_{ill}P^2$, the illumination time multiplied by the square of the optical power, is approximately the same in both cases. If Eq (2) were accurate at all-time scales, we would expect the same amount of photoactivation and photobleaching to have taken place in both cases, and the two resulting traces in Fig. 5.7(a) would be very similar. Instead, only the fluorescence pattern at low illumination power shows the expected peak. At high power, a ring

of fluorescence is seen instead, and the peak fluorescence is much lower than in the low power case. If the fluorescence quenching were due exclusively to a two-photon process we would expect to see a flattening of the peak at long illumination times as the fluorescence everywhere approaches the same value. The ring-like shape must then be attributed to a process that scales faster with optical power thanP^2. This could include multi-photon processes as well as optically or thermo-optically induced changes in the gelatin matrix.

Once a ring-like structure such as shown in the insert in Fig. 5.7(a) has been created, it is permanent. Illuminating the same location at low optical power for a long time still results in a ring-like fluorescence pattern rather than the single peak. I therefore conclude that the additional two-photon fluorescence quenching seen at high powers and long times is due to damage or phase change in the gel induced by the high optical power density. Gelatin solutions have a sol-gel transition temperature near 28 °C [115], and the gelatin-water-alcohol mixture I am using is metastable at room temperature. It is then quite reasonable that intense light can trigger local phase separation or other changes in the gel if applied for a sufficiently amount of time. In spite of this, the initial slope of the two-photon fluorescence onset has the predicted dependence on optical power over a wide range of powers, which indicates that at short exposure times, damage to the gel is not yet significant, and the model presented above is accurate.

To model the degradation, we will make three simplifying assumptions: (1) The rate of degradation depends only on the local light intensity$I_\omega(\boldsymbol{r})$. (2) There is a threshold for degradation, so that if the light intensity does not exceed some value I_m, no degradation takes place. (3) Wherever $I_\omega(\boldsymbol{r}) > I_m$, the fluorescence will eventually go to 0. Denoting $P_m = \frac{1}{2}\pi(h\nu)^2 W_0^2$, we have, when $P > P_m$,

$$S_{TPF}^{\infty} = K'\lambda g\beta_f \frac{\beta_a}{\beta_b}\int_{I_\omega<I_m} I_\omega^2(\boldsymbol{r})d\boldsymbol{r} =$$

$$= K'\lambda g\beta_f \frac{\beta_a}{\beta_b}\frac{2}{(h\nu)^2}\left[\frac{1}{3}(P+2P_m)\sqrt{P_m(P-P_m)} + P^2 arc\tan\sqrt{\frac{P_m}{P-P_m}}\right] \quad (8)$$

$$\rightarrow K'g\beta_f \frac{\beta_a}{\beta_b}\frac{8}{3(h\nu)^2}P_m^{\frac{1}{2}}P^{\frac{3}{2}}$$

For $P \leq P_m$, Eq. (9) is still valid. The 3/2 exponent in the optical power dependence in Eq. (8) is not exactly what is observed, but it is close enough to our observations that the difference could be due to measurement errors, particularly since Eq. (8) can be fit quite well with a function proportional to $P^{1.43}$ when $1 < \frac{P}{P_m}$. It is also likely that the assumptions we made to arrive at Eq. (8) are not entirely valid for our situation, although they are a good starting point as they lead to an easily solvable model that is largely consistent with our observations.

The validity of the model could further be verified by fitting the function given by Eq. (4) to the fluorescence onset curve. As can be seen from Fig. 5.4, the fit is quite good, at least for short times. For longer times, the model deviates significantly from the data, as expected (not shown). Not only does the gel damage start to set in over time, but since the fluorescence from the center of the beam spot saturates first, the evolution of the fluorescence at later times depends on the details of the point spread function farther away from the focus, where the Gaussian approximation no longer is particularly good.

With sufficiently good knowledge of the point spread function, I can use the fit in Fig. 5.4 to measure the two-photon bleaching rate of the activated AzC 151. The fit is done with two free parameters, a constant of proportionality and a time scale. The scale factor in time (γ) is, from Eq. (4)

$$\gamma = \frac{gP^2\beta_b}{(h\nu)^2 W_0^4}, \tag{10}$$

where all parameters except β_b can be measured directly. The source of the greatest uncertainty is the fourth-power dependence on the beam spot radius. More generally, the true point spread function of the optical system must be well known if I am to be able to accurately determine β_b. For that reason, I am only provididing a rough estimate here, based on my Gaussian approximation of the beam profile.

W_0 was estimated by using the fluorescence spot scans in Fig. 5.6. At sufficiently low power and short illumination time, before fluorescence saturation sets in, the spot profile will be proportional to the autocorrelation function of the square of the laser intensity

$$(I_\omega^2 * I_\omega^2)[x, y = z = 0] \propto \int_{-\infty}^{\infty} \frac{exp\left(-\frac{2x^2}{W_0(1+z^2)}\right)}{(1+z^2)^3} dz, \tag{11}$$

which can be solved numerically and fit to the data to extract W_0, which has been done in Fig. 5.8(c). The fit gives us that $W_0 =$ 0.56 μm. With an incident power of 8.3 mW, I found a scale factor of about 294 s^{-1}. Taking g to be 5×10^4, Eq. (10) yields an estimate of β_p 0.006 G.M. (10^{-50} cm^4s). Given the likelihood that photobleaching has broadened the fluorescent spot even at the low power conditions used in Fig. 5.7(b), it is likely that my estimate for W_0 is somewhat large, and the obtained value for β_p should be treated as an upper limit. It is worth mentioning that as we use high quality optics, we could expect diffraction limited behavior, which for our N.A. 0.6 laser beam would give W_0 0.38 μm and β_p0.0015 G.M.

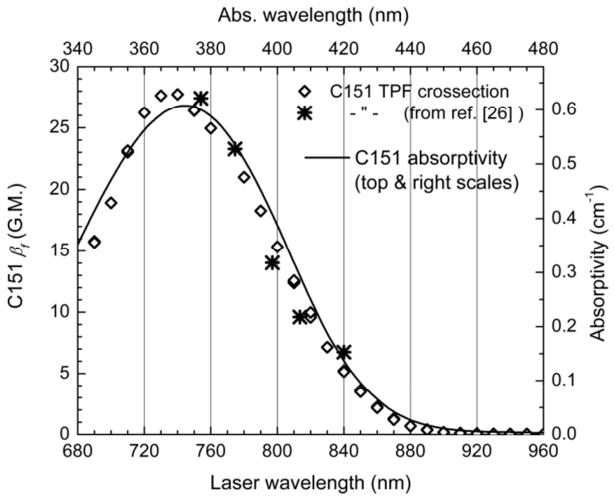

Figure 5.9 (left and bottom axes): Open diamonds (◇) plot the two-photon fluorescence cross section ( ) of C151 dissolved at 1mM concentration in a gelatin gel. The data was obtained by measuring the two-photon fluorescence intensity as a function of laser wavelength, and scaling to agree with data from ref. [117], indicated by stars (✱). (top and right axes): The solid line (—) is the absorption spectrum of coumarin 151. The two horizontal scales differ by a factor of two, and the good agreement between the datasets indicate that one- and two-photon absorption occurs into the same electronic state.

In Fig. 5.9, I have plotted the two-photon fluorescence cross section of C151 vs. wavelength (open diamonds). This was obtained by measuring the two-photon fluorescence at different excitation wavelengths while maintaining a constant laser power. The data was then scaled to match literature values for the two-photon absorption cross section ( ) in C151 [117], and taking the quantum yield of fluorescence ( ) to be 0.582 [117], from which I can extract

. The linear absorption spectrum for C151 is also plotted in Fig. 5.9. By choosing the absorption wavelength range to be precisely half of the laser wavelengths, I get good agreement between linear and nonlinear spectra, indicating that both one- and two-photon absorption occur into a single electronic state. From the figure, we estimate that 26 G.M. for C151 at 720 nm.

I do not know the abundance of the reaction products in the gel after photoactivation of AzC151, so it is harder to obtain β_f for **5**. Since the absorption of the photoactivated dye peaks at a shorter wavelength than for C151, it is however likely to have a smaller β_f value. From this I can estimate the quantum yield of photobleaching $\Phi_b = \Phi_f \frac{\beta_b}{\beta_f}$ to be in the 10^{-3} – 10^{-4} range, consistent with values obtained for other coumarin dyes under single photon excitation. [118]

5.4 Conclusion

I have studied the onset of two-photon fluorescence in azidocoumarin 151 contained in a gelatin matrix and illuminated by focused femtosecond laser light. Since the photactivated intermediary is highly reactive, it binds to the gelatin matrix close to the location of its creation. This makes it possible to create arbitrary three-dimensional patterns of fluorescence, similarly to the way two-photon exposure of a photoresist can be used to create arbitrary three-dimensional geometries.

A model based on a Gaussian approximation of the beam profile described the onset of fluorescence quite well at short time scales, but failed at longer times, likely due to a combination of damage to the gel and the inadequacy of the Gaussian approximation when outlying areas of the beam spot dominate the behavior of the two-photon fluorescence at long times. The success of the model at short times maked it possible to extract an estimate for the two-photon cross section for photobleaching of the coumarin dye. As the beam waist was known to insufficient accuracy, the estimate was quite rough, but this could be remedied with better knowledge of the microscope point spread function.

REFERENCES

1. B. G. Prevo and O. D. Velev, Langmuir **20** (6), 2099-2107 (2004).
2. G. Schmid and L. F. Chi, Advanced Materials **10** (7), 515-526 (1998).
3. A. P. Alivisatos, Science **271** (5251), 933-937 (1996).
4. B. G. Prevo, E. W. Hon and O. D. Velev, Journal of Materials Chemistry **17** (8), 791-799 (2007).
5. Y. A. Vlasov, X. Z. Bo, J. C. Sturm and D. J. Norris, Nature **414** (6861), 289-293 (2001).
6. S. H. Park and Y. N. Xia, Langmuir **15** (1), 266-273 (1999).
7. R. J. Spry and D. J. Kosan, Appl. Spectroscopy **40** (6), 782-784 (1986).
8. I. Willner and B. Willner, Pure Appl. Chem. **74** (9), 1773-1783 (2002).
9. J. H. Holtz and S. A. Asher, Nature **389** (6653), 829-832 (1997).
10. O. D. Velev, T. A. Jede, R. F. Lobo and A. M. Lenhoff, Nature **389** (6650), 447-448 (1997).

11. B. T. Holland, C. F. Blanford and A. Stein, Science **281** (5376), 538-540 (1998).

12. D. M. Kuncicky, B. G. Prevo and O. D. Velev, Journal of Materials Chemistry **16** (13), 1207-1211 (2006).

13. A. B. Pawar and I. Kretzschmar, Langmuir **24** (2), 355-358 (2008).

14. C. L. Haynes and R. P. Van Duyne, J. Phys. Chem. B **105** (24), 5599-5611 (2001).

15. Y. N. Xia, B. Gates, Y. D. Yin and Y. Lu, Advanced Materials **12** (10), 693-713 (2000).

16. D. G. Grier, Mrs Bulletin **23** (10), 21-21 (1998).

17. S. Hayashi, Y. Kumamoto, T. Suzuki and T. Hirai, Journal of Colloid and Interface Science **144** (2), 538-547 (1991).

18. B. Gates and Y. N. Xia, Advanced Materials **13** (21), 1605-+ (2001).

19. P. Jiang, G. N. Ostojic, R. Narat, D. M. Mittleman and V. L. Colvin, Advanced Materials **13** (6), 389-393 (2001).

20. K. E. Davis, W. B. Russel and W. J. Glantschnig, Science **245** (4917), 507-510 (1989).

21. J. L. Harland, S. I. Henderson, S. M. Underwood and W. Vanmegen, Physical Review Letters **75** (19), 3572-3575 (1995).

22. S. M. Clarke, A. R. Rennie and R. H. Ottewill, Langmuir **13** (7), 1964-1969 (1997).

23. H. W. Deckman and J. H. Dunsmuir, Applied Physics Letters **41** (4), 377-379 (1982).

24. J. C. Hulteen and R. P. Vanduyne, Journal of Vacuum Science & Technology a-Vacuum Surfaces and Films **13** (3), 1553-1558 (1995).

25. F. Burmeister, C. Schafle, B. Keilhofer, C. Bechinger, J. Boneberg and P. Leiderer, Advanced Materials **10** (6), 495-+ (1998).

26. R. Micheletto, H. Fukuda and M. Ohtsu, Langmuir **11** (9), 3333-3336 (1995).

27. P. A. Kralchevsky, V. N. Paunov, I. B. Ivanov and K. Nagayama, Journal of Colloid and Interface Science **151** (1), 79-94 (1992).

28. N. D. Denkov, O. D. Velev, P. A. Kralchevsky, I. B. Ivanov, H. Yoshimura and K. Nagayama, Langmuir **8** (12), 3183-3190 (1992).

29. A. S. Dimitrov and K. Nagayama, Langmuir **12** (5), 1303-1311 (1996).

30. A. S. Dimitrov and K. Nagayama, Chemical Physics Letters **243** (5-6), 462-468 (1995).

31. B. G. Prevo, D. M. Kuncicky and O. D. Velev, Colloids Surf. A **311** (1-3), 2-10 (2007).

32. N. D. Denkov, O. D. Velev, P. A. Kralchevsky, I. B. Ivanov, H. Yoshimura and K. Nagayama, Nature **361** (6407), 26-26 (1993).

33. P. A. Kralchevsky, V. N. Paunov, N. D. Denkov, I. B. Ivanov and K. Nagayama, Journal of Colloid and Interface Science **155** (2), 420-437 (1993).

34. J. D. Swalen, D. L. Allara, J. D. Andrade, E. A. Chandross, S. Garoff, J. Israelachvili, T. J. McCarthy, R. Murray, R. F. Pease, J. F. Rabolt, K. J. Wynne and H. Yu, Langmuir **3** (6), 932-950 (1987).

35. A. Ulman, Chemical Reviews **96** (4), 1533-1554 (1996).

36. M. Sano, Y. Lvov and T. Kunitake, Annual Review of Materials Science **26**, 153-187 (1996).

37. A. Laschewsky, European Chemistry Chronicle ECC (2), 13-24 (1997).

38. Y. Lvov, G. Decher and H. Mohwald, Langmuir **9** (2), 481-486 (1993).

39. G. Decher and J. D. Hong, Berichte Der Bunsen-Gesellschaft-Physical Chemistry Chemical Physics **95** (11), 1430-1434 (1991).

40. G. Decher, J. D. Hong and J. Schmitt, Thin Solid Films **210** (1-2), 831-835 (1992).

41. J. Gun and J. Sagiv, Journal of Colloid and Interface Science **112** (2), 457-472 (1986).

42. G. Roberta, Plenum Press, 420 (1990).

43. J. Hiller and M. F. Rubner, Macromolecules **36** (11), 4078-4083 (2003).

44. K. Itano, J. Y. Choi and M. F. Rubner, Macromolecules **38** (8), 3450-3460 (2005).

45. T. K. Sau and A. L. Rogach, Advanced Materials **22** (16), 1781-1804 (2010).

46. S. Pal, Z. T. Deng, B. Q. Ding, H. Yan and Y. Liu, Angewandte Chemie-International Edition **49** (15), 2700-2704 (2010).

47. D. Fava, Z. Nie, M. A. Winnik and E. Kumacheva, Advanced Materials **20** (22), 4318-4322 (2008).

48. J. P. Novak, L. C. Brousseau, F. W. Vance, R. C. Johnson, B. I. Lemon, J. T. Hupp and D. L. Feldheim, Journal of the American Chemical Society **122** (48), 12029-12030 (2000).

49. L. Hong, A. Cacciuto, E. Luijten and S. Granick, Nano Letters **6** (11), 2510-2514 (2006).

50. K. K. Caswell, J. N. Wilson, U. H. F. Bunz and C. J. Murphy, Journal of the American Chemical Society **125** (46), 13914-13915 (2003).

51. F. L. Yap and Y. Zhang, Biosensors & Bioelectronics **22** (6), 775-788 (2007).

52. D. L. Jeanmaire and R. P. Vanduyne, Journal of Electroanalytical Chemistry **84** (1), 1-20 (1977).

53. M. G. Albrecht and J. A. Creighton, Journal of the American Chemical Society **99** (15), 5215-5217 (1977).

54. E. Hao and G. C. Schatz, Journal of Chemical Physics **120** (1), 357-366 (2004).

55. A. Campion and P. Kambhampati, Chemical Society Reviews **27** (4), 241-250 (1998).

56. H. Wang and N. J. Halas, Nano Letters **6** (12), 2945-2948 (2006).

57. A. M. Michaels, M. Nirmal and L. E. Brus, Journal of the American Chemical Society **121** (43), 9932-9939 (1999).

58. A. Otto, I. Mrozek, H. Grabhorn and W. Akemann, Journal of Physics-Condensed Matter **4** (5), 1143-1212 (1992).

59. E. Burstein, Y. J. Chen, C. Y. Chen, S. Lundquist and E. Tosatti, Solid State Communications **29** (8), 567-570 (1979).

60. J. I. Gersten, R. L. Birke and J. R. Lombardi, Physical Review Letters **43** (2), 147-150 (1979).

61. J. R. Lombardi, R. L. Birke, T. H. Lu and J. Xu, Journal of Chemical Physics **84** (8), 4174-4180 (1986).

62. E. Betzig, G. H. Patterson, R. Sougrat, O. W. Lindwasser, S. Olenych, J. S. Bonifacino, M. W. Davidson, J. Lippincott-Schwartz and H. F. Hess, Science **313** (5793), 1642-1645 (2006).

63. S. T. Hess, T. P. K. Girirajan and M. D. Mason, Biophysical Journal **91** (11), 4258-4272 (2006).

64. M. J. Rust, M. Bates and X. W. Zhuang, Nature Methods **3** (10), 793-795 (2006).

65. C. N. LaFratta, J. T. Fourkas, T. Baldacchini and R. A. Farrer, Angewandte Chemie-International Edition **46** (33), 6238-6258 (2007).

66. W. H. Zhou, S. M. Kuebler, K. L. Braun, T. Y. Yu, J. K. Cammack, C. K. Ober, J. W. Perry and S. R. Marder, Science **296** (5570), 1106-1109 (2002).

67. W. Kern and D. A. Poutinen, RCA Review **31**, 187-206 (1970).

68. A. Zdziennicka, J. Colloid Interface Sci. **336** (2), 423-430 (2009).

69. B. V. Derjaguin and N. V. Churaev, Langmuir **3** (5), 607-612 (1987).

70. J. S. Mohammed, M. A. DeCoster and M. J. McShane, Biomacromolecules **5** (5), 1745-1755 (2004).

71. J. Y. Jung, K. W. Kim, K. Na, M. Kaholek, S. Zauscher and J. Hyun, Macromol. Rapid Commun. **27** (10), 776-780 (2006).

72. H. P. Zheng, M. C. Berg, M. F. Rubner and P. T. Hammond, Langmuir **20** (17), 7215-7222 (2004).

73. H. Ai, Y. M. Lvov, D. K. Mills, M. Jennings, J. S. Alexander and S. A. Jones, Cell Biochemistry and Biophysics **38** (2), 103-114 (2003).

74. K. B. Lee, J. H. Lim and C. A. Mirkin, J. Am. Chem. Soc. **125** (19), 5588-5589 (2003).

75. D. R. Reyes, E. M. Perruccio, S. P. Becerra, L. E. Locascio and M. Gaitan, Langmuir **20** (20), 8805-8811 (2004).

76. A. Winkleman, B. D. Gates, L. S. McCarty and G. M. Whitesides, Adv. Mater. **17** (12), 1507-1511 (2005).

77. M. Suzuki, T. Yasukawa, Y. Mase, D. Oyamatsu, H. Shiku and T. Matsue, Langmuir **20** (25), 11005-11011 (2004).

78. S. Ogata, T. Yasukawa and T. Matsue, Bioelectrochemistry **54** (1), 33-37 (2001).

79. T. Kimura, Y. Sato, F. Kimura, M. Iwasaka and S. Ueno, Langmuir **21** (3), 830-832 (2005).

80. K. Mitsui, Y. Handa and K. Kajikawa, Appl. Phys. Lett. **85** (18), 4231-4233 (2004).

81. N. Nath and A. Chilkoti, Analytical Chemistry **74** (3), 504-509 (2002).

82. S. F. Cheng and L. K. Chau, Anal. Chem. **75** (1), 16-21 (2003).

83. J. Zhao, X. Zhang, C. R. Yonzon, A. J. Haes and R. P. Van Duyne, Nanomed. **1** (2), 219-228 (2006).

84. C. L. Haynes and R. P. Van Duyne, J. Phys. Chem. B **107** (30), 7426-7433 (2003).

85. D. L. Jeanmaire and R. P. Van Duyne, J. Electroanal. Chem. **84** (1), 1-20 (1977).

86. S. Nie and S. R. Emory, Science **275**, 1102-1106 (1997).

87. K. Kneipp, Y. Wang, H. Kneipp, L. T. Perelman, I. Itzkan, R. Dasari and M. S. Feld, Phys. Rev. Lett. **78** (9), 1667-1670 (1997).

88. A. J. Haes, W. P. Hall, L. Chang, W. L. Klein and R. P. Van Duyne, Nano Lett. **4** (6), 1029-1034 (2004).

89. S. Ekgasit, C. Thammacharoen, F. Yu and W. Knoll, Appl. Spectrosc. **59** (5), 661-667 (2005).

90. Z. Adamczyk, K. Jaszczolt, B. Siwek and P. Weronski, Langmuir **21** (19), 8952-8959 (2005).

91. M. F. Rubner, in *Multilayer Thin Films*, edited by G. Decher and J. B. Schlenoff (Wiley, 2003), pp. 133-154.

92. K. Chen, S. V. Stoianov, J. Bangerter and H. D. Robinson, J. Colloid Interface Sci. **344** (2), 315-320 (2010).

93. G. Frens, Nature Phys. Sci. **241**, 20-22 (1973).

94. M. Onda, Y. Lvov, K. Ariga and T. Kunitake, J. Ferment. Bioeng. **82** (5), 502-506 (1996).

95. T. G. Shutava, D. S. Kommireddy and Y. M. Lvov, J. Am. Chem. Soc. **128** (30), 9926-9934 (2006).

96. R. Renner, Environ. Sci. Technol. **40** (1), 12-13 (2006).

97. F. Frederix, K. Bonroy, W. Laureyn, G. Reekmans, A. Campitelli, W. Dehaen and G. Maes, Langmuir **19** (10), 4351-4357 (2003).

98. L. K. Chau, Y. F. Lin, S. F. Cheng and T. J. Lin, Sensors and Actuators B-Chemical **113** (1), 100-105 (2006).

99. W. Zhang, A. O. Govorov and G. W. Bryant, Physical Review Letters **97** (14) (2006).

100. W. P. McConnell, J. P. Novak, L. C. Brousseau, R. R. Fuierer, R. C. Tenent and D. L. Feldheim, Journal of Physical Chemistry B **104** (38), 8925-8930 (2000).

101. Z. L. Zhang and S. C. Glotzer, Nano Letters **4** (8), 1407-1413 (2004).

102. A. Walther and A. H. E. Muller, Soft Matter **4** (4), 663-668 (2008).

103. S. B. Chaney, S. Shanmukh, R. A. Dluhy and Y. P. Zhao, Applied Physics Letters **87** (3) (2005).

104. G. Socrates, *Infrared and Raman Characteristic Group Frequences, Tables and Charts*, third edition ed. (Wiley, 2000).

105. J. Gersten and A. Nitzan, Journal of Chemical Physics **73** (7), 3023-3037 (1980).

106. M. C. Daniel and D. Astruc, Chemical Reviews **104** (1), 293-346 (2004).

107. X. Allonas, J. P. Fouassier, M. Kaji, M. Miyasaka and T. Hidaka, Polymer **42** (18), 7627-7634 (2001).

108. B. M. Monroe and G. C. Weed, Chem. Rev. **93** (1), 435-448 (1993).

109. S. K. Wu, J. K. Zhang, J. P. Fouassier and D. Burr, Photographic Science and Photochemistry **2**, 47-54 (1989).

110. T. Wang, Y. X. Zhao, M. Q. Shi and F. P. Wu, Dyes and Pigments **75** (1), 104-110 (2007).

111. S. J. Lord, H. L. D. Lee, R. Samuel, R. Weber, N. Liu, N. R. Conley, M. A. Thompson, R. J. Twieg and W. E. Moerner, Journal of Physical Chemistry B **114** (45), 14157-14167 (2010).

112. K. A. Schnapp, R. Poe, E. Leyva, N. Soundararajan and M. S. Platz, Bioconjugate Chem. **4** (2), 172-177 (1993).

113. K. S. Feng, F. Mahdavianary, R. E. Partch and Y. Z. Li, Photochem. Photobiol. **62** (5), 813-817 (1995).

114. K. Barral, A. D. Moorhouse and J. E. Moses, Org. Lett. **9** (9), 1809-1811 (2007).

115. T. Tanaka, G. Swislow and I. Ohmine, Phys. Rev. Lett. **42** (23), 1556-1559 (1979).

116. L. Friedman, J. Am. Chem. Soc. **52** (4), 1305-1310 (1930).

117. A. Fischer, C. Cremer and E. H. K. Stelzer, Appl. Opt. **34** (12), 1989-2003 (1995).

118. C. Eggeling, J. Widengren, R. Rigler and C. A. M. Seidel, Anal. Chem. **70** (13), 2651-2659 (1998).